TECHNISCHE UNIVERSITÄT MÜNCHEN

TUM School of Natural Sciences

NON-IDEALITY IN ACID CATALYZED ALCOHOL DEHYDRATION REACTIONS IN CONDENSED-PHASE

Niklas Pfriem

Vollständiger Abdruck der von der TUM School of Natural Sciences der Technischen Universität München zur Erlangung des akademischen Grades eines

Doktors der Naturwissenschaften (Dr. rer. nat)

genehmigten Dissertation.

Vorsitz:	Hon.-Prof. Dr. Richard W. Fischer
Prüfer*innen der Dissertation:	1. Prof. Dr. Johannes A. Lercher
	2. Prof. Dr.-Ing. Kai-Olaf M. Hinrichsen
	3. Prof. Dr. Gary L. Haller, Ph.D.

Die Dissertation wurde am 12.09.2022 bei der Technischen Universität München eingereicht und durch die TUM School of Natural Sciences am 28.02.2023 angenommen.

Für meine Familie

Nothing is too wonderful to be true, if it be consistent with the laws of nature, and in such things as these, experiment is the best test of such consistency.

Michael Faraday

Acknowledgments

First of all I want to thank Prof. Dr. Johannes A. Lercher for supervising me during my PhD Thesis. I really enjoyed our discussions, the productive work atmosphere and I'm grateful for the four years I spent in your research group.

I also deeply appreciated the guidance of Prof. Dr. Gary Haller. Gary, you were always helping with new ideas, you reflected scientific problems from a different angle and helped a lot during the preparation of the manuscripts. I really enjoyed the time when you were around in Munich.

Special gratitude goes to Dr. Hui Shi, who accompanied me during the different stages of my PhD. You helped me a lot in finding, formulating and addressing topics for my thesis and the published manuscripts. I wish you all the best for your new career in China!

Best wishes and gratitude also go to Dr. Yue Liu. Thanks for the detailed discussion about thermodynamics and kinetics, your help with the "Science manuscript" and many thanks for your insistence on Science Journal. I learned a lot from you during the last four years and I wish you and Wei all the best for your new chapter in China!

I want to thank Apl. Prof. Dr. Andreas Jentys for the scientific discussions about spectroscopy, the teaching experience and the casual conversations on the hallway. Many thanks go also to Stefanie Seibold, Ulrike Sanwald, Bettina Federmann, and Kateryna Kryvko for their support, their excellent work that made life during PhD a lot easier and the time we spend together during BBQ's or Christmas-Party's.

Xaver Hecht, Andreas Marx, and Martin Neukamm, I really appreciated your help during my time in the lab. Xaver helped many times with this fundamental knowledge and experience, Martin with organizing the orders and the gas supply and Andreas with IT problems!

In addition much of the success of this thesis is derived from the work of many excellent students. I want to thank Florian Zahn, helping a lot during his Master's Thesis and who is now my successor in the lab. Thanks to Yihong „Jack" Lou, spending more than a year in my lab. Svenja „Saskia" Knösch, working hard but also making lab hours way more fun. Christian Fajman, Simon Krebs, Christoph Gross, Felix Simon, Franziska Held, Lucas Hirschberger und Simon Roßkopf, thanks for your support.

During my time in Johannes lab, many colleagues became friends, some even more than friends. So special gratitude goes to Verena Höpfl! We have and had a great time together since we first met on a Nockherberg trip of TC2, joined both Johannes Chair and worked and lived together the last years, went together on business trips and conferences. We had many great moments together during our PhD!

For sure I have to point out some special colleagues and friends that spend many nights with me in the lab, discussing all kinds of problems and supporting me during these four years of PhD. Thanks to Roland Weindl, Insu Lee, Alexander Wellmann und Ferdinand Voglsang! I really enjoyed the time in the bunker and at the NMR, our TC2 Party's and our coffee breaks. During CoVid-19 pandemic I was really grateful that you guys were always up for a Teams-conference talking about the latest gossip and news.

Furthermore I want to thank Felix Kirchberger, Martina Aigner, Laura Löbbert, Lingli Ni, Lei Tao, Jakub Pazdera, Ruixue Zhao, Martin Baumgärtl, Rachit Khare, Madita Einemann and Philipp Fischer for the great time during my PhD. During my studies I also appreciated the time and supervision of Andreas Ehrmaier, Silvia Albersberger, Sebastian Eckstein and Junnan Shangguan from the University of Toronto.

I also deeply appreciated the support of the biomass-/HDO-Crew. Lara Milakovic, Christoph Denk, Qiang Liu, Iris K.M. Yu, Fuli Deng, Takayoshi Oshima, Mingwu Tan, Guanhua Cheng, Xi Chen, Karen Resende, and Lennart Wahl. Thanks for the great time in the lab. Special thanks also go to Mirjam Wenig, Andreas Brenig and Amelie Mühlbach making the biomass lab a great place to work.

Ein besonderer Dank gilt meinen Eltern Heike und Horst, meinem Bruder Marc und meiner Schwägerin Julia, ihr wart immer eine große Stütze und immer für mich da. Das Gleiche gilt für Brigitte und Thomas, die mir immer mit Rat und Tat zur Seite standen.

Vielen Dank euch allen!

Niklas

Abstract

In zeolites, liquid water creates an ionic environment via the formation of hydrated hydronium ions in the negatively charged framework. Hydronium ions on tungsten oxide surfaces are constrained in a support dependent electrical double layer. Both types of ionic environment impact during acid catalyzed reactions on the chemical potential of reacting molecules leading to a remarkable difference in reaction rate. In apolar solvents, Brønsted and Lewis sites contribute to the elimination reaction.

Kurzzusammenfassung

In flüssigem Wasser entsteht in Zeolithen aus Hydronium-Ionen und dem negativ geladenem Gitter eine ionische Umgebung. Über Wolframoxiden sind Hydronium-Ionen in der elektrochemischen Doppelschicht begrenzt. Beide Arten der Ionenkonzentration haben durch Beeinflussung des chemischen Potenzials des reagierenden Moleküls einen signifikanten Einfluss auf die Rate der Alkoholdehydratisierung. In apolarer Umgebung katalysieren sowohl Brønsted- als auch Lewis-Säuregruppen die Eliminierungsreaktion.

List of abbreviations

BAS	Brønsted acid site
BEA	Zeolite framework type code: Beta
c	Concentration
CyOH	Cyclohexanol
θ	Coverage
E_A	Activation barrier
EFAL	Extra-framework aluminum
FAU	Zeolite framework type code: Faujasite
$\Delta G^{\circ\ddagger}$	Standard Gibbs energy of activation
GS	Ground state
H	Planck's constant (6.6261×10^{-34} J·s)
$\Delta H^{\circ\ddagger}$	Standard enthalpy of activation
IR	Infrared
I	Ionic strength
kJ	Kilojoule
K	Equilibrium constant
k	Rate constant
k_B	Boltzmann's constant (1.3807×10^{-23} J·K^{-1})
K_s	Setschenow constant
K_{ad}	Adsorption constant
l	Liter
LAS	Lewis acid site
γ	Activity coefficient
M	Molar
m	mass
mL	Milliliter
McyOH	Methylcyclohexanol
MFI	Zeolite framework type code: Mordenite inverted
mol	Molar amount (6.022×10^{23} mol^{-1})
n	Reaction order
n	Mols
p	Pressure
ppm	Parts per million (10^{-6})
pyr	Pyridine
Q_{ad}	Adsorption heat
R	Universal gas constant (8.3145 J·(K·mol)$^{-1}$)
r	Observed reaction rate
s	Second
$\Delta S^{\circ\ddagger}$	Standard entropy of activation
SI	Supporting Information
T	Temperature
t	Time
TOF	Turnover frequency
TS	Transition state
V	Volume
WO_x	Tungsten oxide
μ	Chemical Potential

Table of Contents

1) Introduction: Refineries

Crude oil is transported to Germany via cross-border pipelines coming from Trieste, Rotterdam, or soon Nordstream 2. Alternatively supertankers introduce their load to a national pipeline system starting from Germany's international cargo harbors.[1,2] Refineries are placed strategically among the country to upgrade the crude oil depending in the demands of the nearby industry. In general one can subdivide refineries in focus on fuel-production, such as gasoline, kerosine or diesel, or on the production of chemical platform molecules.[3]

1.1) Concepts of modern refineries

Fuel-focused refineries typically provide mixtures of hydrocarbons: liquid gas, which chemical composition is determined by the customer climate due to it's low boiling point of <20°C; light (20-75°C) and heavy (75-175°C) naphtha, jet fuels (175-225°C) and other high boiling residues (heating oil, lubricants and bitumen).[3] Independent of the type of refinery, the crude oil is introduced to a distillation unit that typically consist an atmospheric distillation and a vacuum distillation column (Figure 1.1).[4] Before distillation the oil is desalted with water in an extraction step to avoid corrosion in the downstream units.[5] 20 000 - 30 000 t d^{-1} of crude oil can be processed in most known distillation columns, that are composed of up to 60 separation stages.[3] Pre-heating of the feeds is achieved by heat exchangers that take advantage of hot product streams and face the heat conservation of the unit.[6] The inlet temperature of the bi-phasic (gas and liquid) crude oil feed to the atmospheric column is ~350°C.[3] Within the column multicomponent interphase mass transfer is a common phenomenon and realized with tray columns or packed columns to achieve an enhanced fractionation.[5] Depending on the boiling points the above mentioned fractions are separated and isolated. The atmospheric residue is redistilled in vacuum (40-70 mbar) at around 400°C to achieve a maximum yield of low boiling chemicals and feeds that can be upgraded downstream in cracking units.[3,5] The goal of any refinery is to limit the amount of short residue that is ending up as bitumen, asphaltenes and heavy heating oil.

High boiling molecules can be converted to low boiling and middle distillate fractions via cracking processes.[7] One distinguishes between thermal cracking, hydrocracking and catalytic cracking.[3] Thermal cracking is based on radical reactions at temperatures of around 500°C.[5] The major impacts on the thermal process are the feedstock quality, temperature, pressure and residence time. Most critical is the residence time at a given temperature that determines the fractions of volatile gases and coke.[5] Within the cracking unit, large oil molecule are thermally decomposed into low-boiling molecules that can undergo recombination reactions with other reactive molecules, polymerize or form coke.[8] Both hydrogenation and dehydrogenation reactions may occur, producing (di)-olefins, paraffins, polymers and hydrogen.[5] Larger molecules formed during thermal cracking can be recycled to achieve a maximum yield of the desired product feed. However, the selectivity of thermal cracking units is a major drawback.[4] E.g. the well-known Visbreaking technology, reducing the viscosity of the heavy oil at temperatures of 470-495°C, gives only 10% conversion of the feeds on products in the boiling range of ~220°C.[5] Delayed and fluid coking, that are alternative approaches of thermal cracking have the prime purpose to run residues and heavy oils at harsher conditions 480-565°C until full conversion, but yield coke up to 20-40 wt.%.[5]

Yield and quality of the primary feed can be significantly optimized when applying catalytic cracking, rather than thermal cracking, to a variety of feedstocks ranging from gas oil to heavy crudes and residues.[3] While thermal cracking is a process not employing a catalyst, but free radical reaction mechanisms, producing moderate yields of gasoline with low octane numbers and other distillates, the catalytic cracking makes use of a catalytic material that favors ionic reaction mechanisms leading to high yields and selectivity of gasoline with high octane numbers and other distillates.[5] Well known catalysts are X- and Y-zeolites, as well as ZSM-5, that achieve higher reaction rates, a higher fraction of C_3/C_4-hydrocarbons and highly branched molecules.[3] Catalyst materials for FCC have to withstand physical impacts, thermal shocks and action of oxygen-containing compounds such as CO_2 and air, or other potential catalyst poisons introduced by the heteroatom containing cracking feedstock.[5] Commercially applied cracking catalysts are insulating mixed oxides possessing strong acidic functions located in micro- and mesopores.[5] The pore size and external surface area of the zeolite is an additional parameter affecting the overall conversion due to mass transport limitations, pore blocking and subsequent coking.[9] Coking is, similar to thermal cracking, a major problem, with the difference that the coke is mainly recognized on the catalyst surface, blocking the catalyst pores and deactivating the zeolites.[4] The most widely used process is fluid catalytic cracking (FCC) that is characterized by the fluidized catalyst powder moved through the typical riser-reactor.[3] The solid particles are of such a size that when aerated with air or hydrocarbon vapor, the catalyst behaves like a liquid making it more convenient to flush it through the pipes.[5] The actual cracking reaction takes place in the reaction chamber where the catalyst is dispersed in the vaporized feedstock.[4] A very established approach for maintaining catalyst activity in FCC is the reactivation of the catalyst, by combusting the coke in a coupled regeneration unit.[3] On top of the riser, the catalyst is separated via centrifugal force in cyclones and introduced to the regeneration unit in which the coke is combusted in air (>600 °C).[3,7] The cracked hydrocarbons are separated in a fractionator and further treated downstream. The catalyst material is then reintroduced to the process ensure continuous operation of the unit.[7] Cracking, being an endothermic process requires a continuous heat supply, that can be realized by taking advantage of the exothermic coke combustion along with the catalyst regeneration.[5] The main products of an FCC unit are gasoline (~47%), middle distillate (~20%), gases (~21%), high boiling molecules (7%) and coke (5%).[3] Critical process parameters affecting the product selectivity's and feed conversion are temperature and residence time rather than unit pressure, since substantial increase in pressure is required to significantly increase conversion, while temperature has a primary effect on the rates of the endothermic cracking reactions.[5] A secondary temperature effect is the enhanced cracking rate over the hydrogen transfer reactions leading to an increased amount of olefines in the gasoline and the gas fraction.[5] However, most critical is the contact time by adjusting fresh feed rate, riser steam rate and recycle rate, that are directly affecting the conversion level, but can lead to undesired gasoline overcracking forming LPG.[5]

A very expensive but important alternative to FCC is the principle of hydrocracking to convert higher hydrocarbons under H_2-atmosphere to short alkenes and after immediate hydrogenation to alkanes.[3] By adjusting the severity one can yield various product distributions from the exact same feed, which makes this process very attractive. Temperatures of 300-450°C and H_2-pressures of 100-200 bar make this process very costly, but introduction of green hydrogen (H_2 coming from renewable feedstocks), replacing conventional “grey hydrogen”, can lower the running costs due to subsidies from the governments.[3,10] To achieve the cracking and hydrogenation chemistry, a bi-functional catalyst (acidic function: Al_2O_3, SiO_2/Al_2O_3 or zeolites; metal function: Ni/Mo, Ni/W or Pt/Pd), are used in this process.[7] The mechanisms in hydrocracking are similar to that of FCC, but with an external hydrogen source, that hydrogenates quickly the generated olefin intermediates formed via the carbonium ion chemistry.[5] The high H_2-pressures prevents the catalyst blocking by the olefin and the further dehydrogenation to coke.[5] In the future, refineries will face and process an increased amount of heavier feeds making hydrocracking units an essential part of every refinery. However, the increasing throughput requires a more climate-neutral source of hydrogen, as most refineries have only an “in-house” primary source of hydrogen coming from the steam reformers or catalytic reforming units.[11]

Secondary refinery products such as straight-run gasolines and napthas are upgraded to high octane aromatics and branched alkanes. Typical reactions are the isomerization, the dehydrogenation of naphtenes to aromatics or dehydrocyclization of paraffins to napthenes.[3] One valuable side product of dehydrogenation reactions is H_2, which can be separated and introduced in the hydrocracker.[5] Similar to the hydrocracking process, a bi-functional catalyst is needed to catalyze efficiently the acid assisted reforming steps.[3] Coking reactions can be suppressed by applying high hydrogen pressures (8-15 bar) but as dehydrogenation reactions are strongly endothermic, note the unit pressure is critical, but the heat supply is essential.[5]

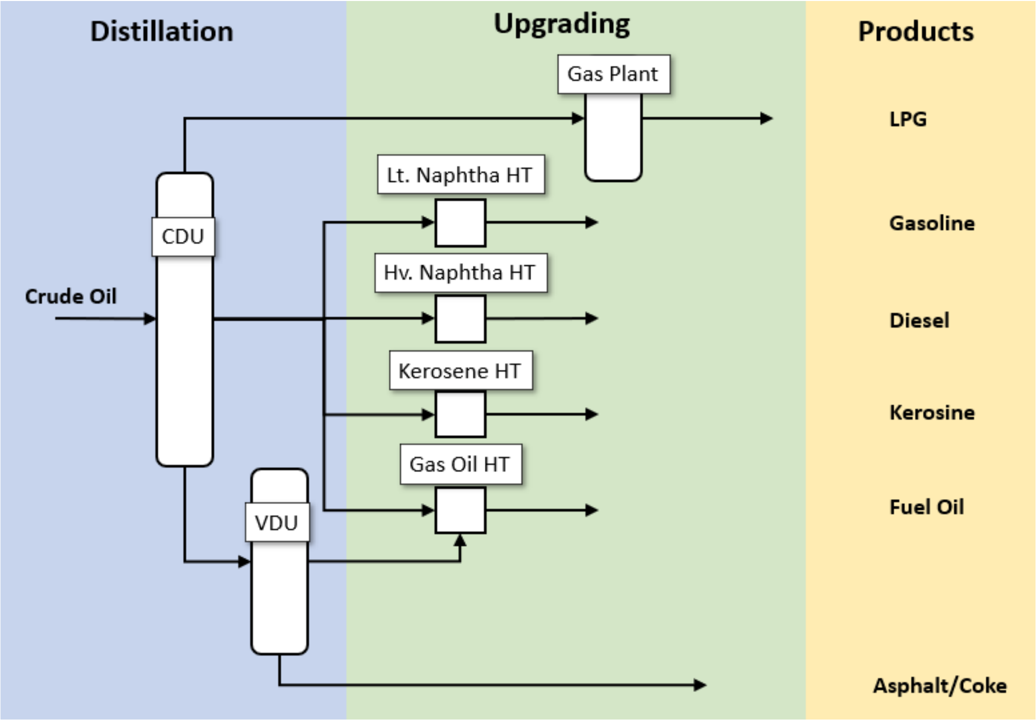

Figure 1.1 *Simplified process scheme of a typical refinery (adapted from ref. [12]) including Crude distillation unit (CDU) and vacuum distillation unit (VDU), Hydrotreater (HT)*

Due to the very cost-intensive shut-down of refinery units for catalyst exchange, the main goal in refineries is to prolong the lifetime of the catalysts. One basic protocol to achieve enhanced catalyst lifetime is the removal of heteroatoms of the crude oil feed.[3] The feed entering the distillation unit typically is composed of 83-87 wt.% carbon, 10-14 wt.% hydrogen and heteroatoms causing catalyst deactivation (0.1-2 wt.% nitrogen, 0.05-6 wt.% sulfur, 0.05-1.5 wt.% oxygen).[4] Additionally, low amounts of metals (>300 ppm) are known to be part of the feed and cause undesired catalyst deactivation.[5] The selective removal of heteroatoms is on the one hand necessary for the units healthiness and productivities and on the other hand to fulfill the product requirements for gasoline and diesel with regard to NO_x and SO_x emissions.[12,13] Hydrotreating units guarantee sulfur, nitrogen and oxygen removal in the presence of high hydrogen pressure and are placed strategically at several process positions in a refinery.[12] Hydrotreater additionally ensure a partial hydrogenation of highly unsaturated feeds to avoid downstream coking and at severe conditions hydrocracking takes place as the upper limits of hydrotreating conditions may overlap with the lower limits of hydrocracking conditions.[5] Hydrotreatment is carried out before, rather than after catalytic cracking as the products require less finishing, corrosion and coke formation are reduced and thus higher conversions are achievable.[5] Classical catalysts for hydrodesulfurization (HDS) and hydrodenitrogenation (HDN) are Mo supported on alumina (Al_2O_3) catalysts with either Ni or Co as promotor metal depending on the requirements on the hydrogenation activity.[14] Molybdenum, cobalt and nickel are the most widely used metals for HDS and HDN reactions, impregnated on the support material in the oxide form and sulfided in H_2S flow prior to the use or during the actual run-time.[4] “Easy-to-process”-feeds usually require a mild hydrogenation activity for an efficient heteroatom removal, so in particular Co-Mo/Al_2O_3 catalysts are used for straight-run petroleum fractions.[4] On the other hand, the upgrading of residues requires a high hydrogenation activity to first hydrogenate the aromatics to eliminate steric hindrances, before cleaving the carbon-heteroatom bonds.[4] Thus, Ni-Mo/Al_2O_3 is known to process refractory feeds more efficiently. A typical hydrotreating feed is composed of saturated alkanes and cycloalkanes, unsaturated molecules as olefins and aromatics and the critical sulfur- or nitrogen-containing compounds such as thiols, thioesters, thiophenes, amines, pyridines and quinolines.[4,15] Oxygen-containing molecules become more interesting when introducing drop-in fuels, which is described in more detail later in this section, but in normal crude oil feeds, the concentration of phenolics or carboxylic acids are rather low (<0.1 wt.%).[12] N-containing molecules deactivate hydrotreating catalysts due to their basicity with a high adsorption constant.[16] However, due to the high sulfur content in crude oil, the HDS reaction is most dominant in today’s refineries.

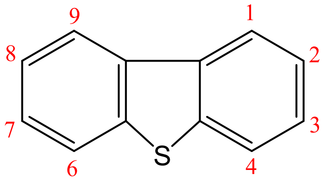

Figure 1.2 *Molecular structure of dibenzothiophene (DBT)*

The chemical structure of the S-containing molecule is known to be more important than the actual S-content, as the local structure around the heteroatom has direct impact on the reactivity.[17] For example the reactivities of 4-alkyl- and 4,6-dialkyl-dibenzothiophenes are significantly decreased when compared to the non-substituted molecule (Figure 1.2).[18] Steric and electronic effects, such as the accessibility of the S-atom, the adsorption mode (flat or perpendicular) or the π-electron system, are directly affecting the C-S cleavage rate.[19] Simple thiols react via β-hydrogen elimination of H_2S and subsequent hydrogenation to the olefin, thiophenes require prior to the C-S bond rupture a hydrogenation of the double bonds and benzothiophene, composed of unsaturated π-electron systems, can react either via hydrogenation route (HYD) or via direct desulfurization route (DDS) as depicted in Figure 1.3.[19,20] The unruliness, meaning the fraction of refractory compounds, of the hydrotreating feed determines the dominant reaction route. E.g. in 4- and 6-position substituted dibenzothiophenes (DBT) the adsorption in σ-mode is much weaker than that of unsubstituted DBT and the DDS pathway is strongly suppressed.[19] However, hydrogenation of the aromatic ring system of alkyl-substituted DBP in a flat adsorption mode is not influenced by the geometric constraints, but results in a reduction of steric hindrance and easier access of the sulfur atom.[21] Hence, these molecules react selectively via the HYD-route, which drastically increases the consumption of hydrogen for complex feedstocks.[22] Unsaturated DBT, on the other hand, reacts at high temperature selectively (up to 40% at 330°C) via the DDS route to biphenyl.[23]

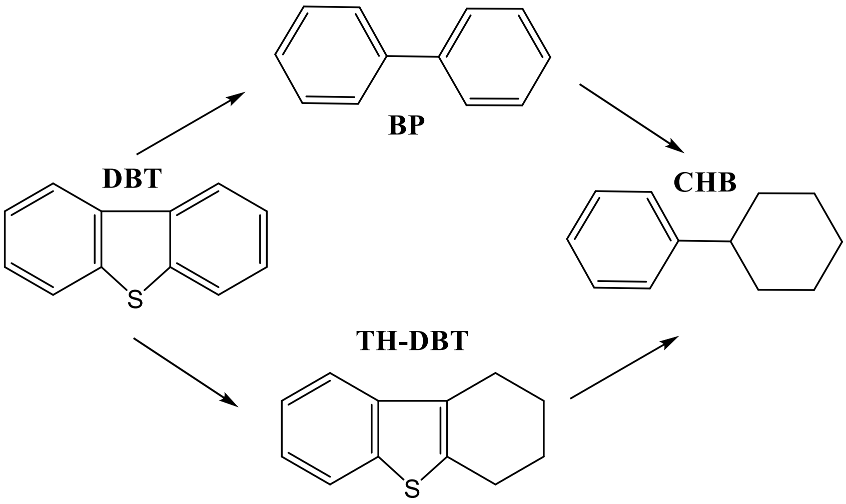

Figure 1.3 *Reaction network of the HDS of dibenzothiophene (adapted from ref.[24])*

The hydrodesulfurization reactions are significantly affected by N-containing molecules as pyridines and piperidines strongly suppress the hydrogenation pathway and simultaneously inhibit the direct desulfurization route.[24] On the other hand, H_2S has a positive effect on the HDN of pyridines, while S-containing dibenzothiophene shows not a significant impact on the C-N bond cleavage rate.[24] Thus, the cleavage of the different heteroatoms (S and N) takes place at different active sites, whereas the hydrogenation sites for N- and S-containing molecules may be the same.[24] The nitrogen removal of simple amines proceeds either via an S_N2 substitution process or if sterically hindered (e.g. 2,6-dimethylpiperidine) by an E_2 elimination.[25] HDN of more complex benzo(a)carbazole and benzo(f)quinoline usually requires a saturation of the π-electron system prior to the C-N cleavage step, due to the strength of the unsaturated C=N bond.[4] Thus, a direct denitrogenation is not possible (Figure 1.4). E.g. the N-removal of quinoline was found to take place via the saturated intermediates decahydroquinoline and propylcyclohexylamine, or via the aromatic intermediates 1,2,3,4-tetrahydroquinoline and ortho-propylaniline.[26] Due to the required hydrogenation steps, catalysts need a strong hydrogenation affinity and the HDN reaction is due to it's high H_2-consumption a very costly process.

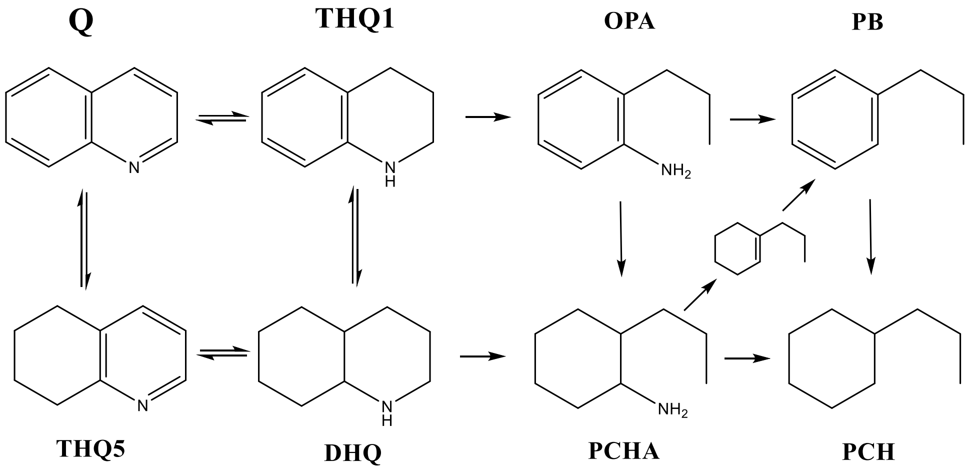

Figure 1.4 *HDN reaction network of quinoline (Q). The nomenclature is THQ5: 5,6,7,8-tetrahydroquinoline; DHQ: decahydroquinoline; THQ1: 1,2,3,4-tetrahydroquinoline; OPA: ortho-propylaniline; PCHA: 2-propylcyclo-hexylamine; PCHE: propylcyclohexene; PB: propylbenzene (adapted from Ref.* [26]*)*

1.2) Future challenges and decarbonization approaches

As mentioned already the hydrogen consumption in many processes of a refinery is a cost intensive factor. Therefore, refineries can either fall back on classical (grey) H_2-production processes such as steam reforming of light hydrocarbons, partial oxidation of hydrocarbons into a gas mixture rich in H_2, hydrogen recovery processes from refinery off-gases (Table 1), or - most promising - incorporate green hydrogen to their balances.[5] Hydrogen production concepts with zero or low environmental impact ("green") process all CO_2 and other pollutants when extracting the H_2.[27] Currently the most popular strategy for almost pure H_2 production is water electrolysis, based on the movement of electrons supported by an external circuit.[27] Other processes include the plasma induced decomposition of natural gas (CH_4 reacts to $C_{(s)}$ and H_2; 100% carbon yields, no CO_2 release),[28] photonic energy based hydrogen production (photocatalysis, photoelectrochemical method, and artificial photosynthesis), thermochemical water splitting and hybrid thermochemical cycles.[27] Since 2018, ITM power together with the

Shell Rhineland Refinery in Wesseling, Germany, operate the world's biggest H_2-electrolyzer for clean refinery-hydrogen. The unit is equipped with a polymer-electrolyte-membrane-technology (PEM) producing up to 1.300 t (H_2) a^{-1}.[29]

Table 1.1 *Hydrogen concentration in refinery off-gases (from Ref. [30])*

Process	H_2-content (vol. %)
Catalytic reforming	40-85
Catalytic cracking (off-gas)	10-30
Hydrocracking (off-gas)	40-60
Hydrotreating (purge)	25-35
Thermal hydrodealkylation	50-75
Hydrogenation (purge)	85

Besides focusing on "green" hydrogen, achieving emission reduction and climate mitigation goals is becoming a key objective of most refineries. An alternative decarbonization approach for petroleum based refineries is the insertion of drop in fuels. [31] Biofuels have been defined as functionally equivalent to petroleum-based transportation fuels and are more or less compatible with the existing refinery infrastructure.[31] Currently, conventional drop-in biofuels are based on lipids or oleochemicals, but renewable feedstocks such as lignocellulosic agricultural residues or other waste biomass are most promising future feedstocks.[32] The high oxygen content of the bio-oil is most obstructive as the more reactive and corrosive intermediates, as well as the immiscibility with petroleum based feeds require new process protocols.[33,34] Biocrudes that might be upgraded at a refinery will contain larger molecules composed of phenols, catechols, guaiacols or syringols if based on lignocellulosic feedstocks.[31,35] Typical upgrading reaction for such classes of molecules are decarboxylation (O removed as CO_2), decarbonylation (O removed as CO), and hydrodeoxygenation (O removed as H_2O).[31,36] Figure 1.5 (A) demonstrates that an increased demand of hydrogen is required in upgrading of low H/C-feedstocks, promoting the hydrodeoxygenation reaction and increasing the operation costs for drop-in biocrudes based on lignin.[31] Oxygen-containing gaseous products such as carbon dioxide and monoxide being formed in the decarboxylation and decarbonylation reaction are undesired loss of carbon. Not only the actual oxygen content of the bio-oils is challenging for the current refinery infrastructure but also the functionality of the organic compounds, including organic acids, aldehydes, ketones, and oxygenated aromatics, determines the chemistry and make insertion to existing infrastructure challenging.[37]

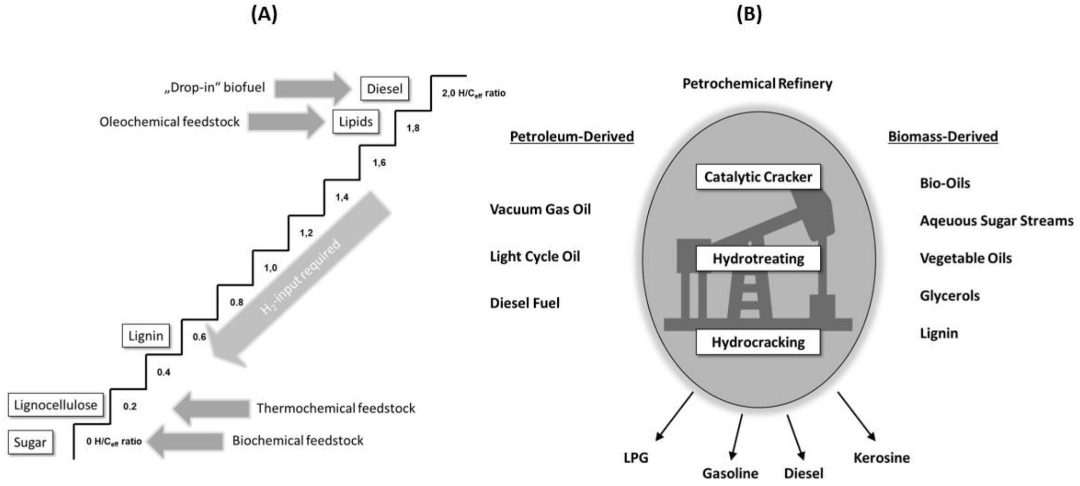

***Figure 1.5 (A)** The effective hydrogen to carbon ratio ‘staircase’ for feedstocks (adapted from Ref. [31]) and **(B)** the conversion of petrochemical- and biomass-derived feedstocks in a petroleum refinery (adapted from Ref. [36])*

Potential insertion points into already existing refinery infrastructure have to be carefully evaluated. The conversion of biomass-derived feedstocks is achieved most efficiently in catalytic cracking, hydrotreating and/or hydrocracking units due to their respective properties (Figure 1.5 (B)).[31,34,36]

1.2.1) Insertion points of biocrudes to the current refinery-infrastructure

Insertion of biocrudes to a conventional FCC unit yields large amounts of coke, but is economically very promising as no external hydrogen is needed for the cracking of large bio-molecules, the investment costs are low and the oxygen tolerant catalyst is continuously reactivated.[31] Coke can either be used to provide process heat or can be converted into syngas through steam or CO_2-reforming.[36] Depending on the source of renewables, the potential product stream will be enriched of aromatics, as phenolics represent a large fraction of pyrolysis bio-oils.[38] Aromatics unlikely undergo any cracking reactions and the removal of oxygen results in the consumption of hydrogen originated from the hydrocarbon, yielding consequently more higher unsaturated olefins or aromatics.[31,37,39] Opposite to the coke-tolerant catalyst recycle in FCC, the risk of permanent catalyst deactivation associated with insertion of unknown or complex feeds is much greater for hydrotreating units.[31] However, the major advantage of the hydrotreater being the insertion point is that the oxygen-atom, even if located in polyaromatic structures, can be removed selectively under H_2-atmosphere analogous to

HDS and HDN reactions, over cobalt molybdate catalyst.[5] Note, even at high hydrogen pressures the removal of oxygen will not exclusively proceed via hydrogen addition, but also via formation of CO and CO_2 causing enhanced catalyst deactivation.[31] Similar to hydrotreating, the hydrocracking unit operates under high hydrogen pressure and is able to deoxygenate the biocrudes with it's current infrastructure. The hydrocracking catalyst, however, due it's bifunctionality is very sensitive to oxygen-containing feeds that may oxidize their expensive noble metals such as palladium (Pd) or platinum (Pt).[31] Hence, hydrocracking may be used as upgrading process downstream of hydrotreating where size reduction of bio-molecules is still required.[31]

The great potential of drop-in fuel insertion to existing petrochemical infrastructure is best shown by Neste Oil, using a modified hydrotreating process to convert triglycerides to diesel fuel, marketed as NExBTL fuel.[36,40] Hydrotreating of vegetable oil results in appreciable fuel properties and is currently more promising than biodiesel based on agricultural waste.[36] The cetane number, a quality feature for diesel, of hydrogenated vegetable oil is increased by ~50% when compared to biodiesel and the oxygen content can be reduced to a minimum (~0 wt.%).[36] Compared to alternative sources, such as microalgae, cellulose and waste agricultural biomass, vegetable oils have a higher energy density and easy handling for processing in large-scale production with already existing infrastructures.[41] Note that more common is the transesterification of vegetable oils such as soybean, sunflower or palm for the production of biodiesel, being similar to conventional diesel with fossil origin.[42] The direct insertion of biofuels from lignocellulose (biomass to liquids) without any pretreatment to conventional refineries is, due to the complex structure of cellulose, hemicellulose and lignin polymers, currently not possible.[34] Thus, the following section briefly summarizes common pretreatment strategies.

1.2.2) Pretreatment strategies for bio-based feedstocks

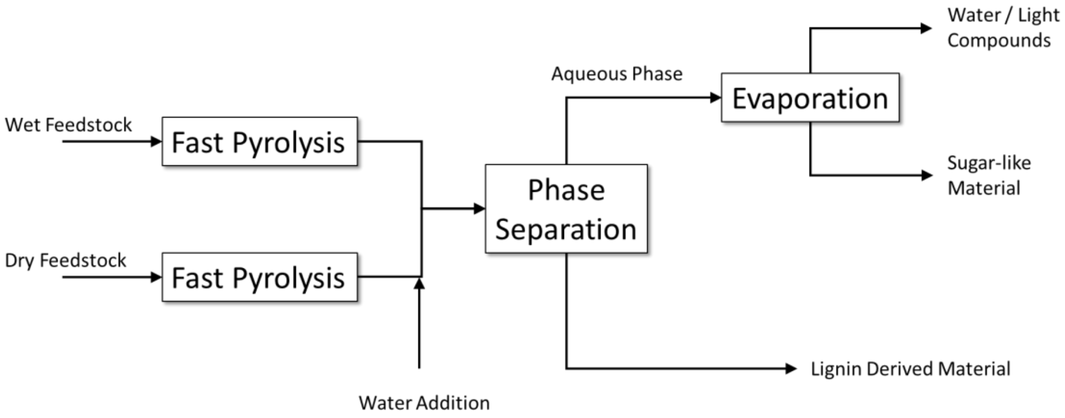

Figure 1.6 *Fractionation scheme for bio-oil phase separation (adapted from Ref. [43])*

Crude oil distillation is the major separation technique in petroleum refineries, as volatile molecules are involved, but the main fraction of biomass components are non-volatile and thus, solvent-based extraction, chromatography or membrane separation are required.[34] Consequently, these feedstocks are upgraded in advance in biorefineries, via pyrolysis, extracted and fractionated (Figure 1.6).[43]

Figure 1.7(A) and (B) depicts the complex molecular structure of lignin polymers, consisting of randomly cross-linked phenyl propane’s, most likely substituted coumaryl alcohol, coniferyl alcohol and sinapyl alcohol.[44,45] Hence, degradation and depolymerization of lignin to fine chemicals is very challenging. Despite the classical approaches of lignin pyrolysis (thermolysis), gasification, hydrogenolysis, chemical oxidation, and hydrolysis under supercritical conditions, much research was done to find elegant protocols for lignin upgrading and most popular are the transition metal catalyzed reduction or oxidation of C–O bonds, the visible light mediated reduction or oxidation of C–O bonds and the redox-neutral conversion of lignin.[44,46] Hydrolysis as well as photocatalytic methods use or allow water as solvent to break down the linkages.[44,46] The liquid oil products can be classified in water soluble phenols (guaiacols, catechols, syringols and cresols), aldehydes and water-insoluble aliphatic molecules (e.g. alkanes, methane, ethane).[46] Conventional cheap solvents for the extraction of phenolic monomers are water[47-49] and water/alcohol mixtures[50,51] that work as hydrogen supplier when introducing a transition metal catalyst for delignification (up to 94% conversion).[52,53] In a secondary upgrading process the hydrodeoxygenation reaction is carried out in the same solvent removing oxygen from the lignin-derived phenolic monomers to obtain chemicals that can be used as fuel or fuel additives.[54]

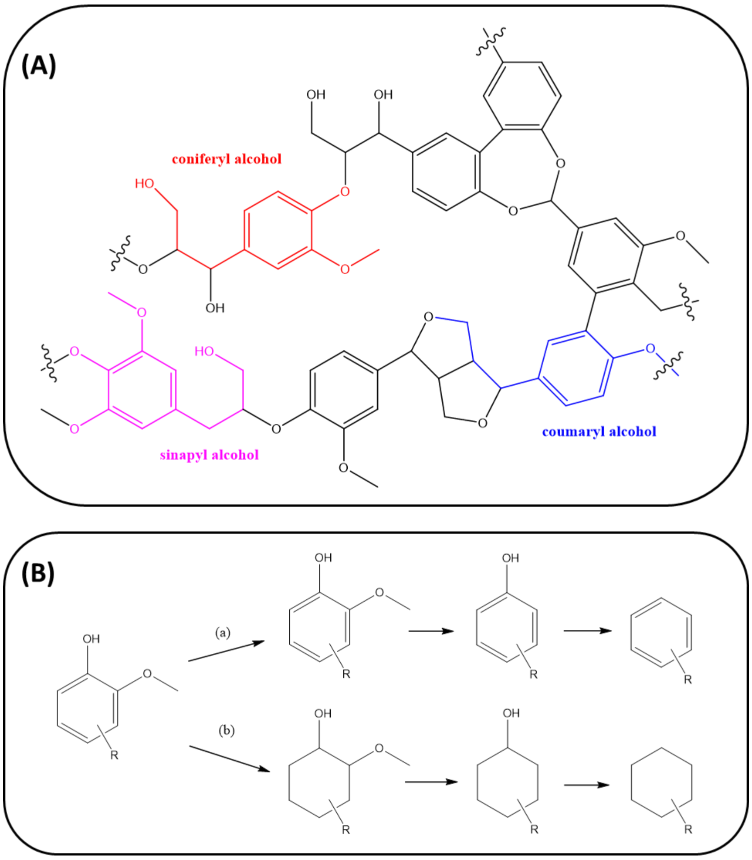

Figure 1.7 (A) *Schematic representation of a lignin polymer (adapted from Ref.*[44]*) and* ***(B)*** *HDO of a lignin-derived monomer via (a) hydrogenolysis and (b) hydrogenation–deoxygenation (adapted from Ref.*[55]*)*

An alternative pretreatment of biooil is the phase separation by water addition, yielding a water-insoluble fraction derived mainly from phenolic lignin at the bottom and a water-soluble fraction rich in carbohydrates at the top.[43,56] Typically bio-oil produced from dry raw material contains already 25-30 wt.% of water, but phase separation begins after exceeding 30 wt.% water content, so the moister is adjusted depending on the feedstock.[43] The addition of salts (LiCl, $CaCl_2$, $FeCl_3$, $(NH_4)SO_4$,K_2CO_3, and $Fe(NO_3)_3$), or their respective salt solutions will enhance phase separation drastically.[57] Depending on the feedstock, the top layer (40-80 wt.%) exhibit high contents of water, acetic acid and other water-soluble molecules like furfural, phenolics and their derivates.[57] The complex lignin derived materials that are water insoluble (Figure 1.5) can be either upgraded via harsh hydrotreating and/or hydrocracking breaking down linkages and reducing molecular size, or can be used e.g. as an organic binder (binder supplemented with 10–15%).[58] The water-soluble fraction can be concentrated by evaporating water and volatile compounds in vacuum, yielding a sugar-like fraction (water content of 6.3 wt % and a pH of 2.2) and an aqueous phase (95.8 wt % H_2O, pH 2.2) as distillate.[43] So far, much research is done investigating the aqueous phase upgrading of water-soluble bio-based molecules via (hydro-)deoxygenation in an acidic environment [45,59-65] and over supported transition metal catalysts.[66-70] However, industry-like solutions contain various impurities such as inorganic salts that can alter the acid catalysis in aqueous phase. It is known that the phase separation,[71] the catalyst stability[72] and the intrinsic rates[73-78] are impacted by the salt concentration, and consequently change the apparent reaction kinetics. As biomass in general contains a significant amount of inorganic compounds[79] such as chlorine, calcium, potassium, or sodium, the potential for a significant improvement is visible and thus, this work will among others discuss the effect of non-ideality induced by ionic strength. As a model compound this dissertation focuses mainly on cyclohexanol, being a undesired oxygen-containing product from the HDO of phenolic compounds (Figure 1.7 (B)).[55]

1.3) Mixed oxide catalysts for reactions in solution

The design and the structure of effective catalysts targets a maximum number of well distributed active sites accessible for the reaction substrate, that is determined by the geometry of the accessible catalyst volume.[3] Deactivation of solid catalysts is mainly caused by thermal degradation (or sintering), fouling (e.g. coking), poisoning, volatilization of active catalyst agent(s), or leaching.[80] In general one can classify the catalyst deactivation in physical, thermal and chemical nature, leading to lack of accessibility or loss of active sites, a decreased number of exposed sites, or a decline of intrinsic activity.[81] Leaching of the active phase and thermal degradation are particularly problematic because of its irreversibility and thus, the catalyst design for a specific reaction under particular reaction conditions is a key element of process design.

A well-established class of solid catalysts are zeolite materials, being microporous crystalline aluminosilicates, applied in particular as zeolite Y and ZSM-5 in the fluid catalytic cracking (FCC) process.[3] Characteristic for zeolites is the Si/Al-ratio, it's acidity and the shape selectivity given by the microporous network of cavities.[82] Aluminosilicate zeolites are most generally defined by their 3-D and regular framework formed by linked TO_4 tetrahedra (T = Si, Al), each oxygen being shared between two T elements, and their channels and cavities with molecular sizes which can host the charge compensating cations, water or other molecules and salts.[83] Weitkamp [83] describes the composition as

$$x_1 \cdot M_1^{n_1^+}, x_2 \cdot M_2^{n_2^+} \left[(y_1 \cdot T_1, y_2 \cdot T_2 \ldots) O_{2(y_1+y_2+\cdots)}\right]^{x-} z_1 \cdot A_1,\ z_2 \cdot A_2, \ldots$$

- M_1, M_2, cations with charge n_1, n_2 which compensate the negative charge of the framework ($x_1n_1 + x_2n_2 + \ldots = x$)
- T_1, T_2 ... , elements (Si,Al...) in the tetrahedra
- A_1 A_2 ... , water, molecules, ion pairs.

and further classifies zeolites with low Si/Al ratio (<5), with medium (5-10) and high Si/Al ratios (>10), achieved by the replacement of the silicon by aluminum.

Zeolites have a wide range of applications, represented by a worldwide consumption of synthetic zeolites of about 1.7–2 million metric tons per year, and in detail, FCC catalysts (primarily USY zeolite) constitute more than 95% of zeolite catalyst consumption.[84] Classical applications of microporous zeolites are exhaust gas treatments, as well as absorption and adsorption processes.[3,85] Nowadays most petrochemical processes make use of microporous crystalline aluminosilicates, e.g. cracking over zeolite-Y, hydrocracking and isomerization over bifunctional zeolite-Y, alkylation over La-Y, or Mobil-oil processes (MTG, MTP, MTA) over ZSM-5.[3] Other applications for zeolite-catalyzed processes are hydroxylation (e.g., phenol), alkylation (e.g., ethylbenzene, cumene), oximation (e.g., cyclohexanone oxime) and epoxidation (e.g., propylene oxide) that are mainly carried out in Japanese industry.[84] The catalyst for the respective processes is chosen based on distinct structural, morphological and compositional characteristics of the zeolite and the needs/limitations of the reaction.[84] A wide range of structures is possible by incorporating template molecules to the synthesis, contributing via bond formation to the stability of the solid and controls the formation of a potentially microporous framework structure.[83] Typical zeolite pore sizes include: (i) small pore zeolites with 8-membered ring, free diameters of 0.30 – 0.45 nm (e.g., zeolite A), (ii) medium pore zeolites with 8-membered ring, 0.45 – 0.60 nm (ZSM - 5), (iii) large pore zeolites with 12-membered ring 0.6 – 0.8 nm (e.g., zeolites X, Y) and (iv) extra-large pore zeolites with 14-membered ring pores (e.g., UTD-1).[86]

For acid base catalysis, as also studied in this dissertation, acidic sites such as acidic OH groups (Brønsted acid centers), true Lewis sites (aluminum-containing extra-framework species) and cations as well as basic sites (such as basic oxygen atoms or alkaline metal clusters) are of major importance.[83] The generation of acidic sites is typically caused by the substitution of Si^{4+} with a metal ion (M^{4+}) during direct hydrothermal synthesis or post-modification.[87] The occupation of the framework T-site (tetrahedral lattice Si or Al atom) by Al is governed by the particular synthetic method and the distribution of Al can markedly vary depending on the Si/Al ratio.[88] The introduction of a negative charge onto the framework by a trivalent aluminum results in a charge compensation by cationic species compensating for the negative lattice charge.[88] In the case of protons compensating the charge, Brønsted acid sites (BAS) are formed.[88] The catalytic activity of BAS confined in zeolite pores is determined by the surrounding zeolite matrix, meaning the physical interactions between the adsorbed molecule and the pore environment that significantly alters the reaction rates, which represents the key difference to homogeneous Brønsted acids.[61,88,89] In addition, the protons structure-activity relation in zeolites is determined by lattice defects and other structural inhomogeneities.[88] On the other hand, one can replace the acidic protos inside the zeolite micropores by other cationic species to create well defined Lewis acid sites and/or redox sites.[88] Alternatively, the Lewis acid density can be tuned by selective lattice modification through isomorphous substitution of silicon atoms (Figure 1.8) in the framework with other tetravalent elements (Sn^{4+}, Ti^{4+}, Zr^{4+}).[88,90] Similar to the BAS reactivity, the activity of Lewis sites is affected by their distribution within the zeolite channels and thus, by local charge distribution, geometrical properties of the confinement space and the chemical properties of the stabilizing zeolite lattice.[88] Both, Brønsted and Lewis sites are most commonly qualified and quantified via ^{27}Al magic-angle spinning nuclear magnetic resonance spectroscopy (probing of coordination structures), FTIR-spectroscopy of the hydroxyl (-OH) groups (nature and strength) and FTIR-spectroscopy using probe molecules (acid type and strength), such as pyridine, substituted pyridine, ammonia, amines and carbon monoxide/dioxide.[83,87]

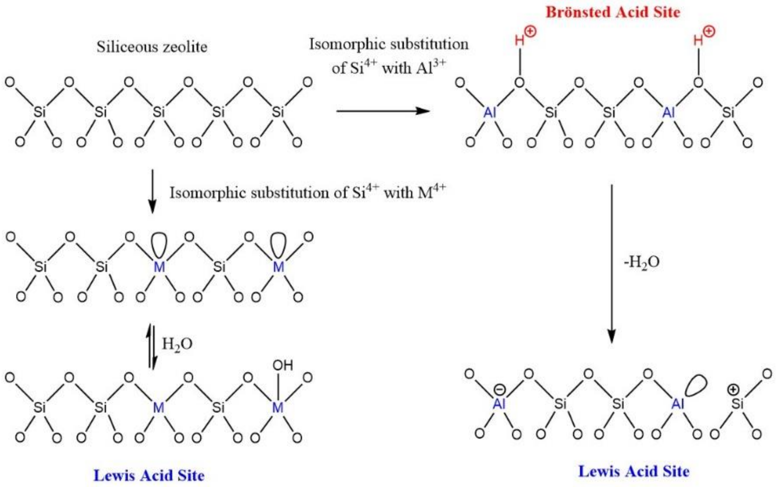

Figure 1.8 *Schematic illustration for structures of Brønsted and Lewis acidity in zeolites. (adapted from Ref.* [87]*)*

For many industrial applications, such as conversions of biomass-derived feedstocks, it is crucial that the catalyst demonstrates a high hydrothermal stability. The insufficient stability of zeolites in hot liquid water is primarily caused by desilication, meaning Si-O-Si hydrolysis leads in aqueous medium to a framework collapse.[91] An increased hydrothermal stability is e.g. achieved when reducing the pore concentration of water in the presence of reacting substrates, which is again determined by the tetrahedral aluminum balancing the hydrated hydronium ions in liquid water.[91] As implied already, the Brønsted acid site changes its nature in the presence of water, as H_2O interacts with the BAS, and converts it into hydrated hydronium ions that stay and distribute within the negatively charged framework.[92] These hydronium ions confined in the pore environment alter markedly the reaction rates of acid catalyzed reactions, when compared to homogenous catalysis, as the association between hydronium ions and alcohols is enhanced and the intrinsic rate constant is increased.[63,65] These insights may allow to understand and predict processes in confined spaces, similar to enzyme catalysis, but do not necessarily make them a good candidate for biomass processing. For example, small amounts of inorganic impurities in the water phase, such as NaCl (0.07–37 wt %), enhance the hydrolysis of Si–O–Al bridges and the release of Al^{3+} species from the zeolite framework.[72] Figure 1.9 demonstrates that zeolites provide a medium hydrothermal stability, while carbon materials and (mixed-)oxides (ZrO_2 and TiO_2) are more promising catalyst materials in hot liquid water.[93]

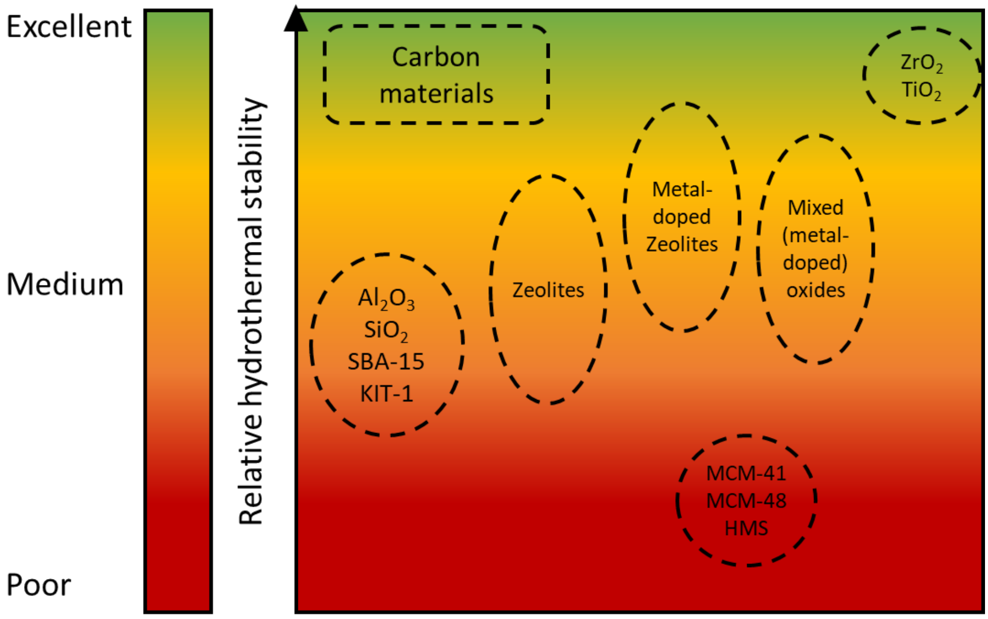

Figure 1.9 *Illustration of hydrothermal stability of heterogeneous catalysts in superheated steam (T> 400 °C). (Adapted from Ref. [93])*

Strategies for improving the hydrothermal stability of heterogeneous catalysts can be (i) doping of the support (e.g. γ-Al_2O_3) with heteroatoms such as La^{3+},Ga^{3+}, Sm^{3+}, Ce^{3+} and Ti^{4+}, (ii) surface modification, e.g. introducing hydrophobic functionalities preventing the direct contact with water bulk or removing hydrothermally unstable surface groups, or (iii) deposition of oxide nanoparticles on a functionalized, high surface area support (e.g. WO_x/ZrO_2, Nb/C), preventing the growth of oxide crystallites (active phase) due to a strong interaction between active phase and support.[93] Tungstated zirconia, alumina or titania (WO_x/ZrO_2) e.g., attracted besides their hydrothermal stability the attention of many research groups, as they also provide both Lewis and Brønsted acid sites for acid catalyzed reactions.[94-97] The surface structure of the active phase (tungsten oxide) is dependent on its surface density on the respective support, revealing maximum dehydration activity at monolayer coverage in gas phase reaction.[94,98] However, physical changes of catalysts during exposure to hot liquid water directly alter the catalytic performance in biomass processing reactions, and only few studies exist targeting such mixed oxides under realistic upgrading conditions. Hence, this dissertation examines suitable mixed oxides, zeolites and carbon-based catalysts for a typical aqueous phase biomass upgrading reaction.

1.4) Chemical kinetics in solution and thermodynamically non-ideal systems

In biomass processing, the solvent may be water containing a significant fraction of ionic species.[79] Therefore, research and especially kinetics take these ions into account and consider them as an non-ideality factor. The following derivations, if not stated otherwise, are based on the references [99-102] and explains how to modify general kinetic formulars if deviating from ideality:

For a bimolecular reaction A + B → P, Madon and Iglesia [101] postulate the reaction rate according transition state theory to be proportional to the number of activated complexes per unit volume ($c^{\ddagger}$) overcoming the activation barrier with a frequency $\frac{\mathrm{k\,T}}{\mathrm{h}}$. Equation (1.1) considers the transition state as a normal molecule. k_B is the Boltzmann's constant, h the Planck's constant and T the temperature.

$$\mathrm{r} = \frac{\mathrm{k_B\,T}}{\mathrm{h}} \mathrm{c}^{\ddagger} \tag{1.1}$$

In the case of a system other than that of an ideal gas, activities are used instead of concentrations.[100] Therefore the equilibrium constant leading to the transition state $K^{\ddagger}$ is defined as

$$\mathrm{K}^{\ddagger} = \frac{\mathrm{a}_{\ddagger}}{\mathrm{a_A\,a_B}} \tag{1.2}$$

and subsequently reformulated when introducing activity coefficients γ, by substituting for activity $a = \gamma \cdot c$ into the equation:

$$\mathrm{K}^{\ddagger} = \frac{\gamma_{\ddagger}}{\gamma_\mathrm{A}\,\gamma_\mathrm{B}} \cdot \frac{\mathrm{c}_{\ddagger}}{\mathrm{c_A\,c_B}} = \exp\left(\frac{\Delta G^{0\ddagger}}{RT}\right) \tag{1.3}$$

Equation (1.3) together with (1.1) gives the expression for a reaction rate under non-ideal conditions (1.4a) and it's corresponding rate constant (1.4b), as well as the rate constant under thermodynamic ideality at infinite dilution $\gamma_i \rightarrow 1$ (1.4c).[100]

$$\mathrm{r} = \frac{\mathrm{k_B\,T}}{\mathrm{h}} \mathrm{K}^{\ddagger} \frac{\gamma_\mathrm{A}\,\gamma_\mathrm{B}}{\gamma_{\ddagger}} \mathrm{c_A\,c_B} \tag{1.4a}$$

$$\mathrm{k} = \frac{\mathrm{k_B\,T}}{\mathrm{h}} \mathrm{K}^{\ddagger} \frac{\gamma_\mathrm{A}\,\gamma_\mathrm{B}}{\gamma_{\ddagger}} \tag{1.4b}$$

$$\mathrm{k_0} = \frac{\mathrm{k_B\,T}}{\mathrm{h}} \mathrm{K}^{\ddagger} \tag{1.4c}$$

The ratio of $\frac{k}{k_0}$ can be taken as a measure of the non-ideality of a system, compared to the corresponding ideal case (Equation (1.5).[100,101]

$$\frac{\mathrm{k}}{\mathrm{k}_0} = \frac{\gamma_\mathrm{A}\,\gamma_\mathrm{B}}{\gamma_\ddagger} \tag{1.5}$$

Activity coefficients can be estimated using the Debye-Hückel theory, which makes use of the ionic strength being a measure of the concentration of charged species in solution.[74,103]

$$\mathrm{I} = \frac{1}{2}\sum_\mathrm{i} \mathrm{c_i} \cdot \mathrm{Z_i^2} \tag{1.6}$$

c_i is the concentration of ion i of charge Z_i. In an environment of a very low ionic strength, activity coefficients can be determined using the Debye-Hückel theory assuming a central ion being surrounded by ions of opposite charge.[74,103] The expression for the activity coefficient following this theory is (with A in water at 298K: 0.51 $\mathrm{mol^{-1/2}\ dm^{3/2}}$)[102]

$$\log(\gamma_\mathrm{i}) = -\mathrm{AZ_i^2}\sqrt{\mathrm{I}} \tag{1.7}$$

This formula is based on the major assumption of low electrolyte concentrations, typically less than 10^{-3} mol $\mathrm{L^{-1}}$. Thus one rewrites equation (1.5) into the form of

$$\log\,(\mathrm{k}) = \log(k_0) + \log(\gamma_\mathrm{A}) + \log(\gamma_\mathrm{B}) - \log(\gamma_\ddagger) \tag{1.8}$$

to yield with (1.9) the final relationship of Brønsted and Bjerrum.[73,104]

$$\log\,(\mathrm{k}) = \log(k_0) + 2\mathrm{AZ_AZ_B}\sqrt{\mathrm{I}} \tag{1.9}$$

An increase in ionic strength leads to higher rate constants for reactions involving substrates/ions of the same charge and decreases the rate when the ions are oppositely charged. Reactions, in which a neutral substrate is involved, do not depend on the ionic strength according to equation (1.9), as Z=0 eliminates the right side of the equation.

For electrolyte solutions with higher ion concentrations, the experimentally determined data deviates from the prediction based on the derived expression (1.9). The major extensions of the Debye-Hückel theory are obtained by the addition of terms, such as

$$\log(\gamma_\mathrm{i}) = -\mathrm{AZ_i^2}\frac{\sqrt{\mathrm{I}}}{1 + \mathrm{Ba_0}\sqrt{\mathrm{I}}} \tag{1.10}$$

with a_0 being the distance of closest approach of ions and the temperature dependent parameters A and B defined as[105]:

$$A = \frac{e^2 B}{2.303 \cdot 8\pi\epsilon_0\epsilon_r k_B T} \tag{1.11a}$$

$$B = \left(\frac{2e^2 N}{\epsilon_0\epsilon_r k_B T}\right)^{1/2} \tag{1.11b}$$

Targeting reaction kinetics on surfaces, equation (1.3) together with (1.4a) already describes the change in the standard Gibbs free energy of a substrate (1.12) which is related to the chemical potentials of the ground and transition states as well as the potential of the empty surface.[101]

$$\Delta G^{0\ddagger} = \mu_{TS}^0 - \mu_{GS}^0 - \mu_*^0 \tag{1.12}$$

In general, the chemical potential is given as a sum of an ideal contribution and an excess contribution describing the thermodynamic non-ideality.[106] Consequently, we yield equations (3.1a-c) as

$$\mu_i = \mu_i^{ideal} + \mu_i^{excess} \tag{1.13a}$$

$$\mu_i^{ideal} = \mu_i^0 + RT\ln(x_i) = \mu_i^0 + RT\ln\left(\frac{\theta_i}{\theta_*}\right) \tag{1.13b}$$

$$\mu_i^{excess} = RT\ln(\gamma_i) \tag{1.13c}$$

for a constant temperature and pressure, where the excess chemical potential accounts for intermolecular interactions between the solute and solvent molecules.[107,108] Assuming a typical chemical reaction on the surface $A\ (g)\ + * \rightleftharpoons\ A*\ (surf)\ \overset{k}{\rightarrow}\ P$ with k being an irreversible rate limiting reaction step and adsorption being equilibrated, one applies transition state formalism to yield the relationship of the equilibrium constant for the reactants in the ground state converting to the activated complex (1.14)[101] and together with (1.4a) we get the expressions:

$$K^\ddagger = \exp\left(-\frac{\Delta G^{0\ddagger}}{RT}\right) = \exp\left(-\frac{\mu_\ddagger^0 - \mu_{A^*}^0}{RT}\right) \tag{1.14a}$$

$$r = \frac{k_B\ T}{h}\exp\left(-\frac{\mu_\ddagger^0 - \mu_{A^*}^0}{RT}\right) \cdot \frac{\gamma_{A^*}}{\gamma_\ddagger} \cdot c_{A^*} = k \cdot \theta_A \tag{1.14b}$$

were c_{A^*} is the concentration of A on the surface, which by definition the coverage $c_{A^*} \equiv \theta_A$.[108] Assuming the chemical potentials of the adsorbed ground state and the substrate A in solution are equal, one can write by applying Langmuir-type adsorption (site balance closed: $1 = \theta_A + \theta_*$) for the chemical potential of an ideal thermodynamic system$\left(\frac{\gamma_{A^*}}{\gamma_\ddagger} = 1\right)$[108]:

$$\mu_{A(l)} = \mu_{A^*} = \mu^0_{A^*} + \mathrm{RTln}\left(\frac{\theta_A}{1 - \theta_A}\right) \tag{1.15a}$$

$$\mu_{\ddagger^*} = \mu^0_{\ddagger^*} + \mathrm{RTln}\left(\frac{\theta_\ddagger}{1 - \theta_\ddagger}\right) \tag{1.15b}$$

$$\theta_A = \frac{\exp\left(-\frac{\mu_{A^*}}{RT}\right)}{1 - \exp\left(-\frac{\mu_{A^*}}{RT}\right) + \exp\left(-\frac{\mu^0_{A^*}}{RT}\right)} \tag{1.15c}$$

This means for a chemical reaction, following transition state theory as (1.1)

$$r = \frac{k_B\,T}{h}c^\ddagger = \frac{k_B T}{h}\frac{\exp\left(-\frac{\mu^0_\ddagger}{RT}\right)}{1 - \exp\left(-\frac{\mu_{A^*}}{RT}\right) + \exp\left(-\frac{\mu^0_{A^*}}{RT}\right)} \cdot \left(\frac{\gamma_{A^*}}{\gamma_\ddagger}\right) \tag{1.16}$$

that the rate only depends on $\mu^0_\ddagger, \mu^0_{A^*}$ and μ_{A^*} (Figure 1.10) for ideal system without excess contribution and for non-ideal system it additionally depends on γ_{A^*} and $\gamma_\ddagger$.

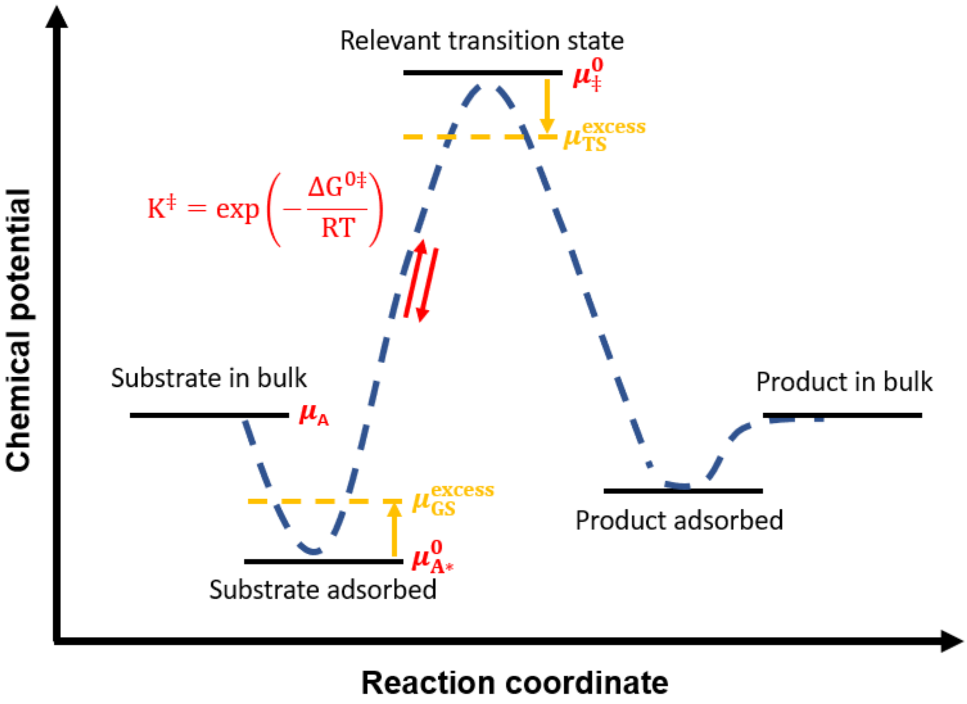

Figure 1.10 *Energy diagram of a typical catalyzed reaction with and without non-ideality contributions (based on Ref.* ^{109}*)*

One can differentiate three levels of influence: (i) The chemical environment, e.g., Al concentration in zeolites, impacts on the strength of BAS and LAS and thus, the nature of the center determines specific interactions; (ii) Steric constraints stabilize transition states or influences the self-organization of solvents and reactive substrates; or (iii) The self-organization of solvents and the presence of cation-anion pairs drastically change the standard chemical potential of reactive substrates.[109] This enables the possibility of catalyst finetuning and processes optimization to enhance ionic and electronic interactions between substrate and catalytic environment to increases acid catalyzed reaction rates.

1.5) Scope of the Thesis

The main goal of this thesis is to gain insights in acid catalyzed reactions such as cyclohexanol dehydrations, being a representative for biomass derived platform molecules, in aqueous and aprotic environment over heterogeneous catalysts. First deviations from ideality caused by ionic strength effects are analyzed and the concept of non-ideality is applied to zeolite catalysis. We investigate the combination of micropore volume and acid site density in the zeolite framework and correlate these physiochemical properties with the measured rates. The impact of the local ionic strength is analyzed on the chemical potential of ground- and transition state. The previously reported volcano-like shape of turnover frequencies (TOF) over Brønsted acid concentration (variation of Si/Al-ratio in H-MFI) is explained using the non-ideality concepts and hydronium ion – substrate distances in the pore channels. These explored concepts I aqueous phase are further applied to mesoporous mixed oxide catalysts. The effect of surface density evolution of tungsten-oxide domains on various supports on the catalytic activity is investigated. Using gas-phase water adsorption techniques a model for the electrical double layer surrounding the WO_x-domain is presented. The confinement effects investigated in the first section are applied to the constraint of the double layer and correlated with the catalytic activity of the various supported tungstates. Finally the apolar phase cyclohexanol dehydration in decalin is elucidated. Participating active sites are identified and quantified via in-situ titration appproach. The kinetics of Brønsted acid sites (BAS), as well as of Lewis acid sites are analyzed. It is shown that the previously for zeolites reported BAS-catalyzed monomer- and dimer-mediated pathway is also evident on tungstate zircona. Further the kinetics of the active Lewis acids are studied with kinetic isotope effect.

1.6) References

1 e.V., M. *Raffinerien und Pipelines*, <https://www.mwv.de/raffinerien-und-pipelines/> (

2 ENERGIE, B. F. W. U. *Rohöl: Transport, Lagerung und Verarbeitung* <https://www.bmwi.de/Redaktion/DE/Artikel/Energie/mineraloel-transport-lagerung-verarbeitung.html> (2021).

3 Baerns, M. *et al.* Technische Chemie. (2014).

4 Speight, J. G. *HANDBOOK OF PETROLEUM REFINING*. (CRC PRESS, 2020).

5 Speight, J. G. *The refinery of the future*. (2020).

6 Al-Gwaiz, M. M. & Murty, K. G. in *Case Studies in Operations Research: Applications of Optimal Decision Making* (ed Katta G. Murty) 217-296 (Springer New York, 2015).

7 Ertl, G. Handbook of heterogeneous catalysis. (2008).

8 Nelson, W. L. *Petroleum refinery engineering*. (McGraw-Hill, 1987).

9 Harding, R. H., Peters, A. W. & Nee, J. R. D. New developments in FCC catalyst technology. *Applied Catalysis A: General* **221**, 389-396, doi:https://doi.org/10.1016/S0926-860X(01)00814-6 (2001).

10 (BMWi), B. f. W. u. E. (2020).

11 Alhajri, I. (UWSpace, 2008).

12 Topsøe, H., Clausen, B. S. & Massoth, F. E. *Hydrotreating catalysis*. (Springer, 1996).

13 (IMO), I. M. O. *International Convention for the Prevention of Pollution from Ships (MARPOL)*, <https://www.imo.org/en/About/Conventions/Pages/International-Convention-for-the-Prevention-of-Pollution-from-Ships-(MARPOL).aspx> (2019).

14 Badawi, M., Vivier, L., Pérot, G. & Duprez, D. Promoting effect of cobalt and nickel on the activity of hydrotreating catalysts in hydrogenation and isomerization of olefins. *Journal of Molecular Catalysis A: Chemical* **293**, 53-58, doi:https://doi.org/10.1016/j.molcata.2008.07.006 (2008).

15 Andari, M. K., Bchbehani, H. & Stanislaus, A. SULFUR COMPOUND TYPE DISTRIBUTION IN NAPHTHA AND GAS OIL FRACTIONS OF KUWAITI CRUDE. *Fuel Science and Technology International* **14**, 939-961, doi:10.1080/08843759608947622 (1996).

16 La Vopa, V. & Satterfield, C. N. Poisoning of thiophene hydrodesulfurization by nitrogen compounds. *Journal of Catalysis* **110**, 375-387, doi:https://doi.org/10.1016/0021-9517(88)90328-4 (1988).

17 Houalla, M. *et al.* Hydrodesulfurization of methyl-substituted dibenzothiophenes catalyzed by sulfided Co・Moγ-Al2O3. *Journal of Catalysis* **61**, 523-527, doi:https://doi.org/10.1016/0021-9517(80)90400-5 (1980).

18 Schulz, H., Böhringer, W., Ousmanov, F. & Waller, P. Refractory sulfur compounds in gas oils. *Fuel Processing Technology* **61**, 5-41, doi:https://doi.org/10.1016/S0378-3820(99)00028-4 (1999).

19 Prins, R. *et al.* Mechanisms of hydrodesulfurization and hydrodenitrogenation. *Catalysis Today* **111**, 84-93, doi:https://doi.org/10.1016/j.cattod.2005.10.008 (2006).

20 Pazos, J. M. & Andréu, P. Hydrodesulphurization mechanism of thiophene and tetrahydrothiophene on a cobalt molybdenum catalyst. *Canadian Journal of Chemistry* **58**, 479-484, doi:10.1139/v80-077 (1980).

21 Yang, H., Fairbridge, C. & Ring, Z. Adsorption of Dibenzothiophene Derivatives over a MoS2 NanoclusterA Density Functional Theory Study of Structure−Reactivity Relations. *Energy & Fuels* **17**, 387-398, doi:10.1021/ef020171k (2003).

22 Yin, C.-l., Zhai, X.-p., Zhao, L.-y. & Liu, C.-g. Mechanism of Hydrodesulfurization of dibenzothiophenes on unsupported NiMoW catalyst. *Journal of Fuel Chemistry and Technology* **41**, 991-997, doi:https://doi.org/10.1016/S1872-5813(13)60043-2 (2013).

23 Wagenhofer, M. F., Shi, H., Gutiérrez, O. Y., Jentys, A. & Lercher, J. A. Enhancing hydrogenation activity of Ni-Mo sulfide hydrodesulfurization catalysts. *Science Advances* **6**, eaax5331, doi:10.1126/sciadv.aax5331 (2020).

24 Egorova, M. & Prins, R. Mutual influence of the HDS of dibenzothiophene and HDN of 2-methylpyridine. *Journal of Catalysis* **221**, 11-19, doi:https://doi.org/10.1016/S0021-9517(03)00264-1 (2004).

25 Oyama, S. T. & Lee, Y.-K. Mechanism of Hydrodenitrogenation on Phosphides and Sulfides. *The Journal of Physical Chemistry B* **109**, 2109-2119, doi:10.1021/jp049194l (2005).

26 Jian, M. & Prins, R. Mechanism of the Hydrodenitrogenation of Quinoline over NiMo(P)/Al2O3Catalysts. *Journal of Catalysis* **179**, 18-27, doi:https://doi.org/10.1006/jcat.1998.2181 (1998).

27 Dincer, I. & Acar, C. Review and evaluation of hydrogen production methods for better sustainability. *International Journal of Hydrogen Energy* **40**, 11094-11111, doi:https://doi.org/10.1016/j.ijhydene.2014.12.035 (2015).

28 Fulcheri, L. *et al.* Plasma processing: a step towards the production of new grades of carbon black. *Carbon* **40**, 169-176, doi:https://doi.org/10.1016/S0008-6223(01)00169-5 (2002).

29 Chi, J. & Yu, H. Water electrolysis based on renewable energy for hydrogen production. *Chinese Journal of Catalysis* **39**, 390-394, doi:https://doi.org/10.1016/S1872-2067(17)62949-8 (2018).

30 Aitani, A. M. Processes to enhance refinery-hydrogen production. *International Journal of Hydrogen Energy* **21**, 267-271, doi:https://doi.org/10.1016/0360-3199(95)00082-8 (1996).

31 van Dyk, S., Su, J., Mcmillan, J. D. & Saddler, J. Potential synergies of drop-in biofuel production with further co-processing at oil refineries. *Biofuels, Bioproducts and Biorefining* **13**, 760-775, doi:https://doi.org/10.1002/bbb.1974 (2019).

32 Sharma, T., Dasgupta, D., Singh, J., Bhaskar, T. & Ghosh, D. Yeast lipid-based biofuels and oleochemicals from lignocellulosic biomass: life cycle impact assessment. *Sustainable Energy & Fuels* **4**, 387-398, doi:10.1039/C9SE00540D (2020).

33 Chen, H. in *Lignocellulose Biorefinery Engineering* (ed Hongzhang Chen) 87-124 (Woodhead Publishing, 2015).

34 Stöcker, M. Biofuels and Biomass-To-Liquid Fuels in the Biorefinery: Catalytic Conversion of Lignocellulosic Biomass using Porous Materials. *Angewandte Chemie International Edition* **47**, 9200-9211, doi:https://doi.org/10.1002/anie.200801476 (2008).

35 Dabros, T. M. H. *et al.* Transportation fuels from biomass fast pyrolysis, catalytic hydrodeoxygenation, and catalytic fast hydropyrolysis. *Progress in Energy and Combustion Science* **68**, 268-309, doi:10.1016/j.pecs.2018.05.002 (2018).

36 Huber, G. W. & Corma, A. Synergies between Bio- and Oil Refineries for the Production of Fuels from Biomass. *Angewandte Chemie International Edition* **46**, 7184-7201, doi:https://doi.org/10.1002/anie.200604504 (2007).

37 Talmadge, M. S. *et al.* A perspective on oxygenated species in the refinery integration of pyrolysis oil. *Green Chemistry* **16**, 407-453, doi:10.1039/C3GC41951G (2014).

38 Yaman, E. *et al.* Catalytic upgrading of pyrolysis vapours: Effect of catalyst support and metal type on phenolic content of bio-oil. *Journal of Cleaner Production* **185**, 52-61, doi:https://doi.org/10.1016/j.jclepro.2018.03.033 (2018).

39 Pinho, A. d. R., de Almeida, M. B. B., Mendes, F. L., Ximenes, V. L. & Casavechia, L. C. Co-processing raw bio-oil and gasoil in an FCC Unit. *Fuel Processing Technology* **131**, 159-166, doi:https://doi.org/10.1016/j.fuproc.2014.11.008 (2015).

40 GmbH, N. G. *Die NEXBTL-Technologie ist unsere eigene Innovation*, <https://www.neste.de/ueber-neste/wer-wir-sind/forschung/nexbtl-technologie> (

41 Lestari , S., Mäki-Arvela, P., Beltramini, J., Lu, G. Q. M. & Murzin, D. Y. Transforming Triglycerides and Fatty Acids into Biofuels. *ChemSusChem* **2**, 1109-1119, doi:https://doi.org/10.1002/cssc.200900107 (2009).

42 Bezergianni, S., Dimitriadis, A., Sfetsas, T. & Kalogianni, A. Hydrotreating of waste cooking oil for biodiesel production. Part II: Effect of temperature on hydrocarbon composition. *Bioresource Technology* **101**, 7658-7660, doi:https://doi.org/10.1016/j.biortech.2010.04.043 (2010).

43 Lindfors, C., Kuoppala, E., Oasmaa, A., Solantausta, Y. & Arpiainen, V. Fractionation of Bio-Oil. *Energy & Fuels* **28**, 5785-5791, doi:10.1021/ef500754d (2014).

44 Das, A. & König, B. Transition metal- and photoredox-catalyzed valorisation of lignin subunits. *Green Chemistry* **20**, 4844-4852, doi:10.1039/C8GC02073F (2018).

45 Zhi, Y. *et al.* Dehydration Pathways of 1-Propanol on HZSM-5 in the Presence and Absence of Water. *Journal of the American Chemical Society* **137**, 15781-15794, doi:10.1021/jacs.5b09107 (2015).

46 Pandey, M. P. & Kim, C. S. Lignin Depolymerization and Conversion: A Review of Thermochemical Methods. *Chemical Engineering & Technology* **34**, 29-41, doi:https://doi.org/10.1002/ceat.201000270 (2011).

47 Zhang, J. *et al.* Highly efficient, NiAu-catalyzed hydrogenolysis of lignin into phenolic chemicals. *Green Chemistry* **16**, 2432-2437, doi:10.1039/C3GC42589D (2014).

48 Lavoie, J.-M., Baré, W. & Bilodeau, M. Depolymerization of steam-treated lignin for the production of green chemicals. *Bioresource Technology* **102**, 4917-4920, doi:https://doi.org/10.1016/j.biortech.2011.01.010 (2011).

49 Wahyudiono, Sasaki, M. & Goto, M. Recovery of phenolic compounds through the decomposition of lignin in near and supercritical water. *Chemical Engineering and Processing: Process Intensification* **47**, 1609-1619, doi:https://doi.org/10.1016/j.cep.2007.09.001 (2008).

50 Deepa, A. K. & Dhepe, P. L. Lignin Depolymerization into Aromatic Monomers over Solid Acid Catalysts. *ACS Catalysis* **5**, 365-379, doi:10.1021/cs501371q (2015).

51 Zakzeski, J., Jongerius, A. L., Bruijnincx, P. C. A. & Weckhuysen, B. M. Catalytic Lignin Valorization Process for the Production of Aromatic Chemicals and Hydrogen. *ChemSusChem* **5**, 1602-1609, doi:https://doi.org/10.1002/cssc.201100699 (2012).

52 Ouyang, X., Huang, X., Zhu, J., Boot, M. D. & Hensen, E. J. M. Catalytic Conversion of Lignin in Woody Biomass into Phenolic Monomers in Methanol/Water Mixtures without External Hydrogen. *ACS Sustainable Chemistry & Engineering* **7**, 13764-13773, doi:10.1021/acssuschemeng.9b01497 (2019).

53 Wendisch, V. F., Kim, Y. & Lee, J.-H. Chemicals from lignin: Recent depolymerization techniques and upgrading extended pathways. *Current Opinion in Green and Sustainable Chemistry* **14**, 33-39, doi:https://doi.org/10.1016/j.cogsc.2018.05.006 (2018).

54 Deepa, A. K. & Dhepe, P. L. Function of Metals and Supports on the Hydrodeoxygenation of Phenolic Compounds. *ChemPlusChem* **79**, 1573-1583, doi:https://doi.org/10.1002/cplu.201402145 (2014).

55 Wang, X., Arai, M., Wu, Q., Zhang, C. & Zhao, F. Hydrodeoxygenation of lignin-derived phenolics – a review on the active sites of supported metal catalysts. *Green Chemistry* **22**, 8140-8168, doi:10.1039/D0GC02610G (2020).

56 Scholze, B. & Meier, D. Characterization of the water-insoluble fraction from pyrolysis oil (pyrolytic lignin). Part I. PY–GC/MS, FTIR, and functional groups. *Journal of Analytical and Applied Pyrolysis* **60**, 41-54, doi:https://doi.org/10.1016/S0165-2370(00)00110-8 (2001).

57 Song, Q.-H., Nie, J.-Q., Ren, M.-G. & Guo, Q.-X. Effective Phase Separation of Biomass Pyrolysis Oils by Adding Aqueous Salt Solutions. *Energy & Fuels* **23**, 3307-3312, doi:10.1021/ef900143u (2009).

58 Zabelkin, S., Grachev, A., Fayzrakhmanova, G., Makarov, A. & Bashkirov, V. Application of the water-insoluble pyrolysis oil fraction as an organic binder. *Construction and Building Materials* **102**, 59-64, doi:https://doi.org/10.1016/j.conbuildmat.2015.10.164 (2016).

59 Zhao, C., He, J., Lemonidou, A. A., Li, X. & Lercher, J. A. Aqueous-phase hydrodeoxygenation of bio-derived phenols to cycloalkanes. *Journal of Catalysis* **280**, 8-16, doi:https://doi.org/10.1016/j.jcat.2011.02.001 (2011).

60 Hintermeier, P. H. *et al.* Hydronium-Ion-Catalyzed Elimination Pathways of Substituted Cyclohexanols in Zeolite H-ZSM5. *ACS Catalysis* **7**, 7822-7829, doi:10.1021/acscatal.7b01582 (2017).

61 Eckstein, S. *et al.* Influence of Hydronium Ions in Zeolites on Sorption. *Angewandte Chemie International Edition* **58**, 3450-3455, doi:10.1002/anie.201812184 (2019).

62 Milakovic, L. *et al.* Towards understanding and predicting the hydronium ion catalyzed dehydration of cyclic-primary, secondary and tertiary alcohols. *Journal of Catalysis* **390**, 237-243, doi:https://doi.org/10.1016/j.jcat.2020.08.009 (2020).

63 Liu, Y. *et al.* Enhancing the catalytic activity of hydronium ions through constrained environments. *Nature Communications* **8**, 14113, doi:10.1038/ncomms14113

https://www.nature.com/articles/ncomms14113#supplementary-information (2017).

64 Liu, Y. *et al.* Solvent-determined mechanistic pathways in zeolite-H-BEA-catalysed phenol alkylation. *Nature Catalysis* **1**, 141-147, doi:10.1038/s41929-017-0015-z (2018).

65 Shi, H., Eckstein, S., Vjunov, A., Camaioni, D. M. & Lercher, J. A. Tailoring nanoscopic confines to maximize catalytic activity of hydronium ions. *Nature Communications* **8**, 15442, doi:10.1038/ncomms15442

https://www.nature.com/articles/ncomms15442#supplementary-information (2017).

66 Hensley, A. J. R., Bray, J., Shangguan, J., Chin, Y.-H. & McEwen, J.-S. Catalytic consequences of hydrogen addition events and solvent-adsorbate interactions during guaiacol-H2 reactions at the H2O-Ru(0 0 0 1) interface. *Journal of Catalysis* **395**, 467-482, doi:https://doi.org/10.1016/j.jcat.2020.09.034 (2021).

67 Shangguan, J. & Chin, Y.-H. C. Kinetic Significance of Proton–Electron Transfer during Condensed Phase Reduction of Carbonyls on Transition Metal Clusters. *ACS Catalysis* **9**, 1763-1778, doi:10.1021/acscatal.8b03470 (2019).

68 Shangguan, J., Pfriem, N. & Chin, Y.-H. Mechanistic details of CO bond activation in and H-addition to guaiacol at water-Ru cluster interfaces. *Journal of Catalysis* **370**, 186-199, doi:https://doi.org/10.1016/j.jcat.2018.11.036 (2019).

69 Shangguan, J., Olarte, M. V. & Chin, Y.-H. Mechanistic insights on CO and CC bond activation and hydrogen insertion during acetic acid hydrogenation catalyzed by ruthenium clusters in aqueous medium. *Journal of Catalysis* **340**, 107-121, doi:https://doi.org/10.1016/j.jcat.2016.04.024 (2016).

70 Shangguan, J. *et al.* The Role of Protons and Hydrides in the Catalytic Hydrogenolysis of Guaiacol at the Ruthenium Nanoparticle–Water Interface. *ACS Catalysis* **10**, 12310-12332, doi:10.1021/acscatal.0c01963 (2020).

71 Román-Leshkov, Y. & Dumesic, J. A. Solvent Effects on Fructose Dehydration to 5-Hydroxymethylfurfural in Biphasic Systems Saturated with Inorganic Salts. *Topics in Catalysis* **52**, 297-303, doi:10.1007/s11244-008-9166-0 (2009).
72 Gardner, D. W. *et al.* Insights into the Hydrothermal Stability of ZSM-5 under Relevant Biomass Conversion Reaction Conditions. *ACS Catalysis* **5**, 4418-4422, doi:10.1021/acscatal.5b00888 (2015).
73 Bronsted, J. N. & Teeter, C. E. On Kinetic Salt Effect. *The Journal of Physical Chemistry* **28**, 579-587, doi:10.1021/j150240a003 (1924).
74 Debye, P. & Pauling, L. THE INTER-IONIC ATTRACTION THEORY OF IONIZED SOLUTES. IV. THE INFLUENCE OF VARIATION OF DIELECTRIC CONSTANT ON THE LIMITING LAW FOR SMALL CONCENTRATIONS. *Journal of the American Chemical Society* **47**, 2129-2134, doi:10.1021/ja01685a008 (1925).
75 Olson, A. R. & Simonson, T. R. Rates of Ionic Reactions in Aqueous Solutions. *The Journal of Chemical Physics* **17**, 1167-1173, doi:10.1063/1.1747137 (1949).
76 Perlmutter-Hayman, B. & Stein, G. The Kinetics of the Decomposition of Alkaline Solutions of Hypobromite—Specific Ionic Effects on Reaction Rate. *The Journal of Physical Chemistry* **63**, 734-738, doi:10.1021/j150575a022 (1959).
77 Perlmutter-Hayman, B. & Weissmann, Y. Kinetics of the hydrolysis of the dichromate ion. III. Environmental effects on rate constants and activation energies. *The Journal of Physical Chemistry* **71**, 1409-1415, doi:10.1021/j100864a035 (1967).
78 Perlmutter-Hayman, B. & Stein, G. Specific Ionic Effects on Reaction Rates. The Reaction between Persulfate and Iodide Ions in the Presence of High Concentrations of Added Salts. *The Journal of Chemical Physics* **40**, 848-852, doi:10.1063/1.1725215 (1964).
79 Agblevor, F. A. & Besler, S. Inorganic Compounds in Biomass Feedstocks. 1. Effect on the Quality of Fast Pyrolysis Oils. *Energy & Fuels* **10**, 293-298, doi:10.1021/ef950202u (1996).
80 Shaikh, A. A., Walter de Gruyter Gmb, H. & Co, K. G. Heterogeneous Catalysis Essentials for Chemical Engineers. (2020).
81 Sádaba, I., López Granados, M., Riisager, A. & Taarning, E. Deactivation of solid catalysts in liquid media: the case of leaching of active sites in biomass conversion reactions. *Green Chemistry* **17**, 4133-4145, doi:10.1039/C5GC00804B (2015).
82 Mallada, R. in *Encyclopedia of Membranes* (eds Enrico Drioli & Lidietta Giorno) 1-2 (Springer Berlin Heidelberg, 2015).
83 Weitkamp, J. Catalysis and Zeolites Fundamentals and Applications. (1999).
84 Yilmaz, B. & Müller, U. Catalytic Applications of Zeolites in Chemical Industry. *Topics in Catalysis* **52**, 888-895, doi:10.1007/s11244-009-9226-0 (2009).
85 Xin, Y., Li, Q. & Zhang, Z. Zeolitic Materials for DeNOx Selective Catalytic Reduction. *ChemCatChem* **10**, 29-41, doi:https://doi.org/10.1002/cctc.201700854 (2018).
86 Kulprathipanja, S. *Zeolites in Industrial Separation and Catalysis*. (John Wiley & Sons, 2010).
87 Schulman, E., Wu, W. & Liu, D. Two-Dimensional Zeolite Materials: Structural and Acidity Properties. *Materials* **13**, doi:10.3390/ma13081822 (2020).
88 Li, G. & Pidko, E. A. The Nature and Catalytic Function of Cation Sites in Zeolites: a Computational Perspective. *ChemCatChem* **11**, 134-156, doi:https://doi.org/10.1002/cctc.201801493 (2019).
89 Gorte, R. J. What do we know about the acidity of solid acids? *Catalysis Letters* **62**, 1-13, doi:10.1023/A:1019010013989 (1999).
90 Moliner, M. State of the art of Lewis acid-containing zeolites: lessons from fine chemistry to new biomass transformation processes. *Dalton Transactions* **43**, 4197-4208, doi:10.1039/C3DT52293H (2014).

91 Prodinger, S. *et al.* Stability of Zeolites in Aqueous Phase Reactions. *Chemistry of Materials* **29**, 7255-7262, doi:10.1021/acs.chemmater.7b01847 (2017).

92 Wang, M. *et al.* Genesis and Stability of Hydronium Ions in Zeolite Channels. *Journal of the American Chemical Society* **141**, 3444-3455, doi:10.1021/jacs.8b07969 (2019).

93 Xiong, H., Pham, H. N. & Datye, A. K. Hydrothermally stable heterogeneous catalysts for conversion of biorenewables. *Green Chemistry* **16**, 4627-4643, doi:10.1039/C4GC01152J (2014).

94 Baertsch, C. D., Komala, K. T., Chua, Y.-H. & Iglesia, E. Genesis of Brønsted Acid Sites during Dehydration of 2-Butanol on Tungsten Oxide Catalysts. *Journal of Catalysis* **205**, 44-57, doi:https://doi.org/10.1006/jcat.2001.3426 (2002).

95 Barton, D. G., Soled, S. L. & Iglesia, E. Solid acid catalysts based on supported tungsten oxides. *Topics in Catalysis* **6**, 87-99, doi:10.1023/A:1019126708945 (1998).

96 Macht, J. & Iglesia, E. Structure and function of oxide nanostructures: catalytic consequences of size and composition. *Physical Chemistry Chemical Physics* **10**, 5331-5343, doi:10.1039/B805251D (2008).

97 Macht, J. *et al.* Support effects on Brønsted acid site densities and alcohol dehydration turnover rates on tungsten oxide domains. *Journal of Catalysis* **227**, 479-491, doi:https://doi.org/10.1016/j.jcat.2004.08.014 (2004).

98 Barton, D. G., Shtein, M., Wilson, R. D., Soled, S. L. & Iglesia, E. Structure and Electronic Properties of Solid Acids Based on Tungsten Oxide Nanostructures. *The Journal of Physical Chemistry B* **103**, 630-640, doi:10.1021/jp983555d (1999).

99 Chemistry, J. L. P. *Derivation of the Brønsted-Bjerrum Equation for the Effectof Added Salt on Rate Constants in Ionic Reactions*, <https://jameslab.ucsf.edu/PC_111/JOHN/Chem.%20112%20pdf%20files/Chem%20112%20Suppl.%20Files/Chem112KineticSaltEff.pdf> (

100 Brenner, H. M. B. Kinetics of Chemical Processes. (2014).

101 Madon, R. J. & Iglesia, E. Catalytic reaction rates in thermodynamically non-ideal systems. *Journal of Molecular Catalysis A: Chemical* **163**, 189-204, doi:https://doi.org/10.1016/S1381-1169(00)00386-1 (2000).

102 Moelwyn-Hughes, E. A. *The chemical statics and kinetics of solutions [by] E. A. Moelwyn Hughes*. (Academic Press Inc., 1971).

103 Hückel, E. in *Ergebnisse der exakten naturwissenschaften* 199-276 (Springer Berlin Heidelberg, 1924).

104 Logan, S. R. Effects of ionic strength on the rates of reaction between ions in solution. *Transactions of the Faraday Society* **63**, 3004-3008, doi:10.1039/TF9676303004 (1967).

105 Kontogeorgis, G. M., Maribo-Mogensen, B. & Thomsen, K. The Debye-Hückel theory and its importance in modeling electrolyte solutions. *Fluid Phase Equilibria* **462**, 130-152, doi:https://doi.org/10.1016/j.fluid.2018.01.004 (2018).

106 Frenkel, D. & Smit, B. *Understanding molecular simulation from algorithms to applications*. (Academic Press, 2002).

107 Paliwal, A., Asthagiri, D., Pratt, L. R., Ashbaugh, H. S. & Paulaitis, M. E. An analysis of molecular packing and chemical association in liquid water using quasichemical theory. *The Journal of Chemical Physics* **124**, 224502, doi:10.1063/1.2202350 (2006).

108 Cheng, J. & Hu, P. Theory of the kinetics of chemical potentials in heterogeneous catalysis. *Angew Chem Int Ed Engl* **50**, 7650-7654, doi:10.1002/anie.201101459 (2011).

109 Johannes, L. *Fundamentals of Catalysis* (Technische Universität München Department Chemie, 2021).

2) Role of the ionic environment to enhance activity of reacting molecules in zeolite pores

Niklas Pfriem[1], Peter H. Hintermeier[1], Sebastian Eckstein[1], Sungmin Kim[2], Qiang Liu[1], Hui Shi[1], Lara Milakovic[1], Yuanshuai Liu[1], Gary L. Haller[1], Eszter Baráth[1], Yue Liu[1]*, Johannes A. Lercher[1,2]*

[1]Department of Chemistry and Catalysis Research Center, Technical University of Munich, Lichtenbergstrasse 4, 85747 Garching, Germany.

[2]Institute for Integrated Catalysis, Pacific Northwest National Laboratory, P.O. Box 999, Richland, WA 99352, United States.

Authors contributions: Y.L. and J.A.L. conceived the research; N.P. did the catalytic reaction by HCl and determined the activation energy on H-MFI; P.H.H., S.H., L.M., Yuanshuai L. and E.B. measured the physicochemical property and catalytic activity of H-MFI, wherein P.H.H. first reported the volcano-like activity of H-MFI; S.E. and Q.L. measured the adsorption property of H-MFI; S.K. measured the reaction on H-BEA; G.L.H. helped analyzing the data

This work has been published:
https://www.science.org/doi/abs/10.1126/science.abh3418

2.1) Abstract

Tailoring the molecular environment around catalytically active site allows to enhance catalytic reactivity via a hitherto unexplored pathway. In zeolites, the presence of water creates an ionic environment via formation of hydrated hydronium ions and the negatively charged framework Al tetrahedra. The high density of cation-anion pairs determined by the aluminum concentration of a zeolite induces a high local ionic strength that increases the excess chemical potential of sorbed and uncharged organic reactants. Charged transition states (carbocations for example) are stabilized, reducing the energy barrier and leading to higher reaction rates. Using the intramolecular dehydration of cyclohexanol on H-MFI in water, we show quantitatively the enhancement of the reaction rate by the presence of high ionic strength as well as potential limitations of this strategy.

2.2) Main text

Zeolites, Brønsted- or Lewis-acidic microporous tectosilicates, are widely applied in chemical industry for sorption, separation, and catalysis.[1-4] In the most classic case, the acid character is introduced by substitution of metal cations with a 3+ formal charge.[5] It has been speculated that the proximity of charge and dipoles in zeolite pores should give rise to strong field-effects, but the effects were not systematically quantifiable.[6,7] A long series of investigations has shown that Brønsted acid sites (BAS) have constant acid strength for sorption and catalysis, as long as the concentrations of substituting tetrahedral atoms did not exceed a certain threshold.[8,9] The high intrinsic catalytic activity of zeolites has, therefore, been attributed to the remarkable stabilization of transition states in the constraints of pores.[10-14]

Recent experiments showed that this beneficial aspect of transition state stabilization also holds true, when the catalyzed reaction is performed in the presence of water, allowing for the generation of hydrated hydronium ions [$H_3O^+_{hydr.}$]. The catalytic activity of these hydronium ions is up to two orders of magnitude higher than the respective specific activity of hydrated hydronium ions in an aqueous acid solution as probed by alcohol dehydration.[10,11,15] In the environment of the zeolites, the hydrated hydronium ions occupy a well-defined location at aluminum tetrahedra (that causes the BAS in the solid), are located in much closer proximity in zeolite pores than in the liquid phase. This proximity has been shown to lead to an increase in the activity coefficient of organic molecules in the zeolite pores, resembling the situation in aqueous phase in the presence of high concentrations of cations and anions of dissolved acids, bases, and salts.[15] The direct consequence of the higher activity coefficient is a decrease of the interaction strength of the sorbed organic molecules, much like the decreasing interaction with the solvent in an aqueous solution of increasing density of cation – anion pairs. This allows to rigorously translate the physical chemistry of non-ideality in an aqueous phase into the constraints of nanopores.

The higher activity coefficient is caused by an increase in the excess chemical potential compared to an ideal environment, for example, of a zeolite having no BAS. Conceptually, the increase in the excess chemical potential of the reacting molecule decreases the energy difference to the transition state and, in consequence, should lead to a higher rate, even if the transition state is not stabilized. In addition to that, a polar transition state will be stabilized by the polar environment compared to the uncharged reactant. It should be noted in passing that the confinement and the well-defined close spacing of hydrated hydronium ions additionally stabilizes the transition state, acting positively to reduce the free energy barrier in the confines of zeolites.[10,11]

We show in this contribution that such a scenario can be realized and that the combination of the increase in the thermodynamic activity of reacting molecules and the steric constraints of the zeolite pores leads to strong deviations from the expected sympathetic variation of catalytic activities with active sites of constant acid-base properties. We use the dehydration of cyclohexanol on a series of H-MFI zeolites with a wide range of BAS [$H_3O^+_{hydr.}$] (0.05 – 0.86 mmol/g_{MFI}) to show that the positive effect of enhancing the excess chemical potential of reacting molecules leads to an optimum density of active sites.

Catalyzed by hydrated hydronium ions ($H_3O^+_{hydr.}$), cyclohexanol dehydrates to cyclohexene in the aqueous phase on zeolite H-MFI. The reaction rate is independent of the aqueous phase concentration of cyclohexanol above 0.1 mol/L (zero order reaction region, S-Figure 2.1). The rate normalized to the concentration of BAS, the turnover frequency (TOF), increased 6-fold from BAS concentration of 0.054 to 0.36 mmol/g_{MFI} and then decreased by 60% to BAS concentration of 0.86 mmol/g_{MFI} (S-Figure 2.1A). Concurrently, the activation energy decreased from 161 kJ/mol to 140 kJ/mol and increased to 158 kJ/mol afterwards (S-Figure 2.B). In contrast, for gas phase reactions such as *n*-pentane cracking and 1-propanol dehydration, the variation in BAS concentration did not change the TOF, i.e., the acid strength of the sites involved can be considered as being constant (S-Figure 2.C). The identical catalytic activity of BAS in such a series of zeolites has been shown before for cracking.[16,17] It should be noted in passing that also the characterization with a base molecule showed an identical strength of the BAS.[18] Although it has been reported that different Al locations influence catalytic activity of zeolites,[19,20] the constant TOFs of *n*-pentane cracking and 1-propanol dehydration on all the tested H-MFIs allows to exclude the probability of selective Al locations on any specific T sites or in pairs impacting reactivity.

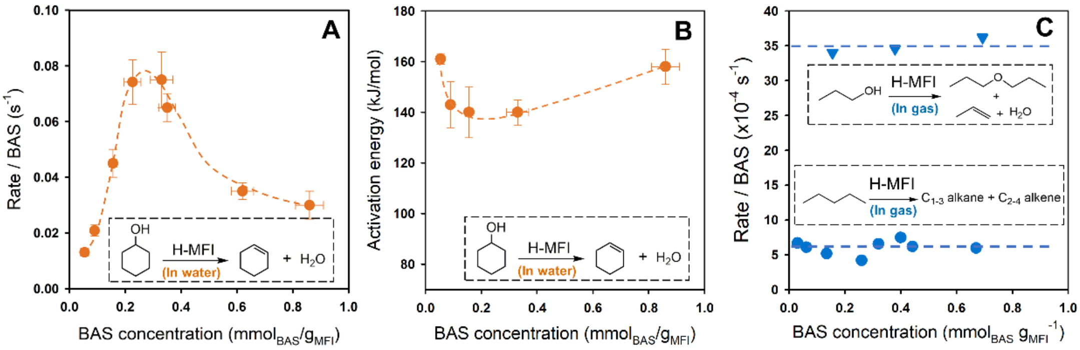

***Figure 2.1** Brønsted acid site (BAS) normalized reaction rate in H-MFI catalyzed reactions in water and gas phase. (A) Rate at 423 K and (B) activation energy of cyclohexanol dehydration on H-MFI with different BAS concentrations in water. (C) Cracking of n-pentane at 763 K (●) and dehydration of 1-propanol at 433 K (▼) on H-MFI with different BAS concentrations in the gas phase. Data for n-pentane cracking is from reference [21] and [16]; data for 1-propanol dehydration on H-MFI with 0.69 mmol/g_{MFI} is from reference [22].*

Then, the question arises as to why BAS exhibited significant differences in the presence of water. To address this question, we analyze the differences of BAS induced by their environments. In the gas phase, BAS are predominately covalent hydroxy groups, located on oxygen bridging between silicon-oxygen and aluminum-oxygen tetrahedra in the zeolite. The hydroxy groups are moderately polar and have negligible volume. In water the BAS are converted to hydrated hydronium ions ($H_3O^+_{hydr.}$) bonded ionically to the zeolite framework, with a positive charge and a specific volume.

In contrast to homogenous solution in which $H_3O^+_{hydr.}$ are highly dispersed throughout the liquid volume, the $H_3O^+_{hydr.}$ in H-MFI are confined in the limited space of zeolite pores. Consequently, this leads to a very high local concentration that cannot be changed by adding more water. Figure 2.1A (black) shows the concentrations of $H_3O^+_{hydr.}$ per H-MFI unit cell varying between 0.3 – 5 in the samples tested, corresponding to a local density of 0.1 – 1.6 mol/L, using the H-MFI unit cell volume of approximately 5.2 nm^3.[23] If we consider further that the micropore volume of H-MFI is only ~ 1.3 nm^3 per unit cell (~ 0.14 $cm^3/g_{MFI,}$ Table S1), the $H_3O^+_{hydr.}$ has a molarity in the range of 0.4 – 6.4 mol/L in the micropore space. Such high local concentrations of $H_3O^+_{hydr.}$ have two consequences, i.e., a very high local ionic strength and a competition between the $H_3O^+_{hydr.}$ and the substrate for the micropore space.

As an ion pair, $H_3O^+_{hydr.}$ with the corresponding anions, induces an ionic environment. In an aqueous homogenous electrolyte solution, this leads to non-ideality by which the ions (including $H_3O^+_{hydr.}$) have concentration-dependent activity coefficients (γ). A solute is stabilized ($\gamma < 1$) or destabilized ($\gamma > 1$) by the presence of a specific concentration of cations and anions, reflecting an increased or decreased excess chemical potential of the solute. The ionic strength (*I*), is the most critical variable determining the extent of deviation from an ideal solution. It is defined as the sum of all product charge (z_i) square weighted concentration (c_i) of all the ions (Equation 1). Thus, γ is expressed as a function of *I*, $\gamma(I)$.

$$\mathrm{I} = \frac{1}{2}\sum_{\mathrm{i}} \mathrm{c_i} \cdot \mathrm{z_i^2} \tag{2.1}$$

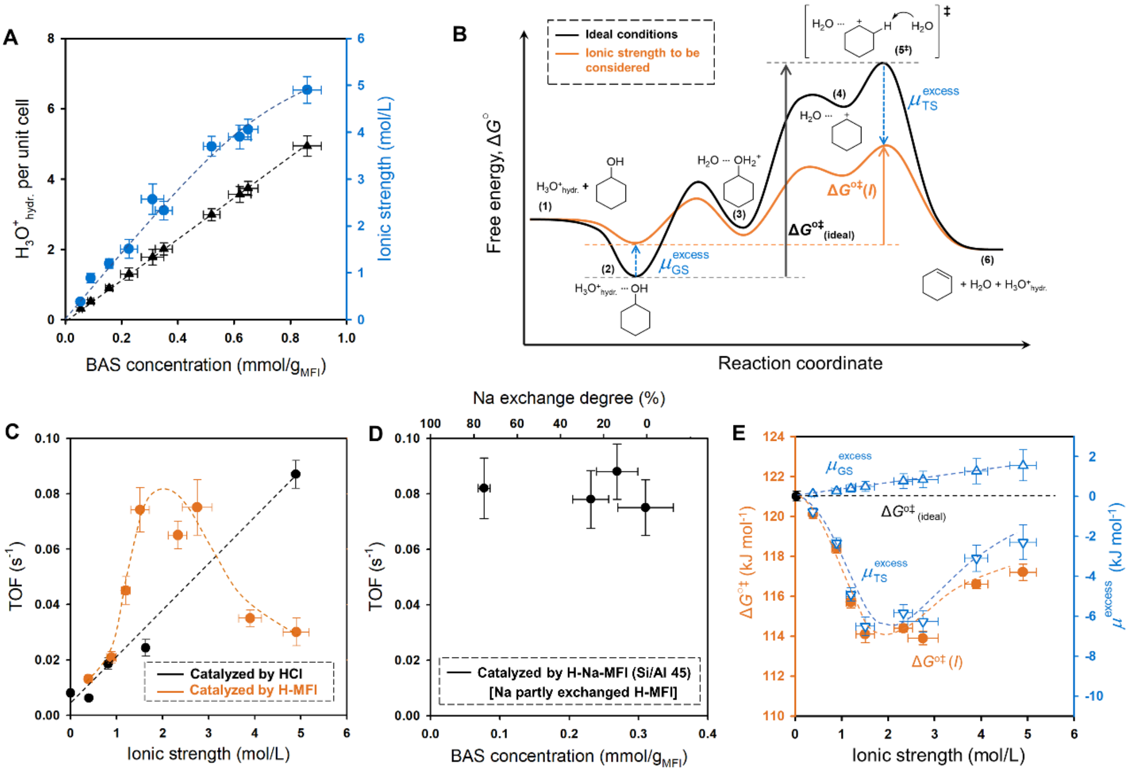

***Figure 2.2** Impact of local $H_3O^+_{hydr.}$ concentration and ionic strength on the dehydration of cyclohexanol catalyzed by $H_3O^+_{hydr.}$. (A) Unit cell normalized concentrations of $H_3O^+_{hydr.}$ (▲) and ionic strength (●) as a function of BAS ($H_3O^+_{hydr.}$) concentration. (B) Elementary steps and their energies in dehydration of cyclohexanol on $H_3O^+_{hydr.}$ in H-MFI zeolite in water under ideal and non-ideal conditions. (1) reactant cyclohexanol and $H_3O^+_{hydr.}$; (2) cyclohexanol associated with $H_3O^+_{hydr.}$; (3) protonated cyclohexanol; (4) cyclohexyl carbenium ion; (5‡) transition state of deprotonation of cyclohexyl carbenium ion by water; (6) product cyclohexene, water and $H_3O^+_{hydr.}$. The "H_2O···" represents the interactions with solvent water. (C) TOF as a function of ionic strength under the catalysis of HCl (●) at 453 K and H-MFI (●) at 423 K. The ionic strength in HCl solution is varied by the changing the concentration of LiCl electrolyte. (D) TOF of Na partly exchanged H-MFI (Si/Al 45). (E) Reaction free energy barriers and excess chemical potential of ground (GS) and transition state (TS) under the ideal condition and under an ionic strength. The calculation of free energy barriers and excess chemical potential are in Supplementary Text S2.1.*

Although classical ionic strength is defined for homogeneous solution, we have shown previously that the concept of non-ideality and ionic strength is transferrable to zeolites in water and applicable to quantitatively explain adsorption properties.[15] By considering the zeolite to be a "quasi solid electrolyte", its local ionic strength in a micropore is also defined by Equation 2.1, with z_i being 1 and c_i being volumetric densities of $H_3O^+_{hydr.}$ and negatively charged framework site (Z^-) in the micropores, i.e., concentration normalized to micropore volume. Figure 2.2A (blue) shows the ionic strength of the investigated H-MFI. Their high local concentration of $H_3O^+_{hydr.}$ in H-MFI micropores induces high local ionic strength. For example, H-MFI (Si/Al 15) has a BAS concentration of 0.86 ± 0.05 mol/g_{MFI}, corresponding to an ionic strength of 4.9 ± 0.3 mol/L. The ionic strength increases monotonically with the BAS concentration (Figure 2.2A), and the curve bends at high BAS concentration, because of the expansion of unit cell at high Al concentration that dilute the volumetric concentration of $H_3O^+_{hydr.}$.

The non-ideality also impacts the catalytic reaction rate. In general, the TOF under a certain ionic strength TOF(I) differs from that under ideal conditions $\mathrm{TOF}_{(ideal)}$, i.e., TOF at zero ionic strength, by factors of the activity coefficient of ground state $\gamma_{GS}(I)$ and transition state $\gamma_{TS}(I)$ (Eq. 2.2a, detailed derivations are in Text S2.1 and S2.2). The $\mathrm{TOF}_{(ideal)}$ is determined by $\Delta G^{o\ddagger}{}_{(ideal)}$, the free energy barrier under the ideal condition applying the transition state formula (Eq. 2.2b).

$$\mathrm{TOF(I)} = \mathrm{TOF_{(ideal)}} \cdot \frac{\gamma_{GS}(I)}{\gamma_{TS}(I)} \tag{2.2a}$$

$$\mathrm{TOF_{(ideal)}} =\cdot \frac{k_B T}{\mathrm{h}} \exp\left(-\frac{\Delta G^{\circ\ddagger}_{(ideal)}}{RT}\right) \tag{2.2b}$$

The k_B, h, and R denote the Boltzmann constant, Plank constant and ideal gas constant, respectively. The activity coefficient determines the excess chemical potential (μ^{excess}) according to $\mu^{\text{excess}} = RT\ln\gamma$. For the dehydration of cyclohexanol by $H_3O^+_{hydr.}$, it proceeds stepwise via association with $H_3O^+_{hydr.}$, protonation of the OH group, C-O cleavage to form the cyclohexyl carbenium ion and deprotonation of the cyclohexyl carbenium ion (Figure 2.2B). This stepwise mechanism is shown to dominate from low $H_3O^+_{hydr.}$ concentration (< 0.01 mol/L) in homogeneous acids to high local $H_3O^+_{hydr.}$ concentration (~ 2.7 mol/L) in zeolite.[10,11] The free energy barrier is the energy difference between transition state, the deprotonation of cyclohexyl carbenium ion by water ($C_6H_{11}^+ \cdots H_2O$), and the ground state of adsorbed cyclohexanol associated with $H_3O^+_{hydr.}$

($H_3O^+_{hydr.} \cdots C_6H_{11}OH$). Cyclohexanol is a neutral molecule in the ground state, while it is a positively charged cyclohexyl carbenium ion ($C_6H_{11}^+$) in the transition state. A neutral molecule is normally destabilized by the specific ionic strength ($\mu_{\mathrm{GS}}^{\mathrm{excess}} > 0$), which is given by Equation 2.3a showing a proportional increase with I. The term K_s denotes the Setschenow constant. In contrast, a cation or an anion is normally stabilized by the presence of an ionic environment ($\mu_{\mathrm{TS}}^{\mathrm{excess}} < 0$), given by extended Debye-Hückel Equation (e.g., Truesdell-Jones Equation, Eq. 2.3b) where a is the ion diameter, A, B and b are constants.

$$\mu_{\mathrm{GS}}^{\mathrm{excess}} = 2.303 \cdot \mathrm{RT}K_s \tag{2.3a}$$

$$\mu_{\mathrm{TS}}^{\mathrm{excess}} = 2.303 \cdot \mathrm{RT} \cdot \left(-\frac{A\sqrt{\mathrm{I}}}{1 + \mathrm{aB}\sqrt{\mathrm{I}}} + bI \right) \tag{2.3b}$$

As illustrated in Figure 2.2B, the positive $\mu_{\mathrm{GS}}^{\mathrm{excess}}$ and negative $\mu_{\mathrm{TS}}^{\mathrm{excess}}$ in an ionic environment lead to a lower energy barrier compared to that under ideal conditions ($\Delta G^{o\ddagger}(I) < \Delta G^{o\ddagger}_{\mathrm{(ideal)}}$).

The rate of cyclohexanol dehydration by HCl in homogeneous aqueous solution showed a positive correlation with the ionic strength in concentrated LiCl solution (Figure 2.2C, black line). Its TOF at 453 K is less than 0.01 s^{-1} at very low ionic strength, while it increased to more than 0.08 s^{-1} at high ionic strength of ~5 mol/L. In analogy to HCl, the TOF of cyclohexanol dehydration on H-MFI is replotted as a function of ionic strength (Figure 2.2C, orange line). It increases with increasing ionic strength up to ~2 mol/L, however, in contrast to HCl it drops at higher ionic strength.

To further explore the impact of ionic strength, a series of Na^+ partly exchanged H-MFI (Si/Al 45) were prepared. Partly exchanging $H_3O^+_{hydr.}$ by Na^+ decreases the BAS concentration of H-MFI while maintaining the same ionic strength. As shown in Figure 2.2D, with Na exchange degrees up to 75%, the TOFs of H-Na-MFI remained unchanged, indicating that the variation of the concentration of hydrated hydronium ions while maintaining the ionic strength constant does not change the reaction rate. The comparison of H-Na-MFI (Si/Al 45) with a Na^+ exchange degree of 75% with H-MFI (Si/Al 200) exemplifies the impact the ionic strength. Both samples have identical BAS concentration (77 vs. 90 µmol/g_{MFI}), however, the former has a higher ionic strength than the latter (2.6 vs. 0.9 mol/L) and, indeed, the TOF is fourfold higher on H-Na-MFI (Si/Al 45) than on H-MFI (Si/Al 200), i.e., 0.082 vs. 0.021 s^{-1}. Thus, these results demonstrate that it is not the location of hydronium ions or the hydronium ion concentrations, but the ionic strength that is critical for the specific catalyzed rate.

The free energy barrier and excess chemical potential in the reactions are shown in Figure 2.2E. The decrease of $\mu_{\mathrm{TS}}^{\mathrm{excess}}$ is more significant than the increase of $\mu_{\mathrm{GS}}^{\mathrm{excess}}$, thus, the lower free energy barrier is caused in its majority by the stabilization of transition state. The inverse-volcano trend of $\mu_{\mathrm{TS}}^{\mathrm{excess}}$ with ionic strength seems at first sight consistent with Equation 3b that the negative first term dominates at low ionic strength, while the positive second term dominates at high ionic strength. However, the monotonic increase of TOFs with ionic strength at all concentrations under HCl catalysis exclude this possibility.

Next, we explore the reason for the rate drop with $H_3O^+_{\mathrm{hydr.}}$ at higher concentrations. In variance to catalysis in aqueous HCl, in H-MFI both cyclohexanol and $H_3O^+_{\mathrm{hydr.}}$ reside in the zeolitic micropore channels, and their relative locations are depicted in Figure 2.3A. The average distance between two $H_3O^+_{\mathrm{hydr.}}$ neighbors ($d_{\mathrm{h\text{-}h}}$) represents the distance between $H_3O^+_{\mathrm{hydr.}}$-Z^- pairs. The distance between their boundaries is $d_{\mathrm{b\text{-}b}}$, with volume of $V_{\mathrm{b\text{-}b}}$. In this space between them resides the sorbed cyclohexanol. At molecular level, the change of electrolyte concentration is equivalent to the change of $d_{\mathrm{h\text{-}h}}$ and $d_{\mathrm{b\text{-}b}}$. Thus, the increase of BAS concentration in H-MFI leads to a shorter distance between $H_3O^+_{\mathrm{hydr.}}$, inducing a decrease of $d_{\mathrm{h\text{-}h}}$, $d_{\mathrm{b\text{-}b}}$ and $V_{\mathrm{b\text{-}b}}$. Figure 2.3B shows that increasing BAS concentration from 0.05 to 0.86 mmol/g_{MFI} reduced the $d_{\mathrm{h\text{-}h}}$ from 2.6 to 1.0 nm and the $d_{\mathrm{b\text{-}b}}$ from 1.6 to almost 0.0 nm. It should be noted here that the composition of $H_3O^+_{\mathrm{hydr.}}$ ($H^+(H_2O)_8$) was determined to be invariant with temperature (Text S2.3).

The individual energy level of reaction ground and transition states in terms of enthalpy ($\Delta H^{\circ}_{\mathrm{GS}}$, $\Delta H^{\circ}_{\mathrm{TS}}$) and excess chemical potential ($\mu_{\mathrm{GS}}^{\mathrm{excess}}$, $\mu_{\mathrm{TS}}^{\mathrm{excess}}$) on all studied H-MFI are depicted as a function of $d_{\mathrm{b\text{-}b}}$ (Figure 2.3C and 3D). The enthalpy of ground state $\Delta H^{\circ}_{\mathrm{GS}}$ of sorbed cyclohexanol is stable at a distance $d_{\mathrm{b\text{-}b}}$ larger than 0.8 nm, while it increases sharply with the decrease of $d_{\mathrm{b\text{-}b}}$ suggesting a repulsion between $H_3O^+_{\mathrm{hydr.}}$ and sorbed cyclohexanol. The same trend is observed for $\mu_{\mathrm{GS}}^{\mathrm{excess}}$. In contrast, the transition state has both $\Delta H^{\circ}_{\mathrm{TS}}$ and $\mu_{\mathrm{TS}}^{\mathrm{excess}}$ in reverse-volcano curves with the minimum at ~0.8 nm and ~0.6 nm of $d_{\mathrm{b\text{-}b}}$. The $d_{\mathrm{b\text{-}b}}$ of 0.8 nm is a critical distance at which $V_{\mathrm{b\text{-}b}}$ is 0.2 nm^3, the same volume of one cyclohexanol molecule in liquid phase. At this distance the volume between two neighboring $H_3O^+_{\mathrm{hydr.}}$ is equal to the van der Waal (vdW) volume of cyclohexanol. At lower $d_{\mathrm{b\text{-}b}}$, the $V_{\mathrm{b\text{-}b}}$ becomes smaller than vdW volume of cyclohexanol, causing a strong vdW repulsion that increases the energy of the TS and decrease the

TOF. In an open aqueous solution, the work to separate charges (hydronium ions and the anions of the zeolite) will be replaced only by a volume increase without constraining the sorbed alcohol.

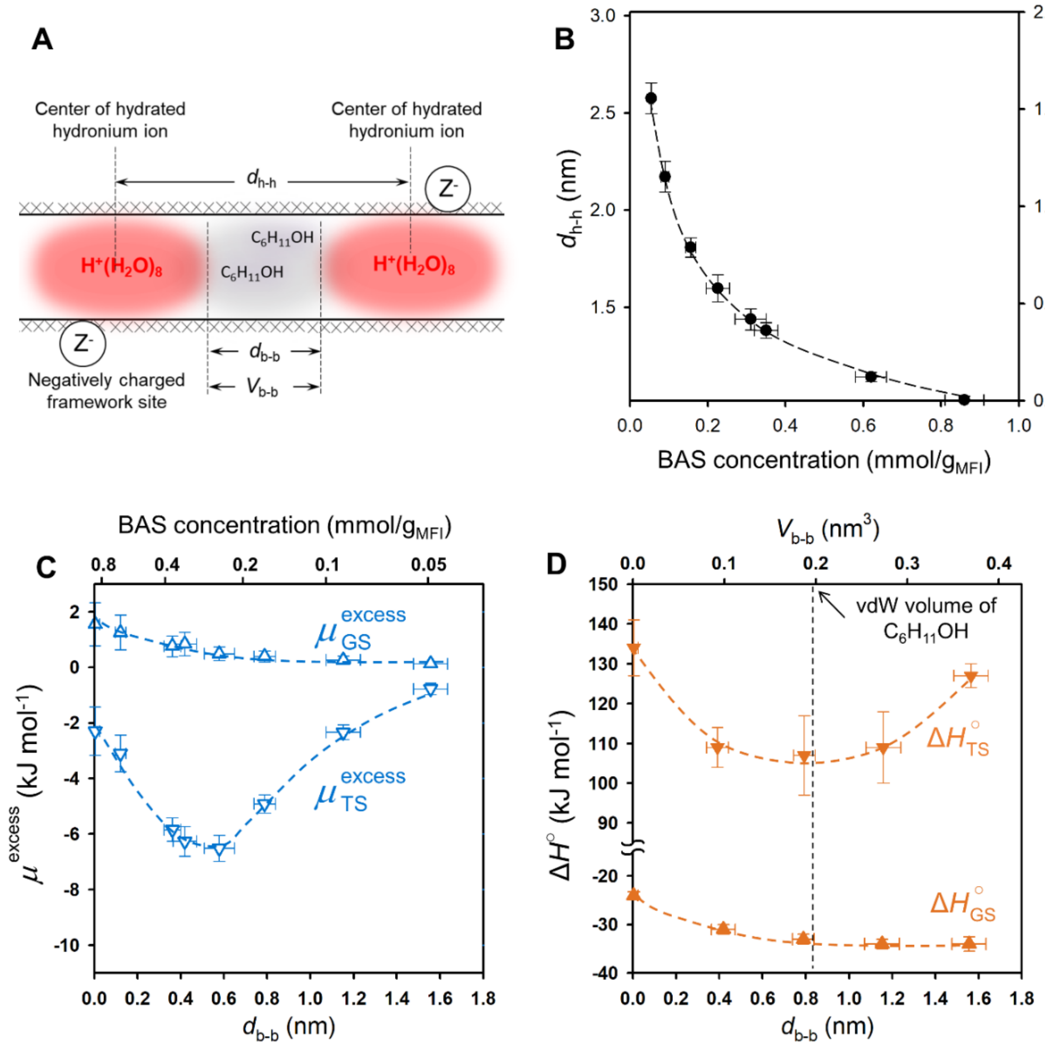

Figure 2.3 *Impact of the distance between $H_3O^+_{hydr.}$ in H-MFI micropore on the energy of the ground state (GS) and the transition state (TS) of cyclohexanol dehydration catalyzed by $H_3O^+_{hydr.}$. (A) Schematic illustration of $H_3O^+_{hydr.}$ and cyclohexanol in H-MFI micropore channels and the mean distance $d_{h\text{-}h}$ between two neighboring $H_3O^+_{hydr.}$, the mean distance $d_{b\text{-}b}$ and volume $V_{b\text{-}b}$ between the boundaries of neighboring $H_3O^+_{hydr.}$. (B) The $d_{h\text{-}h}$ and $d_{b\text{-}b}$ as a function of BAS concentration. (C) Excess chemical potential and (D) enthalpy of ground and transition state as a function of $d_{b\text{-}b}$ and $V_{b\text{-}b}$. The $d_{h\text{-}h}$ is estimated by the cubic root of the average zeolite volume normalized to the number of $H_3O^+_{hydr.}$; the $d_{b\text{-}b}$ is calculated by subtracting the length of $H_3O^+_{hydr.}$ from $d_{h\text{-}h}$; the $V_{b\text{-}b}$ is calculated by a cylinder model with length of $d_{b\text{-}b}$ and the diameter of H-MFI micropore channel.*

Thus, we show how the bulkiness and the charges of $H_3O^+_{hydr.}$ constrained in zeolite micropores combine to influence the catalytic activity. For H-MFI, the $H_3O^+_{hydr.}$ is a cluster with a composition of $H^+(H_2O)_8$ and has a specific volume, e.g. ~0.24 nm^3 at room temperature. It is anchored to the exchange sites of the zeolite framework by Coulombic forces and competes with substrate (e.g., cyclohexanol) to occupy the micropore volume. As the stabilization of water in the $H^+(H_2O)_8$ ion is larger than the stabilization of the sorbed organic molecule, i.e., cyclohexanol, the latter adsorbs only in the volume between neighboring $H^+(H_2O)_8$ in the micropore channel. This adds spatial constraints to substrate additional to that of micropore framework. At high $H_3O^+_{hydr.}$ concentrations, the volume between neighboring $H^+(H_2O)_8$ becomes smaller than vdW volume of substrate. This leads to strong vdW repulsion between substrate and $H^+(H_2O)_8$, and results in consequence in a decrease of the reaction rate. It should be noted in passing that such vdW repulsion might not apply for the case of smaller alcohols, e.g., ethanol, because they were shown capable replacing water molecules in the $H_3O^+_{hydr.}$ cluster, forming $(C_2H_5OH)(H_3O^+)(H_2O)_n$ cluster in zeolite channels.[24]

Thus, the charge of $H_3O^+_{hydr.}$ creates an ionic environment that can be expressed as the ionic strength in H-MFI micropores. Such an environment increases the standard free energy/excess chemical potential of the substrate ground state, i.e., it destabilizes the uncharged reacting ground state of cyclohexanol. The ionic environment stabilizes the positively charged transition state. Both effects together lead to a decrease of the activation free energy and enhance so the reaction rate. Such ionic environments in zeolites will also exist with other solvents. For example, methanol forms protonated clusters $H^+(CH_3OH)_n$ in small pores zeolites,[25] which would additionally allow to stabilize the charged transition state via the modulating solvent permittivity.[26]

The combination of the enhancement by the charged environment and the limitations by the additional spatial constraints from $H_3O^+_{hydr.}$ lead to a maximum in the catalytic activity of $H_3O^+_{hydr.}$ with varying $H_3O^+_{hydr.}$ concentrations. For H-MFI, the highest rates are observed when the volume between two neighboring $H_3O^+_{hydr.}$ equals to the vdW volume of substrate, i.e. concentrations of substrate and $H_3O^+_{hydr.}$ in the micropores are close to equal.

The final question arising is, however, how general these conclusions about reactivity in constrained environments are. To probe this, we explored a wide series of H-BEA zeolites (S-Table 2.1) and report here the first results of this study. The dependence of the rate of alcohol dehydration on the concentration of hydronium ions exhibits an analogous volcano-like dependence (Figure 2.4A). In particular, the variation of activation enthalpy and entropy with ionic strength show the similar profile shapes to H-MFI (Figure 2.4B, 4C), indicating the ionic strength influences catalytic activity via the identical mechanism. Note the curves shifting up and towards lower ionic strength on H-BEA compared to H-MFI, that is attributed to be the consequence of larger pore size of

H-BEA that induces less vdW stabilization of transition state. It is to be expected that the specific enhancement and the position of the maximum will subtly depend on the size of the reacting molecule and the difference in polarity between the reacting substrate and the transition state. Overall, the results demonstrate unequivocally that the quantitative interpretation of the catalytic activity will allow prediction of the most suitable microporous catalyst for reactions in the presence of active sites being associated with ions.

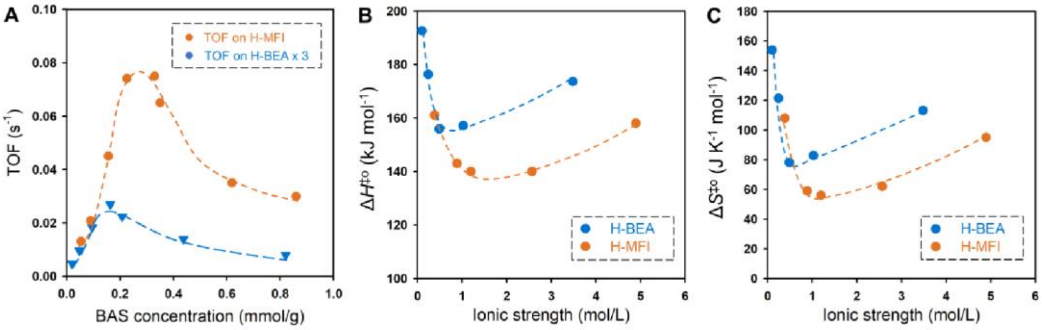

***Figure 2.4** Comparison of the dehydration reactions of cyclohexanol catalyzed by $H_3O^+_{hydr.}$ in H-MFI and H-BEA. (A) Impact of BAS concentration on the TOF at 423 K. (B) Activation enthalpy ($\Delta H^{‡o}$) and (C) activation entropy ($\Delta S^{‡o}$) as a function of ionic strength.*

2.3) Supplementary Materials

Role of the ionic environment to enhance activity of reacting molecules in zeolite pores

Content:

2.3.1) Materials and Methods

H-MFI (Si/Al 45, 60, 90 and 250) were obtained in the hydrogen form from Clariant. H-MFI (Si/Al 12, 15 and 40) were obtained from Zeolyst (CBV2314, CBV3024E, CBV8014). H-MFI (Si/Al 23) was prepared by mild dealumination of HMFI (15) using ammonium hexafluorosilicate (AHFS); H-MFI (Si/Al 26 and 32) were prepared by dealumination of HMFI (15) using AHFS under mild and severe conditions. H-MFI (Si/Al 200) was home hydrothermally synthesized. Their physicochemical properties are compiled in S-Table 2.1. Cyclohexanol (99.7 %) was purchased from Sigma Aldrich and was used as received.

Dealumination of H-MFI was carried out by treating 4 g of zeolite powder in 40 mL AHFS solution at 80 °C for 2 h. In a typical mild treatment, the amount of AHFS was equal to the Al amount in the loaded H-MFI; and four times more AHFS was used in a severe treatment. After the treatment, the powder was separated from the solution by centrifugation and washed with hot deionized water for three times. Then it was dried at 120 °C overnight and calcined in flowing air at 550 °C for 3 h. After cooling, the powder was stored and ready for use.

The hydrothermal synthesis of H-MFI (Si/Al 200) was carried out in the aqueous solution with composition of 10.75 Na_2O : 0.25 Al_2O_3 : 100 SiO_2 : 2000 H_2O : 20 TPABr. In a 36 mL H_2O solution of 1.38 g NaOH, 8.55 g tetrapropylammonium bromide (TPABr), 0.25 g $Al_2(SO_4)_3 \cdot H_2O$ and 32.1 g LUDOX-30 (Sigma-Aldrich, AS-30) were stepwise added under vigorous agitation. The gel formed was transferred to an autoclave and kept at 170 °C for 60 h under slow rotation. After drying overnight, the solid was calcined at 550 °C in 100 mL/min air for 6 h with a heating rate of 10 °C/min to remove the template. Thus Na form MFI was obtained. It was then exchanged to NH_4 form via ion exchange in 50 mL 1 mol/L NH_4NO_3 solution. After centrifugation and washing with deionized water, it was calcined to H-MFI using the same calcination procedure as described above.

The H-BEA zeolite was synthesized in the presence of fluoride anions following a reported method.([27,28]) In brief, the H-BEA was prepared by a hydrothermal synthesis at 140°C, with an initial gel composition: SiO2: xAl2O3 : (0.54 + 2x) TEAOH : (0.54 + 2x) HF : (7 + 2x) H2O. Then it was washed with deionized water and filtered, followed by calcination at 500 °C for 2 h under air. The H-BEA was then obtained as a powder and ready for use. By changing the gel composition, i.e. x indicated in the formula, HBEA with different Si/Al ratios (15 to 400) were prepared.

Aqueous-phase dehydration reactions were performed in a 300ml Hastelloy Parr autoclave. Typically, 100 ml 0.33 M aqueous cyclohexanol solution and a specific amount of catalyst (for example, 100–200 mg for zeolites) were loaded in the reactor. The closed reactor was then pressurized with 40 bar H_2 at room temperature and heated under agitation of 700 rpm. The reaction time was based on the point when the set temperature was reached (10–15 min). At the end of a reaction, the reactor was cooled with an ice/water mixture to below 277 K. The reaction mixture of cyclohexene (oil phase) and cyclohexanol-containing aqueous phase was extracted using dichloromethane and analyzed on an Agilent 7890A gas chromatograph (GC) equipped with a HP-5MS column, coupled with Agilent 5975C MS.

2.3.2) Supplementary Text

S2.1 Calculation of free energy barrier and excess chemical potential of ground and transition state in cyclohexanol dehydration in H-MFI.

The activity coefficient of adsorbed cyclohexanol increases exponentially with ionic strength, which is quantifiable by a salting-out model:

$$\log_{10}\left(\gamma_{\mathrm{Cy,ad}}\right)=K_{\mathrm{s}}I_{\mathrm{HMFI}} \tag{S-2.1}$$

in which K_s is the Setschenow constant. The standard state chemical potential of adsorbed cyclohexanol is a function of ionic strength (I_{HMFI}) in H-MFI, $\mu^{o}_{\mathrm{Cy,ad}}(I_{HMFI})$, expressed as

$$\mu^{\mathrm{o}}_{\mathrm{Cy,ad}}(I_{\mathrm{HMFI}})=\mu^{\mathrm{o}}_{\mathrm{Cy,ad}}(0)+RT\ln\gamma_{\mathrm{Cy,ad}}=\mu^{\mathrm{o}}_{\mathrm{Cy,ad}}(0)+2.303\cdot RTK_{\mathrm{s}}I_{\mathrm{HMFI}} \tag{S-2.2}$$

The $\mu^{o}_{\mathrm{Cy,ad}}(0)$ is the chemical potential of cyclohexanol adsorbed in MFI zeolite free of ions (I = 0), e.g. purely siliceous MFI. For the adsorption of cyclohexanol from the aqueous phase in H-MFI with an ionic strength of I_{HMFI}, the adsorption constant K^{o}_{ad} is expressed as

$$K^{\mathrm{o}}_{\mathrm{ad}}=\exp\left[-\frac{\mu^{\mathrm{o}}_{\mathrm{Cy,ad}}(I_{\mathrm{HMFI}})-\mu^{\mathrm{o}}_{\mathrm{Cy,aq}}}{RT}\right]=\exp\left[-\frac{\mu^{\mathrm{o}}_{\mathrm{Cy,ad}}(0)-\mu^{\mathrm{o}}_{\mathrm{Cy,aq}}}{RT}\right]\cdot 10^{-K_{\mathrm{s}}I_{\mathrm{HMFI}}} \tag{S-2.3}$$

This equation predicts that K^{o}_{ad} increases exponentially with the I_{HMFI}.

Based on the Gibbs-Helmholtz equation, the adsorption heat ΔQ_{ad} and enthalpy ΔH^{o}_{ad} are given by equation (S-2.4).

$$\frac{\Delta Q_{\mathrm{ad}}}{T^{2}}=-\frac{\Delta H^{\mathrm{o}}_{\mathrm{ad}}}{T^{2}}=\left(\frac{\partial\left(\Delta G^{\mathrm{o}}_{\mathrm{ad}}/T\right)}{\partial T}\right)_{p}=-\left(\frac{\partial\left(R\ln K^{\mathrm{o}}_{\mathrm{ad}}\right)}{\partial T}\right)_{p} \tag{S-2.4}$$

Under constant temperature and pressure, using the expression of K^{o}_{ad} in Equation S-2.3 allows Equation S-2.4 to be reformulated as following:

$$\Delta Q_{\mathrm{ad}}=-\frac{\mathrm{d}\left(\left(\mu^{\mathrm{o}}_{\mathrm{Cy,ad}}(0)-\mu^{\mathrm{o}}_{\mathrm{Cy,aq}}\right)/T\right)}{\mathrm{d}\left(1/T\right)}-2.303\cdot RI_{\mathrm{HMFI}}\cdot\frac{\mathrm{d}K_{\mathrm{s}}}{\mathrm{d}\left(1/T\right)} \tag{S-2.5}$$

$$\frac{\mathrm{d}K_\mathrm{s}}{\mathrm{d}\left(1/T\right)} = -\frac{1}{2.303\cdot R}\cdot\frac{\mathrm{d}\Delta Q_\mathrm{ad}}{dI_\mathrm{HMFI}} \tag{S-2.6}$$

Equation S-2.6 gives the variation of K_s with T.

S-Figure 2.2 shows the measured $K^{\mathrm{o}}_{\mathrm{ad}}$ and ΔQ_{ad} of cyclohexanol on H-MFI with different ionic strength at 298 K. By regression of the two plots using equations S-2.6 and S-2.9, K_s at 298 K is determined to be 1.3 ± 0.1 and $dK_s/d(1/T)$ is 95 ± 10 K. Assuming that $dK_s/d(1/T)$ is invariant with temperature, the K_s at 423 K is calculated to be 0.04 ± 0.02.

$$K_\mathrm{s}(423\ \mathrm{K}) = K_\mathrm{s}(298\ \mathrm{K}) + \frac{\mathrm{d}K_\mathrm{s}}{\mathrm{d}(1/T)}\cdot\left(\frac{1}{423\ \mathrm{K}} - \frac{1}{298\ \mathrm{K}}\right) = 0.04 \pm 0.02 \tag{S-2.7}$$

Thus the excess chemical potential of sorbed cyclohexnanol in H-MFI as reacting ground state ($\mu^{\mathrm{excess}}_{\mathrm{GS}}$) is calculated by

$$\mu^{\mathrm{excess}}_{\mathrm{GS}} = 2.303\cdot RTK_\mathrm{s}I \tag{S-2.8}$$

The excess chemical potential of transition state ($\mu^{\mathrm{excess}}_{\mathrm{TS}}$) is calculated by

$$\mu^{\mathrm{excess}}_{\mathrm{TS}} = \Delta G^{\circ\ddagger}(I) - \Delta G^{\circ\ddagger}_{(\mathrm{ideal})} + \mu^{\mathrm{excess}}_{\mathrm{GS}} \tag{S-2.9}$$

The $\Delta G^{o\ddagger}_{(ideal)}$ and $\Delta G^{o\ddagger}(I)$ are the free energy barrier under ideal condition and in the presence of an ionic strength, respectively. They are obtained from the measured reaction TOF using transition state formula.

$$\mathrm{TOF}_{(\mathrm{ideal})} = \frac{k_\mathrm{B}T}{h}\exp\left(-\frac{\Delta G^{\circ\ddagger}_{(\mathrm{ideal})}}{RT}\right) \tag{S-2.10}$$

$$\mathrm{TOF}(I) = \frac{k_\mathrm{B}T}{h}\exp\left(-\frac{\Delta G^{\circ\ddagger}(I)}{RT}\right) \tag{S-2.11}$$

The $TOF_{(ideal)}$ under the ideal condition was obtained as 0.010 ± 0.001 s^{-1} by extrapolating the TOF to zero ionic strength, because it is experimentally impossible to measure the reaction rate of an H-MFI with zero ionic strength, i.e., without BAS.

Taking the relation of $\Delta G^{o\ddagger}_{(ideal)}$ and $\Delta G^{o\ddagger}(I)$ in Equation S-2.9 into Equation S-2.11, gives

$$\begin{aligned}\mathrm{TOF}(I) &= \frac{k_{\mathrm{B}}T}{h}\exp\left(-\frac{\Delta G^{\circ\ddagger}(I)}{RT}\right) = \frac{k_{\mathrm{B}}T}{h}\exp\left(-\frac{\Delta G^{\circ\ddagger}_{\mathrm{(ideal)}} + \mu^{\mathrm{excess}}_{\mathrm{TS}} - \mu^{\mathrm{excess}}_{\mathrm{GS}}}{RT}\right) \\ &= \frac{k_{\mathrm{B}}T}{h}\exp\left(-\frac{\Delta G^{\circ\ddagger}_{\mathrm{(ideal)}}}{RT}\right)\exp\left(-\frac{\mu^{\mathrm{excess}}_{\mathrm{TS}}}{RT}\right)\exp\left(\frac{\mu^{\mathrm{excess}}_{\mathrm{GS}}}{RT}\right) = \mathrm{TOF}_{\mathrm{(ideal)}}\cdot\frac{\gamma_{\mathrm{GS}}(I)}{\gamma_{\mathrm{TS}}(I)}\end{aligned} \qquad \text{(S-2.12)}$$

This Equation S-2.12 is Equation (2.2a) in the main text.

S2.2 Calculation of TOF in cyclohexanol dehydration in H-MFI via partition function analysis.

The cyclohexanol (A for short) adsorbs in zeolite pore channels, reacting through a transition state (‡) to the product. Assuming there are N adsorption sites in the pore channel and no interaction between adsorbed species. When N_A amount of cyclohexanol adsorbed and $N^‡$ amount of transition state exist for the reaction ($N_A >> N^‡$), the canonical partition function $Q(N, N_A, N^‡)$ at constant temperature is expressed as:

$$Q\left(N, N_{\mathrm{A}}, N^{\ddagger}\right)=\frac{N!}{N_{\mathrm{A}}!N^{\ddagger}!(N-N_{\mathrm{A}}-N^{\ddagger})!}\cdot q_{\mathrm{A,p}}^{N_{\mathrm{A}}}\cdot q_{\ddagger,\mathrm{p}}^{N^{\ddagger}} \tag{S-2.13}$$

where $q_{A,p}$ and $q_{‡,p}$ are the molecular partition function of A and reacting transition state in the pore, respectively. Then the chemical potential of A ($\mu_{A,p}$) and transition state ($\mu_{‡,p}$) are expressed by

$$\mu_{\mathrm{A,p}}=-k_{\mathrm{B}}T\frac{\partial\ln Q\left(N,N_{\mathrm{A}},N^{\ddagger}\right)}{\partial N_{\mathrm{A}}}=-k_{\mathrm{B}}T\ln q_{\mathrm{A,p}}-k_{\mathrm{B}}T\frac{\partial\left[\ln N!-\ln N_{\mathrm{A}}!-\ln N^{\ddagger}!-\ln(N-N_{\mathrm{A}}-N^{\ddagger})!\right]}{\partial N_{\mathrm{A}}} \tag{S-2.14a}$$

$$\mu_{\ddagger,\mathrm{p}}=-k_{\mathrm{B}}T\frac{\partial\ln Q\left(N,N_{\mathrm{A}},N^{\ddagger}\right)}{\partial N^{\ddagger}}=-k_{\mathrm{B}}T\ln q_{\ddagger,\mathrm{p}}-k_{\mathrm{B}}T\frac{\partial\left[\ln N!-\ln N_{\mathrm{A}}!-\ln N^{\ddagger}!-\ln(N-N_{\mathrm{A}}-N^{\ddagger})!\right]}{\partial N^{\ddagger}} \tag{S-2.14b}$$

Applying Stirling approximation, equation (S-2.14) is transformed into equation (S-2.15).

$$\begin{aligned}\mu_{\mathrm{A,p}}&=-k_{\mathrm{B}}T\ln q_{\mathrm{A,p}}-k_{\mathrm{B}}T\frac{\partial}{\partial N_{\mathrm{A}}}\left[N\ln N-N_{\mathrm{A}}\ln N_{\mathrm{A}}-N^{\ddagger}\ln N^{\ddagger}-(N-N_{\mathrm{A}}-N^{\ddagger})\ln(N-N_{\mathrm{A}}-N^{\ddagger})\right]\\&=-k_{\mathrm{B}}T\ln q_{\mathrm{A,p}}-k_{\mathrm{B}}T\left[-\ln N_{\mathrm{A}}-1+\ln(N-N_{\mathrm{A}}-N^{\ddagger})+1\right]\\&=-k_{\mathrm{B}}T\ln q_{\mathrm{A,p}}+k_{\mathrm{B}}T\ln\frac{N_{\mathrm{A}}}{N-N_{\mathrm{A}}-N^{\ddagger}}\end{aligned} \tag{S-2.15a}$$

$$\begin{aligned}\mu_{\ddagger,\mathrm{p}}&=-k_{\mathrm{B}}T\ln q_{\ddagger,\mathrm{p}}-k_{\mathrm{B}}T\frac{\partial}{\partial N^{\ddagger}}\left[N\ln N-N_{\mathrm{A}}\ln N_{\mathrm{A}}-N^{\ddagger}\ln N^{\ddagger}-(N-N_{\mathrm{A}}-N^{\ddagger})\ln(N-N_{\mathrm{A}}-N^{\ddagger})\right]\\&=-k_{\mathrm{B}}T\ln q_{\ddagger,\mathrm{p}}-k_{\mathrm{B}}T\left[-\ln N^{\ddagger}-1+\ln(N-N_{\mathrm{A}}-N^{\ddagger})+1\right]\\&=-k_{\mathrm{B}}T\ln q_{\ddagger,\mathrm{p}}+k_{\mathrm{B}}T\ln\frac{N^{\ddagger}}{N-N_{\mathrm{A}}-N^{\ddagger}}\end{aligned} \tag{S-2.15b}$$

Number of transition states $N^‡$ are very small ($N_A >> N^‡$). So the $\mu_{A,p}$ and $\mu_{‡,p}$ are further expressed by

$$\mu_{\mathrm{A,p}}=-k_{\mathrm{B}}T\ln q_{\mathrm{A,p}}+k_{\mathrm{B}}T\ln\frac{N_{\mathrm{A}}}{N-N_{\mathrm{A}}} \tag{S-2.16a}$$

$$\mu_{\ddagger,\mathrm{p}} = -k_{\mathrm{B}}T\ln q_{\ddagger,\mathrm{p}} + k_{\mathrm{B}}T\ln\frac{N^{\ddagger}}{N-N_{\mathrm{A}}} \quad \text{(S-2.16b)}$$

Coverage (θ) is often used to describe an adsorption process. In this particular case the coverage of A is defined as $\theta_A = N_A / N$; and that of transition state is defined as $\theta^{\ddagger} = N^{\ddagger} / N$. The equations (S-2.16a and b) are then expressed as:

$$\mu_{\mathrm{A,p}} = -k_{\mathrm{B}}T\ln q_{\mathrm{A,p}} + k_{\mathrm{B}}T\ln\frac{\theta_{\mathrm{A}}}{1-\theta_{\mathrm{A}}} \quad \text{(S-2.17a)}$$

$$\mu_{\ddagger,\mathrm{p}} = -k_{\mathrm{B}}T\ln q_{\ddagger,\mathrm{p}} + k_{\mathrm{B}}T\ln\frac{\theta^{\ddagger}}{1-\theta_{\mathrm{A}}} \quad \text{(S-2.17b)}$$

Equations (S-2.17) are the chemical potential under ideal condition. When accounting the interactions under non-ideal conditions, it is corrected by an activity coefficient term, $\gamma_{A,p}$ or $\gamma_{\ddagger,p}$

$$\mu_{\mathrm{A,p}} = -k_{\mathrm{B}}T\ln q_{\mathrm{A,p}} + k_{\mathrm{B}}T\ln\frac{\theta_{\mathrm{A}}}{1-\theta_{\mathrm{A}}} + k_{\mathrm{B}}T\ln\gamma_{\mathrm{A,p}} \quad \text{(S-2.18a)}$$

$$\mu_{\ddagger,\mathrm{p}} = -k_{\mathrm{B}}T\ln q_{\ddagger,\mathrm{p}} + k_{\mathrm{B}}T\ln\frac{\theta^{\ddagger}}{1-\theta_{\mathrm{A}}} + k_{\mathrm{B}}T\ln\gamma_{\ddagger,\mathrm{p}} \quad \text{(S-2.18b)}$$

Consider a catalyst having local ionic strength (I) coexist with an ideal catalyst (I = 0). Under equilibrium, A and transition state in both catalysts have the same chemical potential, respectively:

$$-k_{\mathrm{B}}T\ln q_{\mathrm{A,p}} + k_{\mathrm{B}}T\ln\frac{\theta_{\mathrm{A}}(I)}{1-\theta_{\mathrm{A}}(I)} + k_{\mathrm{B}}T\ln\gamma_{\mathrm{A,p}}(I) = -k_{\mathrm{B}}T\ln q_{\mathrm{A,p}} + k_{\mathrm{B}}T\ln\frac{\theta_{\mathrm{A}}(0)}{1-\theta_{\mathrm{A}}(0)} \quad \text{(S-2.19a)}$$

$$-k_{\mathrm{B}}T\ln q_{\ddagger,\mathrm{p}} + k_{\mathrm{B}}T\ln\frac{\theta^{\ddagger}(I)}{1-\theta_{\mathrm{A}}(I)} + k_{\mathrm{B}}T\ln\gamma_{\ddagger,\mathrm{p}}(I) = -k_{\mathrm{B}}T\ln q_{\ddagger,\mathrm{p}} + k_{\mathrm{B}}T\ln\frac{\theta^{\ddagger}(0)}{1-\theta_{\mathrm{A}}(0)} \quad \text{(S-2.19b)}$$

The I in parentheses represents the ionic strength in the zeolite, while the value of 0 refers to the ideal zeolite. The Equations S-2.19 is reformulated to

$$k_{\mathrm{B}}T\ln\frac{\theta_{\mathrm{A}}(I)}{\theta_{\mathrm{A}}(0)} + k_{\mathrm{B}}T\ln\gamma_{\mathrm{A,p}}(I) = k_{\mathrm{B}}T\ln\frac{1-\theta_{\mathrm{A}}(I)}{1-\theta_{\mathrm{A}}(0)} \quad \text{(S-2.20a)}$$

$$k_{\mathrm{B}}T\ln\frac{\theta^{\ddagger}(I)}{\theta^{\ddagger}(0)} + k_{\mathrm{B}}T\ln\gamma_{\ddagger,\mathrm{p}}(I) = k_{\mathrm{B}}T\ln\frac{1-\theta_{\mathrm{A}}(I)}{1-\theta_{\mathrm{A}}(0)} \quad \text{(S-2.20b)}$$

Noticing that the right part of Equation S-2.20a and S-2.20b are the same, therefore their left parts equal.

$$k_\mathrm{B}T\ln\frac{\theta_\mathrm{A}(I)}{\theta_\mathrm{A}(0)}+k_\mathrm{B}T\ln\gamma_\mathrm{A,p}(I)=k_\mathrm{B}T\ln\frac{\theta^\ddagger(I)}{\theta^\ddagger(0)}+k_\mathrm{B}T\ln\gamma_{\ddagger,\mathrm{p}}(I) \tag{S-2.21}$$

This gives the expression of transition state ratio

$$\frac{\theta^\ddagger(I)}{\theta^\ddagger(0)}=\frac{\theta_\mathrm{A}(I)}{\theta_\mathrm{A}(0)}\cdot\frac{\gamma_\mathrm{A,p}(I)}{\gamma_{\ddagger,\mathrm{p}}(I)} \tag{S-2.22}$$

Under reaction order of zero, zeolite pore is saturated by A, i.e. $\theta_A(I) = \theta_A(0)$. The ratio of $\theta^\ddagger(I) / \theta^\ddagger(0)$ is the ratio of TOF(I) / TOF(0), because transition state has a constant frequency to convert to product. So Equation S22 transforms into

$$\frac{\mathrm{TOF}(I)}{\mathrm{TOF}(0)}=\frac{\gamma_\mathrm{A,p}(I)}{\gamma_{\ddagger,\mathrm{p}}(I)} \tag{S-2.23a}$$

$$\mathrm{TOF}(I)=\mathrm{TOF}(0)\cdot\frac{\gamma_\mathrm{A,p}(I)}{\gamma_{\ddagger,\mathrm{p}}(I)} \tag{S-2.23b}$$

The Equation S23b is essentially Equation (2.2a) in the main text.

S2.3 Determination of the number of water molecules constituting a hydronium ion in H-MFI

The number of water molecules (n_{H_2O}) constituting a hydronium ion in H-MFI was determined by the approach described in a previous work ([29]). In brief, three steps were involved: (1) determining the saturated uptake (q_{sat}) of a substrate (e.g. cyclohexanol, phenol) from the aqueous phase in H-MFI zeolite and the volumetric uptake in the micropore (V_{sub}); (2) calculating the volume (V_{hydr}) in the micropore that is occupied by the hydronium ions; (3) repeat the two steps on H-MFI with different BAS concentrations (c_{BAS}).

Under saturated adsorption, the adsorbed substrate and hydronium ions takes up all the micropore space of H-MFI (Eq. S-2.24). The volume taken by hydronium ions are proportional to its concentration in micropores (Eq. S-2.25).

$$V_{\mathrm{sub}} + V_{\mathrm{hydr}} = V_{\mathrm{micr}} \tag{S-2.24}$$

$$V_{\mathrm{hydr}} = n_{\mathrm{H_2O}} \cdot V_{\mathrm{m,H_2O}} \cdot c_{\mathrm{BAS}} \tag{S-2.25}$$

The V_{micr} is the micropore volume of H-MFI zeolite; V_{M,H_2O} is the molar volume of water. Here it is assumed that water in the hydronium ion has the same packing density as that of free water. By determining V_{hydr} on a series of H-MFI with varying c_{BAS}, their plot shows a linear correlation (S-Figure 2.4). Then n_{H_2O} is obtained from the quotient of the slope to V_{M,H_2O} (Eq. S-2.25), and is shown to be invariant with temperature (S-Figure 2.5).

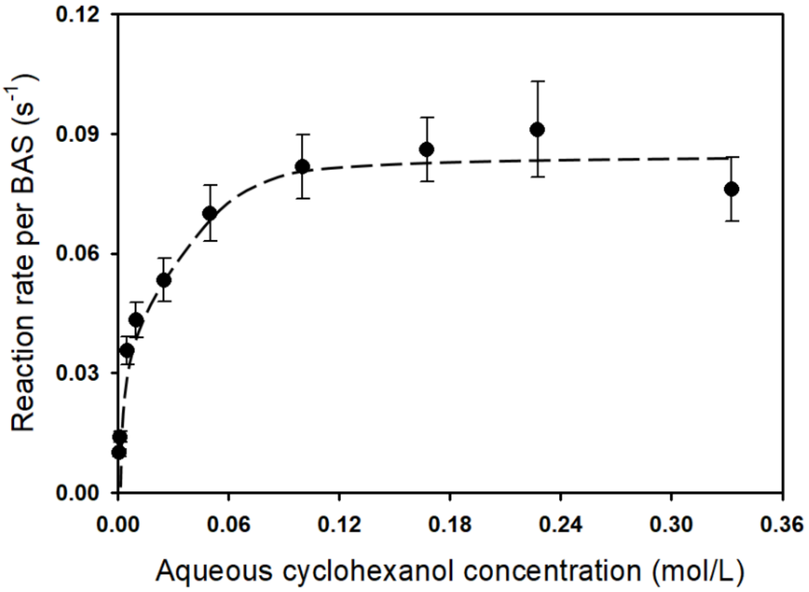

S-Figure 2.1 *BAS normalized dehydration rate of cyclohexanol on H-MFI (Si/Al 45) as a function of aqueous cyclohexanol concentration. This work chooses the zeroth order reaction region, i.e. cyclohexnaol concentration above 0.1 mol/L for the rate comparison and kinetic analysis.*

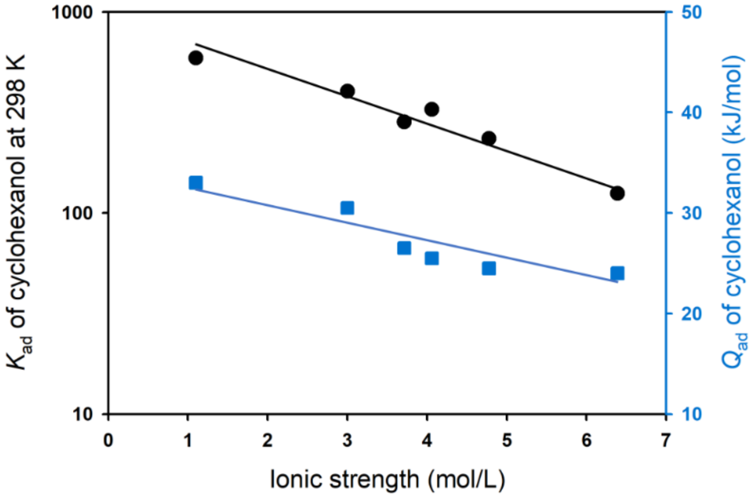

S-Figure 2.2 *Influence of ionic strength in H-MFI on the adsorption constant (K_{ad}^{o}) and adsorption heat (Q_{ad}) of cyclohexanol at 298 K. The values are reported previously in reference ([29]), and the one first from the right is measured on H-MFI (Si/Al 12) in this work, see S-Figure 2.5*

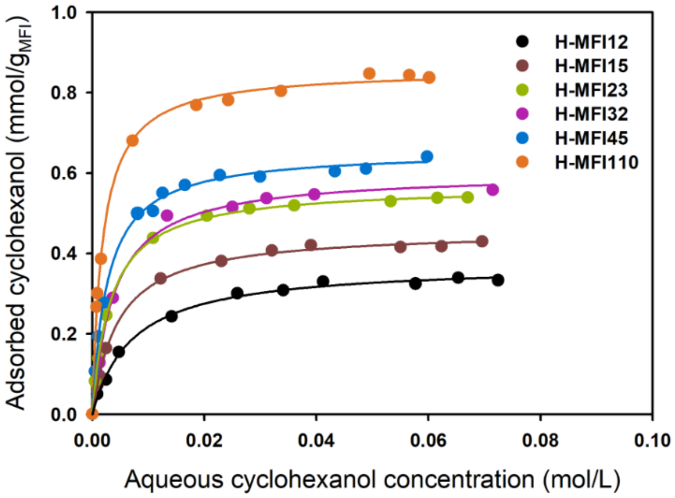

S-Figure 2.3 *Adsorption isotherm of cyclohexanol on H-MFI zeolite in aqueous phase at 298 K. The data for H-MFI110, H-MFI45, H-MFI32, H-MFI23 and H-MFI15 are reported previously in reference (*[29]*).*

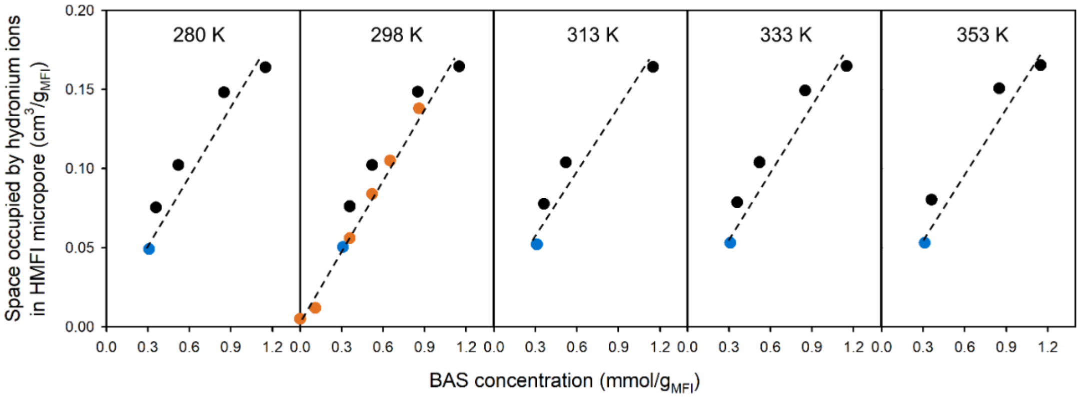

S-Figure 2.4 *Micropore space volume occupied by hydronium ions in H-MFI in water as a function of the BAS concentration. Black data points (●) were from reference (*[30]*); Blue data points (●) were from reference (*[10]*); Orange data points (●) were from reference (*[29]*).*

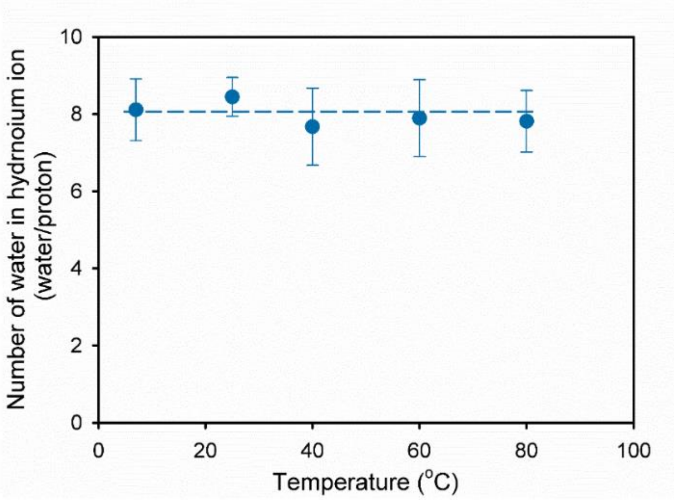

S-Figure 2.5 *Number of water molecules constituting a hydronium ion in H-MFI at different temperatures.*

S-Table 2.1 *Physicochemical properties of H-MFI zeolite samples*

Sample	Si/Al ratio	BAS concentration (mmol/g)	Micropore volume (cm^3/g)	Ionic strength[a] (mol/L)	$H_3O^+_{hydr.}$ per unit cell[b]
H-MFI12	12	1.15	0.18	6.4	6.6
H-MFI15	15	0.86	0.18	4.8	4.9
H-MFI23	23	0.65	0.16	4.1	3.7
H-MFI26	26	0.62	0.16	3.9	3.6
H-MFI32	32	0.52	0.14	3.7	3.0
H-MFI40	40	0.35	0.15	2.3	2.0
H-MFI45	45	0.31	0.12	2.6	1.8
H-MFI60	60	0.23	0.15	1.5	1.3
H-MFI90	90	0.15	0.13	1.2	0.9
H-MFI200	200	0.090	0.10	0.90	0.52
H-MFI250	250	0.054	0.14	0.39	0.31
H-BEA15	15	0.82	0.24	3.5	3.2
H-BEA25	25	0.44	0.21	2.1	1.7
H-BEA50	50	0.21	0.20	1.0	0.81
H-BEA75	75	0.16	0.20	0.80	0.62
H-BEA100	100	0.095	0.19	0.50	0.36
H-BEA200	200	0.047	0.19	0.25	0.18
H-BEA400	400	0.020	0.19	0.11	0.08

[a] calculated by normalizing BAS concentration to micropore volume

[b] calculated by the BAS concentration per weight of zeolite (mmol/g) multiplying the weight of unit cell (5760 $g/mol_{UnitCell}$ for MFI and 3840 $g/mol_{UnitCell}$ for BEA). Unit cell compositions of $H_xAl_xSi_{96-x}O_{192}$ for H-MFI and $H_xAl_xSi_{64-x}O_{128}$ for H-BEA based on database of Structure Commission of the International Zeolite Association (IZA-SC), reference to http://www.iza-structure.org/databases/micropore volume.

2.4) References

1 Gounder, R. & Iglesia, E. Catalytic consequences of spatial constraints and acid site location for monomolecular alkane activation on zeolites. *J. Am. Chem. Soc.* **131**, 1958-1971, doi:10.1021/ja808292c (2009).

2 Tian, P., Wei, Y., Ye, M. & Liu, Z. Methanol to olefins (MTO): From fundamentals to commercialization. *ACS Catal.* **5**, 1922-1938, doi:10.1021/acscatal.5b00007 (2015).

3 Vermeiren, W. & Gilson, J. P. Impact of zeolites on the petroleum and petrochemical industry. *Top. Catal.* **52**, 1131-1161, doi:10.1007/s11244-009-9271-8 (2009).

4 Vogt, E. T. C. & Weckhuysen, B. M. Fluid catalytic cracking: recent developments on the grand old lady of zeolite catalysis. *Chem. Soc. Rev.* **44**, 7342-7370, doi:10.1039/c5cs00376h (2015).

5 Woolery, G. L., Kuehl, G. H., Timken, H. C., Chester, A. W. & Vartuli, J. C. On the nature of framework Brønsted and Lewis acid sites in ZSM-5. *Zeolites* **19**, 288-296, doi:Doi 10.1016/S0144-2449(97)00086-9 (1997).

6 Barthomeuf, D. Conjugate acid-base pairs in zeolites. *J. Phys. Chem.* **88**, 42-45, doi:DOI 10.1021/j150645a010 (1984).

7 Mirodatos, C. & Barthomeuf, D. Cracking of n-decane on zeolite catalysts - Enhancement of light-hydrocarbon formation by the zeolite field gradient. *J. Catal.* **114**, 121-135, doi:Doi 10.1016/0021-9517(88)90014-0 (1988).

8 Stach, H. *et al.* Mordenite acidity: dependence on the silicon/aluminum ratio and the framework aluminum topology. 2. Acidity investigations. *J. Phys. Chem.* **96**, 8480-8485, doi:10.1021/j100200a051 (1992).

9 Auroux, A. Acidity characterization by microcalorimetry and relationship with reactivity. *Top. Catal.* **4**, 71-89, doi:10.1023/A:1019127919907 (1997).

10 Shi, H., Eckstein, S., Vjunov, A., Camaioni, D. M. & Lercher, J. A. Tailoring nanoscopic confines to maximize catalytic activity of hydronium ions. *Nature Communications* **8**, 15442, doi:10.1038/ncomms15442

https://www.nature.com/articles/ncomms15442#supplementary-information (2017).

11 Liu, Y. *et al.* Enhancing the catalytic activity of hydronium ions through constrained environments. *Nature Communications* **8**, 14113, doi:10.1038/ncomms14113

https://www.nature.com/articles/ncomms14113#supplementary-information (2017).

12 Wang, S. & Iglesia, E. Catalytic diversity conferred by confinement of protons within porous aluminosilicates in Prins condensation reactions. *J. Catal.* **352**, 415-435, doi:10.1016/j.jcat.2017.06.012 (2017).

13 Jones, A. J., Zones, S. I. & Iglesia, E. Implications of transition state confinement within small voids for acid catalysis. *J. Phys. Chem. C* **118**, 17787-17800, doi:10.1021/jp5050095 (2014).

14 Margarit, V. J. *et al.* Control of the reaction mechanism of alkylaromatics transalkylation by means of molecular confinement effects associated to zeolite channel architecture. *ACS Catal.* **9**, 5935-5946, doi:10.1021/acscatal.9b00763 (2019).

15 Eckstein, S. *et al.* Influence of hydronium ions in yeolites on sorption. *Angew. Chem. Int. Ed.* **58**, 3450-3455, doi:10.1002/anie.201812184 (2019).

16 Schallmoser, S. *et al.* Impact of the local environment of Brønsted acid sites in ZSM-5 on the catalytic activity in n-pentane cracking. *J. Catal.* **316**, 93-102, doi:doi.org/10.1016/j.jcat.2014.05.004 (2014).

17 Haag, W. O., Lago, R. M. & Weisz, P. B. The active-site of acidic aluminosilicate catalysts. *Nature* **309**, 589-591, doi:DOI 10.1038/309589a0 (1984).

18 Parrillo, D. J., Lee, C. & Gorte, R. J. Heats of adsorption for ammonia and pyridine in H-ZSM-5: evidence for identical Brønsted-acid sites. *Appl. Catal. A* **110**, 67-74 (1994).

19 Janda, A. & Bell, A. T. Effects of Si/Al Ratio on the Distribution of Framework Al and on the Rates of Alkane Monomolecular Cracking and Dehydrogenation in H-MFI. *Journal of the American Chemical Society* **135**, 19193-19207, doi:10.1021/ja4081937 (2013).

20 Knott, B. C. *et al.* Consideration of the Aluminum Distribution in Zeolites in Theoretical and Experimental Catalysis Research. *ACS Catal.* **8**, 770-784, doi:10.1021/acscatal.7b03676 (2018).

21 Luo, W. *et al.* Zeolite-supported metal catalysts for selective hydrodeoxygenation of biomass-derived platform molecules. *Green Chemistry* **21**, 3744-3768, doi:10.1039/C9GC01216H (2019).

22 Zhi, Y. *et al.* Dehydration Pathways of 1-Propanol on HZSM-5 in the Presence and Absence of Water. *Journal of the American Chemical Society* **137**, 15781-15794, doi:10.1021/jacs.5b09107 (2015).

23 Olson, D. H., Kokotailo, G. T., Lawton, S. L. & Meier, W. M. Crystal-structure and structure-related properties of ZSM-5. *J. Phys. Chem.* **85**, 2238-2243, doi:DOI 10.1021/j150615a020 (1981).

24 Bates, J. S., Bukowski, B. C., Greeley, J. & Gounder, R. Structure and solvation of confined water and water–ethanol clusters within microporous Brønsted acids and their effects on ethanol dehydration catalysis. *Chemical Science* **11**, 7102-7122, doi:10.1039/D0SC02589E (2020).

25 Di Iorio, J. R. *et al.* Mechanistic origins of the high-pressure inhibition of methanol dehydration rates in small-pore acidic zeolites. *Journal of Catalysis* **380**, 161-177, doi:https://doi.org/10.1016/j.jcat.2019.10.012 (2019).

26 Murzin, D. Y. Solvent effects in catalysis: implementation for modelling of kinetics. *Catalysis Science & Technology* **6**, 5700-5713, doi:10.1039/c6cy00495d (2016).

27 A. Camblor, M., Corma, A. & Valencia, S. Synthesis in fluoride media and characterisation of aluminosilicate zeolite beta. *Journal of Materials Chemistry* **8**, 2137-2145, doi:10.1039/A804457K (1998).

28 Prodinger, S., Shi, H., Wang, H., Derewinski, M. A. & Lercher, J. A. Impact of structural defects and hydronium ion concentration on the stability of zeolite BEA in aqueous phase. *Applied Catalysis B: Environmental* **237**, 996-1002, doi:https://doi.org/10.1016/j.apcatb.2018.06.065 (2018).

29 Eckstein, S. *et al.* Influence of Hydronium Ions in Zeolites on Sorption. *Angewandte Chemie International Edition* **58**, 3450-3455, doi:10.1002/anie.201812184 (2019).

30 Eckstein, S. *et al.* Elementary steps and reaction pathways in the aqueous phase alkylation of phenol with ethanol. *Journal of Catalysis* **352**, 329-336, doi:https://doi.org/10.1016/j.jcat.2017.06.002 (2017).

3) Impact of the local concentration of hydronium ions at tungstate surfaces for acid-catalyzed alcohol dehydration

Niklas Pfriem,[1] Yue Liu,[1] Florian Zahn,[1] Hui Shi,[2,*] Gary L. Haller[1,3] and Johannes A. Lercher[1,4,*]

[1] Department of Chemistry and Catalysis Research Center, TU München, Garching 85747, Germany

[2] School of Chemistry and Chemical Engineering, Yangzhou University, Yangzhou, Jiangsu 225009, China

[3] Yale University, Department of Chemical and Environmental Engineering, New Haven, CT 06520-8682, USA

[4] Institute for Integrated Catalysis, Pacific Northwest National Laboratory, P.O. Box 999, Richland, WA 99352, United States

*Correspondence to: shihui@yzu.edu.cn (H.S.); johannes.lercher@ch.tum.de (J.A.L.)

Authors contributions: H.S. and J.A.L. conceived the research; N.P. measured catalytic activities, analyzed the physicochemical properties of the catalysts and drafted the manuscript. F.Z. measured physicochemical properties and helped finalizing the manuscript. G.L.H. helped analyzing the data.

This work has been published:
https://pubs.acs.org/doi/10.1021/jacs.1c07203

3.1) Abstract

Tungstate domains supported on ZrO_2, Al_2O_3, TiO_2, and activated carbon drastically influence the hydronium-ion-catalyzed aqueous phase dehydration of alcohols. For all catalysts, the rate of cyclohexanol dehydration normalized to the concentration of Brønsted acid sites (turnover frequencies, TOFs) was lower for monotungstates than for polytungstates and larger crystallites of WO_3. TOFs were constant, when reaching or exceeding the monolayer coverage of tungstate, irrespective of the specific nature of surface structures that continuously evolve with surface W loading. However, the TOFs with polytungstates and large WO_3 crystallites depend strongly on the underlying support (e.g., WO_x/C catalysts are 10-50 fold more active than WO_x/Al_2O_3 catalysts). The electrical double layer (EDL), surrounding the negatively charged WO_x domains, contain hydrated hydronium ions, whose local concentrations change with the support. This varying concentration of interfacial hydronium ions ("local ionic strength") impacts the excess chemical potential of the reacting alcohols and induces the marked differences in the TOFs. Primary H/D kinetic isotope effects (~3), together with the substantially positive entropy of activation (111-195 J mol^{-1} K^{-1}), indicate that C–H(D) bond cleavage is involved in the kinetically relevant step of an E1-type mechanistic sequence, regardless of the support identity. The remarkable support dependence of catalytic activity observed here for aqueous-phase dehydration of cycloalkanols likely applies to a broad set of hydronium-ion-catalyzed organic reactions sensitive to ionic strength.

3.2) Introduction

Tungsten oxide (WO_x)-based solid acids have been intensively characterized in terms of the inorganic structures and widely employed as catalysts in gas-phase isomerization reactions of linear alkanes and o-xylene,[1-11]alcohol dehydration[5,12-15] and liquid-phase upgrading of biomass-derived feedstocks (e.g., sugars and bio-oils[16-18]).

General agreement exists that the catalytic activity of the tungstated catalysts depends on the structure of the WO_x species and their interactions with the support.[11] For isomerization and dehydration reactions at a gas-solid interface, Iglesia and coworkers[12,19-21] showed that the total-W-based catalytic activity of supported WO_x domains is a function of the surface W density, reaching a maximum at a monolayer coverage of surface polytungstates. Their value of monolayer surface W density (7-8 W nm^{-2}), however, is higher than what is generally agreed upon (4.5-5 W nm^{-2}) by most other authors.[5,6,10,22] It has also been suggested that protons may take different positions on the polytungstate domains, denoted as $H^{\delta+}(WO_3)_n^{\delta-}$ (titrated protons typically exist in a ratio < 0.1 to total W atoms).[13] More recent investigations indicated that Zr-WO_x mixed oxide clusters of $\sim$1 nm in size possess the most active Brønsted acid sites (BAS) of WO_x/ZrO_2 catalysts for both alkane hydroisomerization and alkanol dehydration. These observations, along with the interpretations and implications, have been well outlined and discussed.[11]

While tungstated catalysts expose multiple types of surface WO_x structures and acid sites (e.g., W-OH, $H^{\delta+}(WO_3)_n^{\delta-}$), immersing such catalysts in water results in the deprotonation of Brønsted acid sites, forming hydrated hydronium ions ($H_3O^+(H_2O)_n$, abbreviated here as $(H_3O^+)_{hydr.}$).[22] An analogy is made here to our previous finding with H-MFI zeolites, for which the transformation of the Brønsted acid sites to hydrated hydronium ions in the presence of water has been demonstrated.[23]

Chemical transformations such as the formation of hydrated hydronium ions occur in the presence of water via an acid-base reaction, possibly accompanied by a redistribution of electrons and generation of a surface potential that manifests itself in surface charges, which become neutralized by ions of opposite charge in solution. The process leads to the formation of an electrical double layer (EDL) at the surface.[24] Transfer of protons to water (generating hydrated hydronium ions) leads to negatively charged oxide particles and a layer rich in $(H_3O^+)_{hydr.}$ at the WO_x domains (point of zero charge < 2 for pure WO_3[25,26]).

Our previous studies demonstrate that hydronium ions confined in molecularly sized pores of zeolites catalyze aqueous-phase cyclohexanol dehydration with turnover rates enhanced by up to two orders of magnitude compared to non-constrained hydronium ions in aqueous solutions.[22,27] Here, we investigate the catalytic activity of hydronium ions localized in the EDL of tungstated catalysts, which has been shown to be of excellent stability in the acidic aqueous phase.[18,28]

In this study, we use cyclohexanol dehydration as a probe reaction, aiming to examine the effects of WO_x domain size and support (ZrO_2, Al_2O_3, TiO_2 and activated carbon) on the turnover rates of hydronium ions that are primarily distributed near the surface of tungstate domains. As conventional characterization techniques for acid-base properties of these materials often yield results inconsistent with those measured in the presence of polar liquids such as water,[29] we developed a robust quantification method based on ion exchange for enumerating active sites at (or close-to-) reaction conditions in the aqueous phase. We show that not only the surface W densities, but also the nature of the underlying support affects the site-specific activity remarkably. The catalytic activity of WO_x domains supported on activated carbon even rivaled the activity of the most active zeolites for this reaction.

3.3) Results and Discussion

3.3.1) Aqueous-phase cyclohexanol dehydration over WO_x/ZrO_2

WO_x/ZrO_2 catalysts were prepared in different ways. The first set of catalysts (entries 1-4 of Table 1) was obtained by thermally treating a commercial $W/Zr(OH)_4$ sample with a constant WO_3 loading (15.5 wt.%) at different temperatures (973-1173 K), while for the second series, a commercial $Zr(OH)_4$ sample was impregnated with 3-37 wt.% WO_x (weight percentage calculated in the form of WO_3) and calcined at 973 K (entries 5-8 of Table 1). In the first series, the measured W surface density increased from 4.1 to 20.4 W nm^{-2}, with the concomitant decrease in surface area caused by the increasing calcination temperature; in the second series, the W surface density increased continuously from 1.2 to 19.5 W nm^{-2} (the BET surface areas first increased and then decreased as the W loading increased).

Based on the well-established relationship between the W surface density and surface structures of WO_x domains,[20,21,30,31] our samples with intermediate W surface densities of 4-6 W nm^{-2} are expected to exhibit approximately monolayer coverages of two-dimensional WO_x domains (i.e., polytungstate species) on the surface of ZrO_2. In line with this expectation, these samples do not show pronounced peaks of WO_3 crystallites in their XRD patterns (S-Figure 3.3).

A more detailed compilation of characterization results is presented in the Supporting Information (S-Figure 3.3-10 and S-Table 3.3). The physicochemical properties of tungstated zirconia materials have been extensively investigated in the literature and our findings here are in general agreement with previous studies.[1,12,13,20,21,32] The surface W densities of WO_x/ZrO_2 samples studied in this work correspond to a full span of WO_x-domain structures, ranging from isolated monotungstates and two-dimensional polytungstates to three-dimensional crystalline WO_3 nanoparticles.[5] In addition, subnanometric WO_x clusters incorporating some zirconium cations are also expected to exist in samples prepared by impregnation of W precursor onto amorphous $Zr(OH)_4$ support.[5,10] Wachs et al. argued that it should be easier to extract and incorporate zirconium cations from the metastable $ZrO_x(OH)_{4-2x}$ phase than a stable pre-formed ZrO_2 crystallite during calcination. Thus, as a comparison, two additional catalysts were prepared by first calcining the same commercial $Zr(OH)_4$ sample at 973 K to convert it into crystalline ZrO_2 and then applying the same impregnation and thermal treatments used for the second series (entries 9-10 of Table 3.1).

Table 3.1 | *General properties of the investigated tungstate catalysts*

Entry	Catalyst	WO_3 loading wt.%	BET surface area $m^2\ g^{-1}$	W-surface density $W\ nm^{-2}$
1	$WO_x/ZrO_{2,MEL,973}$	16	80	4.1
2	$WO_x/ZrO_{2,MEL,1023}$	16	75	4.7
3	$WO_x/ZrO_{2,MEL,1073}$	16	57	5.6
4	$WO_x/ZrO_{2,MEL,1173}$	16	19	20.4
5	(3)WO_x/ZrO_2	3	71	1.2
6	(18)WO_x/ZrO_2	18	106	4.6
7	(24)WO_x/ZrO_2	24	94	6.7
8	(37)WO_x/ZrO_2	37	50	19.5
9	(18)WO_x/pre-formed ZrO_2	18	33	14.2
10	(30)WO_x/pre-formed ZrO_2	30	17	46.0
11	(7)WO_x/C	7	1001	0.2
12	(18)WO_x/C	18	888	0.5
13	(27)WO_x/C	27	765	0.9
14	(37)WO_x/C	37	670	1.4
15	(41)WO_x/C	41	619	1.7
16	(54)WO_x/C	54	479	2.9
17	(15)$WO_x/\gamma\text{-}Al_2O_3$	15	177	2.2
18	(20)$WO_x/\gamma\text{-}Al_2O_3$	20	152	2.9
19	(24)$WO_x/\gamma\text{-}Al_2O_3$	24	136	4.7
20	(32)$WO_x/\gamma\text{-}Al_2O_3$	32	129	6.5
21	(50)$WO_x/\gamma\text{-}Al_2O_3$	50	80	16.1
22	(2)WO_x/TiO_2	2	10	5.2
23	(5)WO_x/TiO_2	5	12	11.0
24	(15)WO_x/TiO_2	15	12	32.5

The BAS of WO_x/ZrO_2 materials are almost exclusively associated with W-OH (in W-O-W and W-O-Zr structures) and protons delocalized over extended domains of polytungstates and WO_3 crystallites (through formation of $H^{\delta+}(WO_3)_n^{\delta-}$ via the local reduction of polytungstate domains). In the aqueous phase, these BAS become hydrated hydronium ions; the vast majority of these $(H_3O^+)_{hydr.}$ are spatially distributed in the EDL (comprised of an immobile Stern layer and a diffuse layer, with typical thickness of a few nanometers),[33] while only a minor fraction diffuses into the bulk solution (<10%) according to static pH measurements. It should be noted that the negative charge of the $(WO_3)_n^{\delta-}$ domains stabilizes the $(H_3O^+)_{hydr.}$ close to the surface, but that the repulsion between $(H_3O^+)_{hydr.}$ will lead to a fairly well averaged distance between them.

The total BAS concentrations on all the WO_x/ZrO_2 samples (in the aqueous phase), determined by the Li^+-ion-exchange method (Experimental), are presented in Table 3.2 (entries 1-10). The maximum BAS concentration appears at ~5 W nm^{-2}, i.e., corresponding to a monolayer coverage of WO_x-species. Concurrently, the mass-specific olefin formation rates reached their maxima at such surface W densities. The presence of optimal W surface densities for maximum rates is well documented for BAS-catalyzed o-xylene isomerization and 2-butanol dehydration on tungsten oxide catalysts (WO_x/ZrO_2 and WO_x/Al_2O_3).[5,12,15,19,20,34] Such observations are often associated with the structural evolution of supported WO_x domains from isolated monotungstates at submonolayer coverages to surface polytungstates at intermediate W densities and to WO_3-crystallites at even higher loadings. Our data in this study are in line with those of Wachs et al.[5,6,10] and Thomas et al.,[22] who reported the monolayer coverage to be achieved at 4.5-5 W nm^{-2}.

It should be noted in passing that the BAS counts, determined by aqueous phase Li^+ ion-exchange, represent more accurate estimates for the active sites than those given by ex-situ measurements in the gas phase or vacuum. The BAS per W-atom increased from 0.025 to 0.19 as the surface W density increased to a point when monolayer coverage was reached, beyond which point not all W atoms would be exposed. For gas-phase studies on similar tungstated zirconia catalysts, the H^+/W. ratio was found to be much smaller (< 0.04) at similar W densities,[12] suggesting that in the presence of water, the reducibility of WO_x domains and their ability to delocalize charges is enhanced and/or that some Lewis acid sites are converted into BAS. We hypothesize that the latter contribution to the higher BAS concentration, requiring water dissociation on Lewis acid sites, is minor, because water preferably adsorbs on WO_3 domains in an undissociated form.[35,36] The increase in BAS concentrations was fourfold higher than the decrease of the LAS concentration prior to exposure to water for tungsten oxide-based catalysts[37] or after immersing such catalysts in the aqueous phase.[38]

Table 3.2. Active site concentrations and various activity metrics of tungstated catalysts (473 K, 0.33 M cyclohexanol)

Entry	Catalyst	BAS	Mass-specific rate	TOF
		$\mu mol_{H^+}\ g_{cat}^{-1}$ ($H^+\ nm^{-2}$)	$\mu mol\ s^{-1}\ g_{cat}^{-1}$	s^{-1}
1	$WO_x/ZrO_{2,MEL,973}$	47 (0.35)	4.3	9.1×10^{-2}
2	$WO_x/ZrO_{2,MEL,1023}$	85 (0.68)	8.0	9.5×10^{-2}
3	$WO_x/ZrO_{2,MEL,1073}$	61 (0.64)	4.9	8.1×10^{-2}
4	$WO_x/ZrO_{2,MEL,1173}$	36 (1.1)	2.7	7.4×10^{-2}
5	(3)WO_x/ZrO_2	4 (0.03)	0.06	1.7×10^{-2}
6	(18)WO_x/ZrO_2	159 (0.90)	13.8	8.7×10^{-2}
7	(24)WO_x/ZrO_2	123 (0.79)	10.8	8.8×10^{-2}
8	(37)WO_x/ZrO_2	71 (0.85)	6.0	8.4×10^{-2}
9	(18)WO_x/pre-formed ZrO_2	40 (0.73)	2.0	5.0×10^{-2}
10	(30)WO_x/pre-formed ZrO_2	15 (0.53)	0.7	4.7×10^{-2}
11	(7)WO_x/C	79 (0.05)	6.2	7.8×10^{-2}
12	(18)WO_x/C	79 (0.05)	25.8	3.3×10^{-1}
13	(27)WO_x/C	71 (0.06)	24.9	3.5×10^{-1}
14	(37)WO_x/C	92 (0.08)	30.0	3.3×10^{-1}
15	(41)WO_x/C	70 (0.07)	23.7	3.4×10^{-1}
16	(15)$WO_x/\gamma\text{-}Al_2O_3$	15 (0.05)	0.1	5.3×10^{-3}
17	(20)$WO_x/\gamma\text{-}Al_2O_3$	92 (0.36)	1.4	1.5×10^{-2}
18	(24)$WO_x/\gamma\text{-}Al_2O_3$	96 (0.41)	1.8	1.8×10^{-2}
19	(32)$WO_x/\gamma\text{-}Al_2O_3$	140 (0.65)	3.6	2.6×10^{-2}
20	(50)$WO_x/\gamma\text{-}Al_2O_3$	153 (1.1)	4.9	3.2×10^{-2}
21	(2)WO_x/TiO_2	5 (0.03)	0.2	3.6×10^{-2}
22	(5)WO_x/TiO_2	14 (0.70)	2.0	1.5×10^{-1}
23	(15)WO_x/TiO_2	23 (1.1)	3.1	1.4×10^{-1}

To properly account for variations in the concentration of accessible W atoms and the associated acid sites, while varying the surface W-densities, TOFs were obtained by normalizing the measured mass-specific rate against the total BAS concentration. Although a bare ZrO_2 surface also has BAS, these sites are virtually inactive for dehydration (S-Table 3.2). For samples containing WO_x at, close to, or exceeding their monolayer coverages, it may be reasonably assumed that ZrO_2 surfaces are almost fully covered and, thus, BAS (13 μmol g_{cat}^{-1}; S-Table 3.2) on ZrO_2 do not contribute to the total BAS counts. The full coverage is corroborated by the absence of carbonate formation typically observed with ZrO_2 surfaces exposed to CO_2 (S-Figure 3.11 and 3.12). For other samples that expose ZrO_2 surfaces to varying extents, our TOF estimates based on total BAS counts might somewhat underestimate the site-specific activity of BAS associated with WO_x domains. For WO_x/ZrO_2 catalysts derived from W/Zr(OH)$_4$ (entries 1-8 of Table 3.2), the TOF showed a continuous increase with increasing W surface densities up to ~4.5 W nm^{-2}, beyond which the TOFs stayed constant. The TOFs at the plateau (Figure 3.1) are ~50% higher compared to that of homogeneous acids at the same conditions (i.e., (5-6)×10^{-2} s^{-1} at 473 K and 0.33 M cyclohexanol),[22] suggesting a higher catalytic activity of hydronium ions localized near the polytungstate domains supported on ZrO_2. It is noteworthy that the WO_x/ZrO_2 catalysts prepared by using crystalline ZrO_2 as the support displayed a somewhat lower TOF than the other WO_x/ZrO_2 catalysts derived from amorphous W-impregnated Zr(OH)$_4$ precursors (Table 3.2). These findings motivated us to explore the impact of the underlying support for these tungstate domains, with the surrounding EDL hosting the hydronium ions.

3.3.2) Support effects in aqueous alcohol dehydration on supported tungsten oxides

Surface densities of W on γ-Al_2O_3, TiO_2 and activated carbon were varied by changing the W loading, which also induced concomitant changes in specific surface areas (entries 11-24 of Table 3.1). The way surface WO_x structures vary as a function of the areal W density depended on the nature of the support, as shown by comparison of Raman spectra and XRD patterns of all tungstated catalysts (S-Figures 3.3-10). The structural aspects of supported tungstate domains have been discussed in great detail.[6,39,40] Compared to oxide supports, activated carbon appears to be less prone to dispersing WO_x domains, thus, favoring the formation of large WO_x crystallites at much lower W surface densities than on oxides (S-Figure 3.6). With activated carbon, however, tungstates did not reach the theoretical monolayer coverage in the range of W loadings studied here.

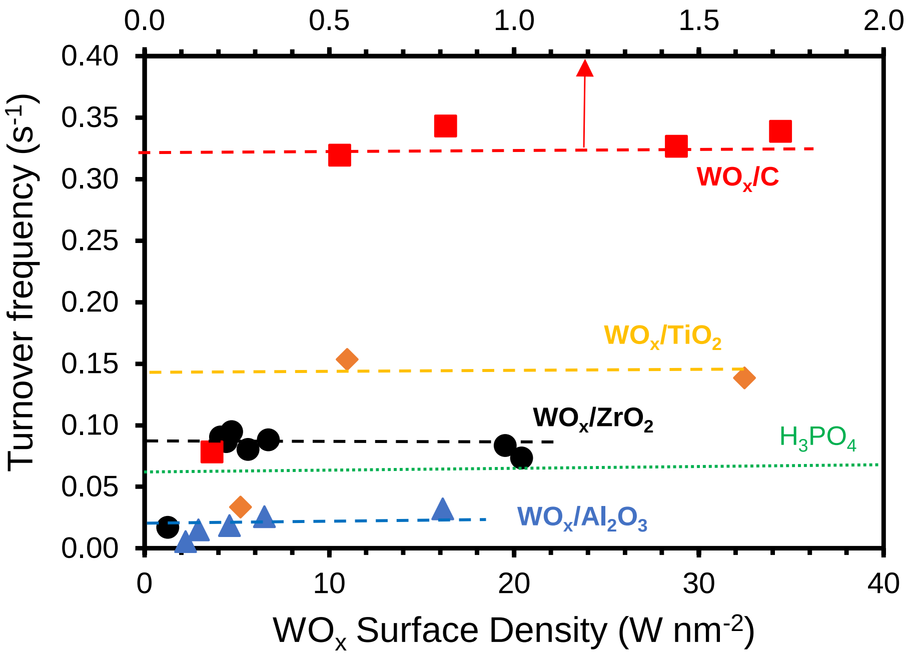

Figure 3.1. Turnover frequencies (rates normalized to the concentration of exchangeable protons on solid surfaces) as a function of WO_x-surface density on different tungstated catalysts (reaction conditions: 473 K, 0.33 M cyclohexanol). The TOF with a homogeneous acid (H_3PO_4), normalized to the dissociated hydronium ion concentration in water at reaction temperature, is shown for comparison (dotted line). Dashed lines serve as guide for eyes, indicating the level of TOFs at the plateau region. The WO_x/ZrO_2 catalysts derived from $W/Zr(OH)_4$ are plotted with the same symbol (black filled circles). Note the much smaller x-axis scale (0-2 W nm^{-2}) for the plotted data of WO_x/C series, for which the synthesized catalysts with higher WO_x loadings were not stable and, therefore, the TOFs at higher WO_x surface densities were not measured.

As with WO_x/ZrO_2 (Section 3.1), TOFs of all tungstated catalysts increased dramatically with W surface densities, but leveled off after reaching a certain threshold value of surface W density (Table 3.2 and Figure 3.1). This threshold coincided with the surface W density (~5 W nm^{-2}) at monolayer coverage for WO_x/ZrO_2 and WO_x/Al_2O_3 catalysts but did not quite match that value for WO_x/TiO_2 catalysts. The plateau was reached at a much smaller surface W density for tungstate supported on activated carbon than on other oxide supports (Figure 3.1). Interestingly, the plateau TOFs differ among catalysts (WO_x/C > WO_x/TiO_2 > WO_x/ZrO_2 > homogeneous acids > WO_x/Al_2O_3), unlike that reported for gas-phase 2-butanol dehydration, for which TOFs were unaffected by the identity of the support (SiO_2, Al_2O_3, ZrO_2 and SnO_2).[13] In another report on gas-phase methanol dehydration catalyzed by supported tungstate catalysts, a substantial support dependence was also observed, but the highest activity (W-based) was observed on WO_x/Al_2O_3.[42] Remarkably, the TOF of EDL-confined hydronium ions on WO_x/C is an order of magnitude higher than that on WO_x/Al_2O_3 and even comes close to that of the most active zeolite catalysts (that work in zero-order kinetic regime) previously discovered for this reaction.[22] Note that γ-Al_2O_3 is converted into a hydrated boehmite (AlOOH) phase in hot liquid water without having an appreciable impact on rate measurements (i.e., the conversion increased linearly with time).

A similar magnitude of support effect was observed for the aqueous-phase dehydration of several other substituted cyclohexanols, showing the generality of this marked support dependence of catalytic activity of the $(H_3O^+)_{hydr.}$ in the EDL (S-Table 3.4).

3.3.3) Mechanism and kinetics of cyclohexanol dehydration on tungstate domains

Before analyzing the observed rate dependence on the nature of support for WO_x domains, we establish below that the mechanism of alcohol dehydration is identical for the investigated catalysts. The reaction sequence for the hydronium-ion-catalyzed alcohol dehydration in the aqueous phase was shown previously to consist of alcohol adsorption and association with hydronium ions, protonation of the alcohol, and stepwise or concerted C-O and C-H bond cleavage along E1- or E2-type paths.[22,27] Our previous studies showed that in general an E1-like mechanism dominates for cyclohexanol dehydration with zeolites and aqueous inorganic acid catalysts, but that alcohol dehydration may occur via an E2-like mechanism for some substrates, such as cis-2-methylcyclohexanol.[41]

To identify the kinetically relevant step, the H/D kinetic isotope effect (KIE) was determined by comparing dehydration rates of $C_6H_{11}OH$ and $C_6D_{11}OD$ (Table 3.3). KIEs of ~3 measured (at 473 K) on representative tungstate-based catalysts, including materials in sub-monolayer regime and catalysts exceeding the theoretical monolayer coverage, clearly indicate that C-H(D) bond cleavage is involved in the kinetically relevant step.

Table 3.3 | H/D isotope effects measured for cyclohexanol dehydration in aqueous phase (473 K, concentration of cyclohexanol shown in brackets). In the first-order regime, measured KIE values are not affected by the alcohol concentration.

Reactant	Formation rate of olefin (μmol g^{-1} s^{-1})					
	(15)WO_x/ Al_2O_3	(32)WO_x/ Al_2O_3	(18)WO_x/ ZrO_2	(5)WO_x/TiO_2	(18)WO_x/C	(37)WO_x/C
$C_6H_{11}OH$	0.027 (0.11 M)	1.7 (0.22 M)	8.4 (0.22 M)	0.6 (0.11 M)	5.8 (0.11 M)	14.4 (0.11 M)
$C_6D_{11}OD$	0.010 (0.11 M)	0.5 (0.22 M)	2.9 (0.22 M)	0.2 (0.11 M)	1.9 (0.11 M)	5.0 (0.11 M)
KIE	2.7	3.1	2.9	3.3	3.1	2.9

The observed large positive activation entropies are shown later to be much less compatible with a typical E2 mechanism having an ordered transition state in which C-O and C-H bonds are concertedly broken. Therefore, we conclude that an E1-type mechanism is also the dominant path with the C-H bond cleavage (deprotonation of a carbenium ion-like intermediate) as the step with the largest degree of rate control for the present set of catalysts.

Under the measurement conditions, the dehydration rates on representative tungstated catalysts were determined to be first order with respect to the alcohol concentration (S-Figure 3.13), indicating low coverages of the reactive intermediates derived from cyclohexanol (i.e., a small fraction of hydronium ions being associated with cyclohexanol). The first-order rate expression can be written as:

$$TOF = k_{eff} K_{ads} a_{ROH} \qquad (3.1)$$

where K_{ads} is the equilibrium constant for the adsorption of alcohol in the EDL, which includes the association of alcohol with the hydronium ions in the EDL volume, a_{ROH} is the thermodynamic activity of the alcohol, and k_{eff} is a product of several corresponding kinetic and thermodynamic constants for the protonation of alcohol, C-O bond cleavage and C-H bond cleavage steps, as shown previously.[22,27] Thus, within the mechanistic framework described above, the effective first-order rate constant ($k_{eff}K_{ads}$= TOF/a_{ROH}) reflects the standard free energy differences ($\Delta G^{\circ\ddagger}$, Table 3.4) between the highest-lying transition state (C-H cleavage TS with the organic moiety and H_2O loosely interacting with each other) and associated alcohol and hydronium ions in the EDL:

$$\Delta G^{\circ\ddagger}_{meas} = \Delta G^{\circ}_{TS_{C-H}{}^{+}\dots H_2O(EDL)} - \Delta G^{\circ}_{ROH(aq)} - \Delta G^{\circ}_{H^{+}(EDL)} \tag{3.2}$$

Measured first-order rate-constants at various temperatures (only for representative catalysts in their respective plateau regime in Figure 3.1) were used to determine $\Delta H^{\ddagger}$ and, in turn, $\Delta S^{\ddagger}$ (Table 3.4). These $\Delta H^{\ddagger}$ and $\Delta S^{\ddagger}$ values vary with the type of catalysts and are significantly different from those obtained for reactions catalyzed by soluble acids. This suggests that hydrated hydronium ions as active sites exist in an environment different from the bulk solution and that this environment is influenced by the material dispersing the WO_x structures.

Table 3.4. Activation parameters derived for first-order rate constants*

Catalyst	$\Delta H^{\circ\ddagger}$ (kJ mol^{-1})	$\Delta S^{\circ\ddagger}$ (J mol^{-1}K^{-1})	$\Delta G^{\circ\ddagger}_{473K}$ (kJ mol^{-1})
(15)WO_x/Al_2O_3	222 ± 7	195 ± 17	130 ± 3
(32)WO_x/Al_2O_3	210 ± 4	173 ± 18	128 ± 4
$WO_x/ZrO_{2,MEL,973}$	184 ± 10	131 ± 15	123 ± 2
(18)WO_x/ZrO_2	177 ± 9	114 ± 15	123 ± 3
(5)WO_x/TiO_2	192 ± 2	152 ± 5	121 ± 3
(37)WO_x/C	174 ± 2	119 ± 6	118 ± 2
Soluble acids	151 ± 4	55 ± 8	125 ± 1

*These parameters are determined for first-order rate constants, reflecting the enthalpic, entropic and free energy differences between the highest-lying transition state and the solution state. Standard enthalpies, entropies and free energies of activation (at 473 K) were derived from kinetic measurements using the transition state theory formalism. The error bars for $\Delta H^{\circ\ddagger}$ and $\Delta S^{\circ\ddagger}$ represent the 1-σ s.d.'s, while the error bar for $\Delta G^{\circ\ddagger}$ represents the maximum error rounded up to the nearest integer.

On the other hand, changing the areal concentration of W and BAS for a given support leads to rather minor variations in the activation enthalpies and entropies, indicating that the concentration of sites varied, but not their nature. The lowest TOFs and first-order rate constants (at the plateau regime in Figure 3.1) measured for WO_x/Al_2O_3 are caused by the highest enthalpic barrier, which is offset to a great extent by the largest entropy gain. In fact, hydronium ions near surfaces of ZrO_2 and carbon-supported WO_x catalysts are more active than those in homogeneous solutions, because the associated activation entropies are significantly higher. In all cases studied, the positive transition entropies show that the elimination follows an E1 mechanism.

With hydronium ions in the aqueous phase, the reaction takes place with a substantially lower enthalpic barrier and a much smaller entropy gain than those measured for the WO_x-based catalysts (Table 3.4). The progress of the C-H bond cleavage should be similar for the homogeneous-acid-catalyzed dehydration, as inferred from the identical KIE[22,27] to those reported in Table 3.3. Thus, the entropy gain is concluded to arise, in part, from the translational and rotational degrees of freedom for water released upon the almost complete C-O bond scission. Additional entropy changes (either gains or losses) may be acquired primarily via configurational rearrangements within the extended water network that solvates the kinetically relevant TS and the initial state with different abilities to engage in H-bonding. More hydrogen bonds being disrupted in attaining the TS typically leads to a greater entropy gain and a higher enthalpic barrier.[42,43] Thus, it appears that the disruption of hydrogen bonds is more extensive in attaining the same kinetically relevant C-H bond cleavage TS in the EDL near surfaces of tungstated catalysts than in the bulk aqueous solution. We attribute this to the stronger bonding of the hydronium ion near the surface and the concomitant higher entropy gain of water formed past the protonation steps.

3.3.4) Origins of aqueous phase support-dependent activities

The TOFs and the activation parameters for aqueous-phase cyclohexanol dehydration vary drastically with the nature of the support. Conceptually, the differences in the TOFs and activation parameters may be caused by: (1) different nature of the rate-determining step (RDS) or differences in the extent of bond breaking/making; (2) different thermodynamics of the adsorption of cyclohexanol, K_{ads}, and the ensuing quasi-equilibrated steps (e.g., protonation of alcohol) preceding the RDS; (3) different intrinsic rate constants for the RDS, k_{int} (variations in enthalpy and entropy of activation).

As the measured KIEs were identical among catalysts (~3; Table 3.3), the progress of C-H_β bond cleavage at the kinetically relevant TS is inferred to be similar across different catalysts and can be characterized as being “late” (i.e., C-H_β bond almost fully broken) along the reaction coordinate.[22] Thus, differences in the progress of C-H_β bond breaking at the TS are concluded to be unlikely and not the reason for differences in the activation parameters and rates (Figure 3.1 and Table 3.4).

In the first-order regime and with the RDS being the C-H_β bond scission, the adsorption (including association with the hydronium ion), protonation and the C-O bond cleavage steps that precede the RDS can be treated as a lumped, quasi-equilibrated step ($K_{lump} = K_{C\text{-}O}K_{prot}K_{ads}$). The measured first-order rate constant, k_{meas}, is the product of k_{int} and K_{lump}. Although a higher k_{meas} (and a correspondingly lower $\Delta G^{\circ\ddagger}_{meas}$) must be caused by a better stabilization of the transition state or a destabilization of hydronium ions in the EDL (in the 1st order regime, the alcohol reactant being in the liquid phase makes its energy level irrelevant), it is impossible to assess in this kinetic regime, which of the two constants, k_{int} and K_{lump}, is the main contributor to k_{meas}. The adsorption constant K_{ads} is comparable across different tungstated catalysts according to independent measurements (S-Figure 3.15), leading us to conclude that any difference in the adsorption strength is not responsible for the pronounced TOF variations as the support identity varies (Figure 3.1).

Now the question arises, why the C-H cleavage TS is more stabilized (relative to the hydronium ions) on WO_x/C than on oxide-supported tungstate domains and in an aqueous acidic solution (in enthalpic and free energy terms; see Table 3.4). To answer this question, let us reiterate that hydronium ions are distributed primarily in the EDL with a ratio of water to H^+ ranging from 6 to 18 when adsorbed from the gas phase close to the water saturation/condensation pressure. This is in the range for which water is still considered to be in the hydration shell of the hydronium ion. This may have two consequences. On one hand, the acid strength of hydronium ions varies subtly with the size of the hydration shell.[27] On the other hand, the size of the hydronium ion may influence the distance between them changing the impact on the sorbed molecules[44,45], i.e., it influences the excess chemical potential of the sorbed molecules and all intermediates and transition states along the reaction coordinate.

Our recent work indicated that a “local ionic strength” in zeolite pores has a great impact on the excess chemical potential (considered in the activity coefficient) of the adsorbed species.[45] Thus, we hypothesize that the density of the hydronium ions in the EDL on the WO_x domains also induces a local ionic environment and controls the excess chemical potentials of the substrates along the reaction pathway. We also hypothesize that the potential size of the hydronium ion plays a minor role, as most changes in the acid strength have been found for hydrated hydronium clusters with only a few water molecules associated.[23,46,47] The nature of the support influences the concentration of surface protons (BAS concentration in Table 3.2) and the volume of the EDL that is primarily comprised of water molecules, and few alcohol molecules (first-order kinetic regime).

Hence, gas-phase water uptake measurements are used here to provide relative magnitudes of the EDL volume surrounding the WO_x domains for different catalysts, though we must keep in mind that such measurements are not meant to quantitatively represent the EDL volume at reaction conditions. S-Figure 3.16 shows the isotherms measured at 313 K of water adsorption on different catalysts and column 2 of S-Table 3.5 reports the water uptake extrapolated to 70 mbar (saturation vapor pressure)[48] and 313 K. Extrapolation to other equilibrium pressures along the isotherm would not change the qualitative trend discussed next. Column 4 of S-Table 3.5 is the estimate of the ionic strength that would exist if the number of hydronium ions on each support, measured (473 K, 40 bar N_2) as shown in Scheme 3.1 and described in the associated text, were placed in the water layer (approximating an EDL as estimated at 313 K).

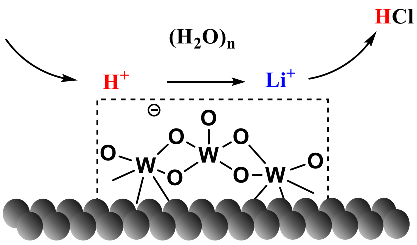

Scheme 3.1. Determination of Brønsted acid site concentration on tungstate surfaces using ion exchange of a Brønsted acid site with excess LiCl solution.

Given that the accessible support surfaces on supported tungstate catalysts (WO_x/ZrO_2, WO_x/Al_2O_3 and WO_x/TiO_2) become minimal after exceeding monolayer coverage of the tungstate domains (S-Figures 3.11 and 3.12), the water uptakes on these materials can be directly related to those adsorbed on WO_x domains only. In contrast, for WO_x/C, where the WO_x-coverage was much lower than a monolayer, the surface of activated carbon, on which water adsorption can also occur (on the polar surface functional groups), must be considered. Consequently, the water uptake on WO_x/C was corrected for the adsorption on bare carbon support to obtain the fraction of water adsorbed on WO_x domains only.

Figure 3.2A illustrates that the TOFs of representative catalysts increase with the concentration of hydronium ions in the EDL. WO_x/C catalysts had a more than 10-fold higher activity than WO_x/Al_2O_3 catalysts, owing to the much higher concentration of hydronium ions in the EDL. This trend is qualitatively similar to that observed for HCl-catalyzed dehydration of cyclohexanol in water, where an increasing ionic strength (induced by increasing LiCl concentration from 0 to ~5 M) enhanced the TOF by nearly

20-fold (S-Figure 3.2). For a reaction that develops positive charges in the transition state, this observation would be expected as a consequence of ionic strength effects (i.e., Brønsted-Bjerrum-Debye theory).

Conceptually, a higher concentration of hydronium ions in the EDL leads to a closer spacing, which is ultimately limited by the repulsive electrostatic forces between EDL-constrained hydronium ions and the negatively charged WO_3 surfaces. Applying a purely geometric model (Figure 3.2, upper panel), we then estimated the average distance (d_{H+}) between neighboring hydronium ions; the details of the estimation method are described in the SI, S-Note 3.1. Here, a uniform spacing was assumed for the hydronium ions distributed over the EDL surrounding WO_x-domains. As expected, the decrease of d_{H+} was found to correlate well with an exponential increase of TOF (Figure 3.2B), reflecting the substantial rate enhancement of the acid-catalyzed dehydration in a dielectric environment populated with hydronium ions as the average spacing (d_{H+}) decreases, or as the local ionic strength increases.

To address the temperature difference of the water adsorption measurement and the reaction conditions (TOFs at 473 K are associated with ionic strength in the EDL estimated from water adsorption at 313 K, see S-Table 3.5 and associated text for details), we draw attention to the fact that specific interactions with the tungstate surface that may affect the EDL volume are chemical/structural properties of the surface and, therefore, likely to be somewhat temperature independent after accounting for the change in pH with temperature (S-Note 3.2). For a demonstration of this, Fokkink et al. reported for TiO_2 (and this is expected to apply to other simple oxides) that at a constant electrolyte concentration, after temperature correction of the pH, the charge density on the surface vs. pH was independent of temperature.[49] By inference, it would be reasonable to assume for the present study that the actual EDL dimension and the ionic strength remain constant over the temperature range 313-473 K.

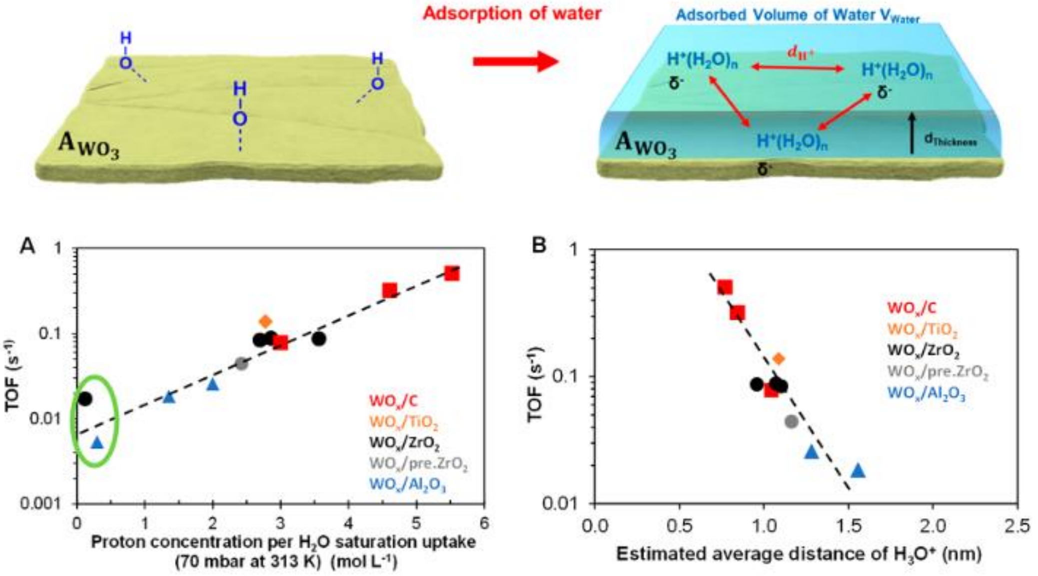

Figure 3.2. *Graphical model (upper panel) of the gas-phase water uptake measurements. V_{Water} is defined as the adsorbed water on WO_x-domain only (corrected for adsorption on support material in the case of carbon), $d_{Thickness}$ is the multiplication of the kinetic diameter of H_2O (0.265 nm)[50] and the number of water-layers on the WO_x-surface and d_{H^+} is the average distance of hydronium ions on the tungsten oxide surface (A_{WO_3}). Lower panel:* ***A:*** *Turnover frequencies (TOFs) of aqueous-phase cyclohexanol dehydration (473 K, 0.33 M cyclohexanol) on different tungstated catalysts as a function of approximated "hydronium ion concentration" based on H^+ counts constrained in V_{Water};* ***B:*** *TOF as a function of the average distance of hydronium ions (d_{H^+}), calculated from q. S-2.1 and 2 (see SI) using an estimated layer thickness of 0.49 nm (S-Figure 3.17, SI) on the WO_x-domain for catalysts with monolayer or supramonolayer W-coverages (the calculated average distance of hydronium ions appears to be artificially larger for WO_x/Al_2O_3 and WO_x/ZrO_2 samples with submonolayer coverages, due to non-corrected adsorption of water on oxide supports; for this reason, the two lowest points in panel A are not plotted in panel B). Dashed lines represent trends.*

As the reaction is first order in the alcohol, the reference state for the kinetics is cyclohexanol in the bulk solution phase, essentially unaffected by the "ion concentration" in the EDL. However, both the ground state and the C-H cleavage transition state are located in the EDL at the WO_3 surface and, thus, influenced by the ionic strength. While we cannot exclude an impact on the (excess) chemical potential of hydronium ions, we conclude that the TOF is directly related to the ionic strength in the EDL (and inversely proportional to the average distance of the hydronium ions) and, hence, controlled by the difference between the excess chemical potential of cyclohexanol in the liquid phase and the transition state of the C-H cleavage of the intermediately formed carbenium ion. Although the individual enthalpy and entropy components must both be affected by the local ionic strength, a detailed analysis remains challenging and beyond the scope of this work.

Summarizing, our analysis shows that the effect of the support identity on the TOF of alcohol dehydration in the aqueous phase is predominantly associated with the different extents of stabilization for the $C-H_\beta$ bond cleavage transition state in the presence of a variable ionic strength within the interfacial water layer. This local ionic strength, which is equivalent to the hydronium ion concentration in the interfacial layer, is hypothesized to account for the changes in energetics (free energy level of the rate-limiting TS) and the measured TOFs. The volume of the interfacial layer (EDL) and the number of hydronium ions distributed therein collectively determine the local ionic strength. The number density of hydronium ions is influenced by the nature of the support because the latter is known to affect the ability of the WOx domains to delocalize negative charges, the extent of which appears to be enhanced by the presence of water as shown in this work. The volume of the interfacial water layer is much less straightforward to determine, but gas-phase water uptake appears to serve as a reasonable approximation of the EDL volume surrounding the WOx domains for different catalysts.

3.3.5) Conclusion

Using a series of hydrothermally stable supported tungstate catalysts, we demonstrate that hydronium ions within the electrical double layer of these two-dimensional surfaces exhibit a marked dependence of TOF on the identity of the support for the aqueous-phase dehydration of cycloalkanols. This site-specific activity increases with the density of $(H_3O^+)_{hydr.}$ in the layer above the solid surface (EDL). The maximum TOFs rival the most active zeolite catalysts for the same reaction.

For oxide-supported tungstates, their ability to delocalize hydronium ions in the EDL varies with the dominant surface tungstate structures, with the maximum $(H_3O^+)_{hydr.}/W$ ratio appearing at monolayer coverage (~5 W nm^{-2}) where two-dimensional polytungstates prevail. For these catalysts, TOF is a steep function of surface W density up to monolayer coverage, but then becomes independent of the W-surface density and structural changes of tungstate. Differences in the TOFs and activation parameters are not caused by changes in the reaction mechanism or rate-determining step, as indicated by the same magnitude of primary deuterium isotope effects across the studied catalysts. Instead, the TOFs increase with the estimated hydronium ion concentrations in the EDL (with increasing proximity of hydronium ions localized in the EDL) over the negatively charged WO_x-domain. This reflects the impact of ionic strength, H-bonding and the associated variations in electrostatic forces on the stability of the positively charged deprotonation transition state in the EDL. These insights also extend our recent findings on the impact of non-ideal ionic environments in zeolite pores for hydronium ion-catalyzed alcohol dehydration.[53]

Our findings point to a new possibility of modulating the intrinsic activity of acid sites associated with WO_x domains in aqueous-phase acid catalysis, previously unexploitable in gas-phase scenarios of similar reactions catalyzed over these materials. The implications may be extended to a broad set of acidic oxide domains (VO_x, ReO_x, MoO_x, etc.) that host a high local concentration of $(H_3O^+)_{hydr.}$ in their near-surface regions.

3.3.6) Materials and Methods

Reagents used were follows: cyclohexanol (ReagentPlus®, 99%, Sigma-Aldrich); cyclohexanol-d_{12} ($\geq$ 98 atom% D, Sigma-Aldrich); ethyl acetate (ACS reagent, $\geq$99.5%, Sigma-Aldrich); sodium sulfate (Acros Organics, anhydrous, 99%); 2-cyclohexen-1-one ($\geq$95%, Sigma-Aldrich); doubly deionized water (resistivity of ~18 MΩ·cm); ammonium metatungstate hydrate (Sigma-Aldrich, 99.99% trace metals basis); lithium chloride (ACS reagent, $\geq$99%, Sigma-Aldrich, anhydrous, free-flowing).

Tungstated zirconium hydroxide (XZO1251/02) and zirconium hydroxide ($Zr(OH)_4$, batch number: PRB310) were obtained from MEL Chemicals. Other support materials for impregnation, including activated carbon (Darco®; KB-G, Sigma- Aldrich), titanium(IV) oxide (anatase; Sigma-Aldrich, 99.8% trace metals basis) and commercial boehmite (CATAPAL® B alumina, SASOL), were purchased from individual companies.

The first series of WO_x/ZrO_2 catalysts was obtained by thermally treating a commercial tungstated zirconium hydroxide sample (XZO1251/02, specification sheet in S-Table 3.1) in a static air muffle furnace at 973-1173 K for 4 h, resulting in materials with calculated surface densities of 3-20 W nm^{-2}; in this case, the increase in surface density is due to phase transformation from monoclinic to tetragonal zirconia and a consequent loss of surface area with increasing calcination temperature.[51] This series of WO_x/ZrO_2 is denoted with 'MEL' and the corresponding pretreatment temperature as subscripts; for example, $WO_x/ZrO_{2,MEL,973}$ stands for a commercially obtained catalyst calcined at 973 K.

The second series of WO_x/ZrO_2 catalysts was prepared by incipient wetness impregnation of as-received $Zr(OH)_4$ with aqueous solutions of ammonium metatungstate containing the desired amount of W. The samples were dried at 383 K for 12 h and calcined in flowing synthetic air (20 ml min^{-1} g^{-1}) for 4 h at 973 K. Nominal W loadings of 4-50 wt.% were achieved, corresponding to surface densities (SD_W) of 1-20 W nm^{-2}, calculated using an established correction method[5]:

$$SD_W = \frac{\frac{N_A \times \frac{\frac{wt\%W}{100}}{M_W}}{S.A. \times 10^{18}}}{1-\left(\frac{wt\%W}{100} \times \frac{M_{WO_3}}{M_W}\right)} \tag{3.3}$$

where M_{WO_3} and M_W are the molar mass of WO_3 (231.84 g mol^{-1}) and W (183.84 g mol^{-1}), N_A is the Avogadro's number (6.023×10^{23}), wt%W is the W loading (wt%) in the sample and S.A. is the Brunauer–Emmett–Teller (BET) surface area of the sample (m^2 g^{-1}), respectively. Two additional WO_x/ZrO_2 catalysts were prepared by first calcining the as-received $Zr(OH)_4$ at 973 K (in synthetic air flow, 20 ml min^{-1} g^{-1}) for 4 h to convert it to crystalline ZrO_2, which was then impregnated with aqueous solutions of ammonium metatungstate containing the desired amount of W, followed by the same thermal treatment at 973 K. These two samples are denoted as "(M)WO_x/pre-formed ZrO_2", where M refers to the nominal WO_3 loading.

WO_x/C, WO_x/γ-Al_2O_3 and WO_x/TiO_2 were prepared via the same protocols described above for incipient wetness impregnation and thermal treatments of the second series of WO_x/ZrO_2, using activated carbon, γ-Al_2O_3 and TiO_2 as support materials, respectively, except that N_2 was the atmosphere used in thermal treatments of carbon-supported materials. For WO_x/γ-Al_2O_3 catalysts, the γ-alumina support was obtained by treating boehmite for 7 h in static air at 973 K. These impregnated materials and the second series of tungstated zirconia are all denoted as "(M)WO_x/support", where M refers to the nominal WO_3 loading.

The elemental composition was determined by the Microanalytical Laboratory at TU München using acid digestion and subsequent photometric determination using a Shimadzu UV-160 photometer. Specific surface areas and pore volumes of the impregnated materials were determined by N_2 physisorption using a PMI Automatic Sorptometer. The isotherms were measured at 77 K, after activation in vacuum at 473 K.

Raman spectra were acquired on a Renishaw inViaTM Reflex Raman system, equipped with a Renishaw RL532C, Class 3B, 532 nm laser as excitation source. After calibration to a Si (111) crystal, the spectra were conducted with a 50-fold magnification in the range of 100-4000 cm^{-1} and 1-10 s of measurement time. At least 10 different positions were measured on each sample.

X-ray Diffraction (XRD) was performed on an instrument (Empyrean, PANalytical) equipped with a Cu X-ray tube (Cu-Kα radiation, 0.154 nm), a Ni Kβ-filter, and a solid-state detector (X'Celerator) operated at 45 kV and 40 mA with step size of 0.017° and scan time of 115 s per step. Reflection transmission mode from 5 to 70° (2θ) at ambient conditions was performed while samples were pressed on a silicon single crystal with a (111) surface.

Gas-phase calorimetric and gravimetric measurements were performed at 318 K on a Setaram TGA-DSC 111 microbalance attached to a UHV system. The catalyst powder was pressed into pellets, crushed and sieved to a 100-500 µm fraction and loaded in a crucible (10-20 mg). Prior to measurements, the sample was activated at 723 K for 1 h with a heating ramp of 10 K min^{-1} under high vacuum ($p < 10^{-4}$ mbar). Water vapor was introduced into the isothermal system in small pressure steps from 10^{-3} to 25 mbar, followed by adsorption equilibration. The weight increase and heat flux were monitored during pressure equilibration.

Liquid-phase adsorption was carried out immersing 50-200 mg of catalyst in several defined cyclohexanol solutions (3-74 mM) for at least 24 h under isothermal conditions.

The solid was separated from the solution and the residual concentration of cyclohexanol in the liquid was determined via GC-MS, after an extraction with ethyl acetate in which 2-cyclohexene-1-one was added as an internal standard.

The Fourier-transform infrared (IR) spectra of adsorbed carbon dioxide were recorded on a Perkin–Elmer 2000 spectrometer at a resolution of 4 cm^{-1} in transmission mode. The catalyst samples were prepared as self–supporting wafers and activated in vacuum ($p = 10^{-6}$ mbar) at 723 K for 1 h at a heating rate of 10 K min^{-1}. After cooling to 303 K, the sample was equilibrated with 0.5 mbar CO_2 for one hour followed by outgassing at 10^{-6} mbar for one hour and the acquisition of the spectrum. Finally, desorption program (up to 723 K with 10 K min^{-1} and 1 h at 723 K) was initiated and the spectra were recorded until equilibrium was achieved.

Aqueous-phase cyclohexanol dehydration was performed in a 100 ml Hastelloy Parr reactor. In a typical experiment, 33 mL of 0.33 M aqueous cyclohexanol solution and ~200 mg of the catalyst were loaded in the reactor. The reactor was sealed, and all oxygen was removed by flushing three times with 40 bar N_2, before pressurizing to a N_2-pressure of 40 bar at ambient temperature. The mixture was then heated to a defined temperature (T_R, e.g., 473 K). Agitation (700 rpm) was started when the temperature reached (T_R -10), to ensure a negligible conversion during heat-up. The reaction time (t_R) was recorded after reaching T_R (time zero). At the end of a reaction, the reactor was immediately cooled with an ice/water mixture to 277 K and lower. Reactants and products were extracted three times using 20 ml of ethyl acetate each time. A defined quantity of 2-cyclohexen-1-one was added in ethyl acetate as an internal standard. The organic phase, after being separated and dried over sodium sulfate, was analyzed on a Shimadzu 2010 GC equipped with an HP-5MS 25m×0.25 mm (i.d.) column and a flame ionization detector (FID). The carbon balance was found to be better than 95%. The selectivity towards the olefin (cyclohexene) was always larger than 99% (i.e., only traces of the ether product).

For all prepared catalysts, stability tests were performed at 473 K and 40 bar N_2 in stirred hot liquid water for at least 12 h. In a typical run, 0.1 g of catalyst and 100 mL of deionized water were charged into a 300 mL Hastelloy Parr reactor equipped with a 2 µm filter. After stirring (700 rpm) for 12 h, the hot suspension was drained and filtered from the reactor via a gate valve to ensure no back-precipitation of possibly dissolved tungstates if any. The filter cake was dried overnight at 373 K and analyzed for its elemental composition to examine whether there was any leaching of W (as bulk WO_3 is known to slowly dissolve in water, with the dissolution rate and the speciation of multiple co-existing W-anions controlled by solution pH). For none of the materials did we detect noticeable changes in the elemental compositions, indicative of negligibly slow dissolution of WO_3 domains in hot liquid water in the absence of externally added acids or bases. Additional tests of long-term hydrothermal stability required the monitoring of alcohol conversion as a function of time (> 20 h), that is to say, if W leaching occurred (forming tungstic acid in water via: $WO_3 + H_2O = WO_4^{2-} + 2H^+$) over an extended period of time, the conversion rate would change (as we show later that TOFs are significantly different for supported tungstates and homogeneous acidic species such as tungstic acid), which would be captured by a noticeable change in the slope of the conversion-time curve. These results are shown and discussed in the Supporting Information (S-Figure 3.1), based on which W leaching was fully excluded.

For the determination of BAS concentration at reaction conditions (473 K, 40 bar N_2), 300 mg catalyst was suspended in 100 mL of an aqueous cyclohexanol solution (0.11 M) and charged to a 300 ml Hastelloy Parr reactor. After removing air by flushing with N_2 for multiple times, the reactor was charged to 40 bar (N_2) and heated under an agitation speed of 500 rpm to 473 K. When reaching the target temperature, the reactor was immediately quenched by cooling the vessel in an ice-water bath, to ensure negligible conversion of the alcohol during cooling. This protocol ensured that possible reduction processes of the WO_x-domain by the alcohol (a potential reductant) that would form additional BAS at reaction conditions had taken place prior to reaction. These processes, if occurring, are considered to be fast and irreversible. The reactor was depressurized before adding lithium chloride (LiCl) to yield a final salt concentration of 1.6 M. The mixture was stirred at ambient conditions for at least 12 h to ensure complete proton exchange of all BAS (e.g., $W\text{-}OH + LiCl_{aq} \rightarrow W\text{-}OLi + HCl_{aq}$).

After separating solid and liquid, the ion-exchanged catalyst was dried and tested for alcohol dehydration reaction, which showed negligible conversion (< 1% conversion after 4 h, i.e., two to three orders of magnitude lower mass-specific activity than any of the tungstated catalysts) and thus indicated complete proton exchange with Li^+. This result also indicates that Lewis acid sites (that are not supposed to react away with LiCl), if still persisting in water, do not catalyze dehydration at detectable rates. The recovered liquid contained LiCl at approximately the same concentrations as the initial values, and it also contained a defined quantity of protons exchanged from the solid sample. Note that for high LiCl concentrations (1-5 M), a pH meter that measures the activity of hydronium ions in aqueous solution does not yield a reliable measure of the concentration of hydronium ions because of the ionic strength effects. Therefore, to quantify the concentration of hydronium ions, 33 mL of the recovered solution was added to the 100 mL Hastelloy Parr reactor and cyclohexanol (0.33 M) was added. Multiple reactions with HCl as a catalyst were conducted (conversion < 10%) to allow calculating rates of HCl-catalyzed cyclohexene formation, $r_{formation,HCl}$. As the solution contains LiCl at relatively high concentrations, the turnover frequency (TOF) was corrected for the ionic strength effects (S-Figure 3.2). In this way, the concentration of BAS (i.e., hydronium ions) in the post-exchange solution can be calculated according to Eq. 3.4:

$$[BAS]= \frac{r_{formation,\ HCl}}{TOF(I)} \qquad (3.4)$$

This [BAS] concentration in the post-exchange solution was then used to calculate the surface concentration of exchangeable protons on the solid sample, based on the volume of solution and mass of the solid sample. To quantify the amount of in-situ generated BAS, the protocol was repeated at room temperature without heating to 473 K prior to the addition of LiCl. Separate experiments with support materials alone show that hydroxyls (-OH) on Al_2O_3, TiO_2 and activated carbon do not contribute significantly to the BAS counts, while there is 13 μmol g_{cat}^{-1} of exchangeable BAS on bare ZrO_2 surfaces (S-Table 3.2).

3.4) Supporting Information

Impact of the local concentration of hydronium ions at tungstate surfaces for acid-catalyzed alcohol dehydration

Content:

Specification sheet for the commercial tungstated zirconium hydroxide sample (MEL Chemicals): S-Table 3.1

Supporting kinetic analysis: S-Table 3.2, 4; S-Figure 3.2, 13

Supporting characterization: S-Table 3.3, 5; S-Figure 3.3-10, 11, 12 ,14-16

Stability tests: S-Figure 3.1

Supporting concepts: Note 3.1, Note 3.2, S-Figure 3.17 and 18

***S-Table 3.1** Generic sample analysis sheet for the commercial tungstated zirconium hydroxide (product XZO 1251/02, batch PRB1034) provided by the company (MEL Chemicals). The company recommends the following activation procedures: this sample needs activating by calcining at 973-1073 K (preferably in static air) immediately before use; the optimum temperature will depend upon the acidity requirements of the reaction being catalyzed; preferably, cool in a P_2O_5 desiccator, or dry at 573 K for 1 h immediately before use.*

Analysis	Units	Result
LOI (@1000 °C)	%	26.5
WO_3/MO_x	%	15.5
SO_3	%	< 0.01
Na	ppm	10
Cl	ppm	40
Specific surface Area	m^2/g	260
Total Pore Volume	cm^3/g	0.33
Phase (by visual inspection of XRD)	Amorphous	
Particle Size (high ultrasonic 40w 60s)		
D10	µm	1.4
D50	µm	5.6
D90	µm	9.3
Aged surface area (after 750 °C for 2 h)	m^2/g	80
Aged total pore volume (after 750 °C for 2 h)	cm^3/g	0.22

S-Table 3.2 *General properties and mass-specific activities of bare supports, after thermal treatment at 973 K in synthetic air (for γ-Al_2O_3, ZrO_2 and TiO_2) or N_2 (for activated carbon). Activity measurements were carried out at standard conditions (473 K, 0.33 M cyclohexanol in water, ~0.2 g of catalyst)*

Entry	**Support**	**BET surface area**	**BAS**	**Mass-specific rate**
		$m^2\ g^{-1}$	$\mu mol\ g_{cat}^{-1}$	$\mu mol\ g_{cat}^{-1}\ s^{-1}$
1	γ-Al_2O_3	219	N.D.	~0
2	ZrO_2	112	13	~0
3	TiO_2	~20	N.D.	~0
4	activated carbon	1090	2	3

* N.D. (not detectable) is defined as a value smaller than 1 µmol g_{cat}^{-1}.

3.4.1) Stability tests

To maintain relatively low conversions for an accurate assessment of stability without the interference from reactant depletion effects on first-order kinetics, a much smaller mass of sample had to be employed. For example, a WO_x/C sample was chosen for the study of hydrothermal stability, since the presumably poor wetting of tungstate domains on carbon surfaces casts doubts on the stability of WO_x-domains in hot liquid water. S-Figure 3.1, however, illustrates that this representative carbon-supported catalyst maintained its activity (i.e., linear increase of conversion) over a period of more than 45 h, demonstrating its hydrothermal stability. Moreover, the obtained rate was close to the activity when applying the conditions described for the typical experiments, illustrating that variation of the catalyst mass loading has no effect on the mass-specific rates of the reaction. Oxide-supported tungstate catalysts also did not show any sign of W leaching based on the long-term activity tests (not shown). Thus, we conclude that our tungstated materials are hydrothermally stable catalysts for acid-catalyzed reactions and are also promising platforms for the assembly of bifunctional catalysts for hydrodeoxygenation reactions.

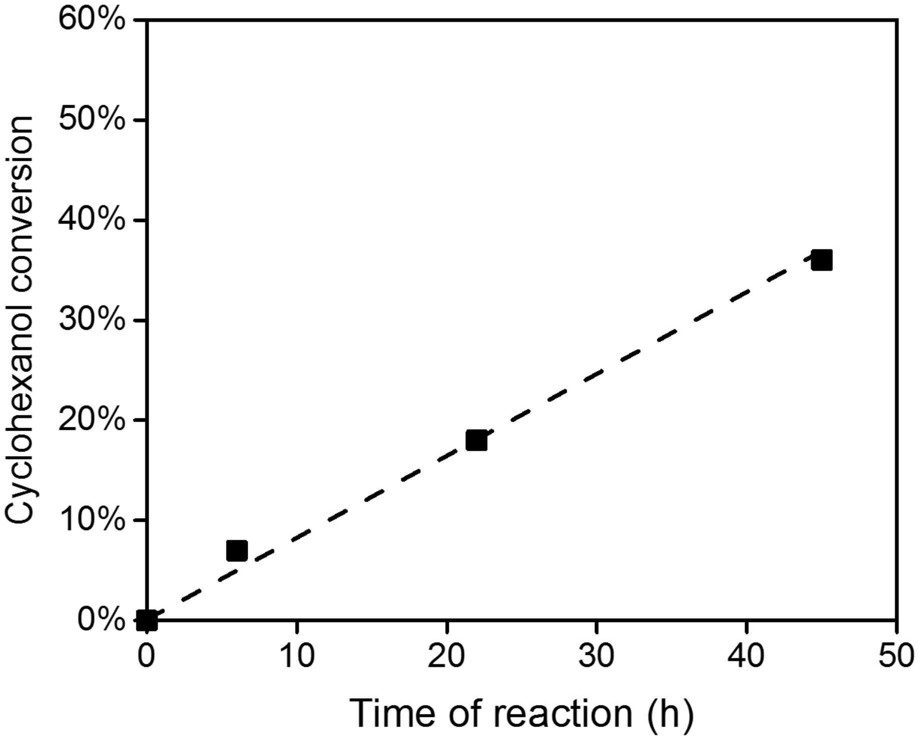

S-Figure 3.1 *Long-term hydrothermal stability test of a representative WO_x/C catalyst in a reaction at 443 K (intended for lower rates and longer reaction times) and 0.33 M cyclohexanol. The obtained rate over 45 h was 1.7 µmol* $(g_{cat}\ s)^{-1}$*, similar to 1.3 µmol* $(g_{cat}\ s)^{-1}$ *for initial rates with 211 mg catalyst and ~2 h reaction time. The linear increase over that long period of time and the obtained rate close to the initial rate demonstrates a good stability of this type of material for the reaction in water.*

3.4.2) BAS determination: calibration of ionic strength effects

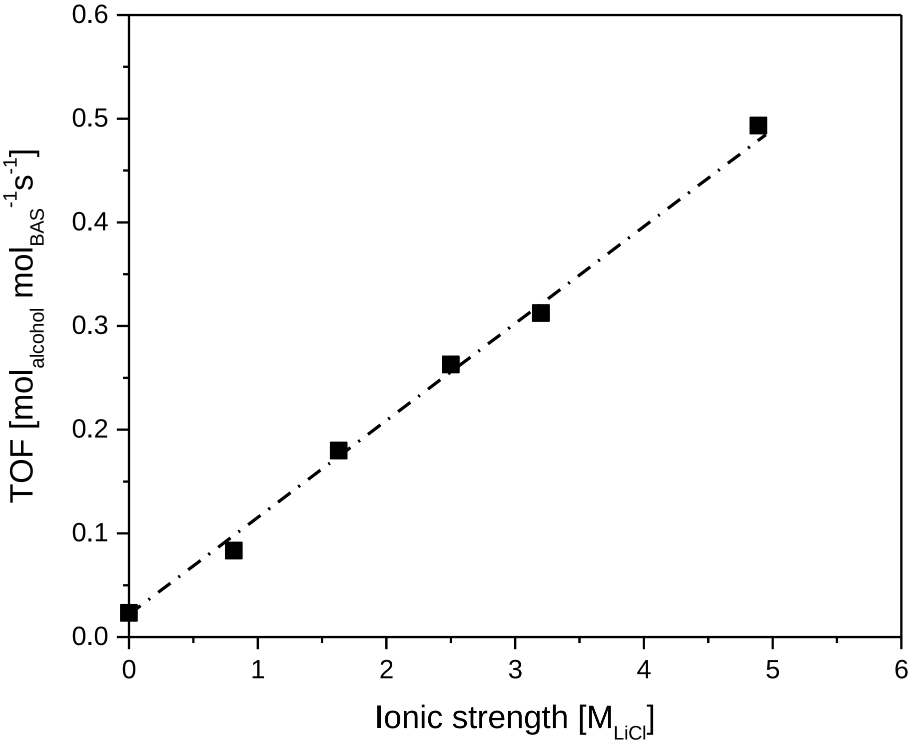

S-Figure 3.2 *Calibration of ionic strength effects on the dehydration activity (TOF per hydronium ion) with HCl solution containing LiCl at 0-5 M concentrations (473 K, 0.33 MCyOH, pH(HCl) = 3.2).*

3.4.3) X-ray diffraction

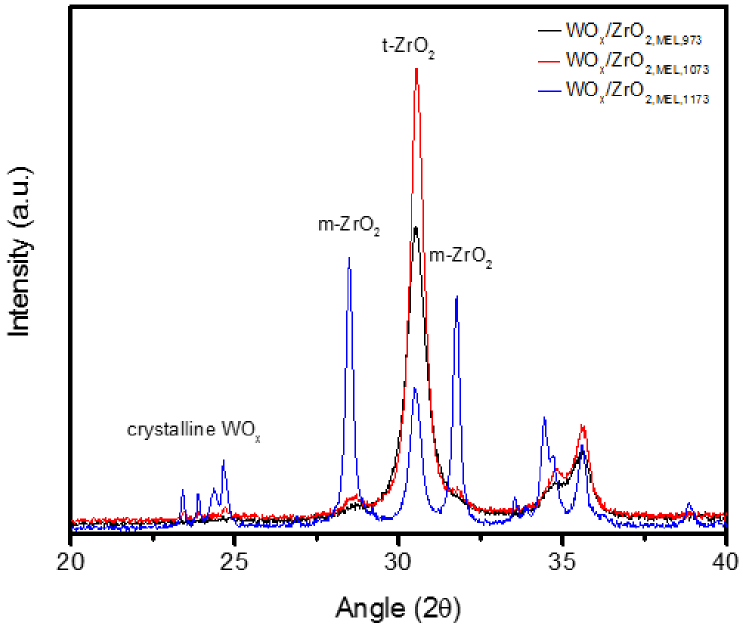

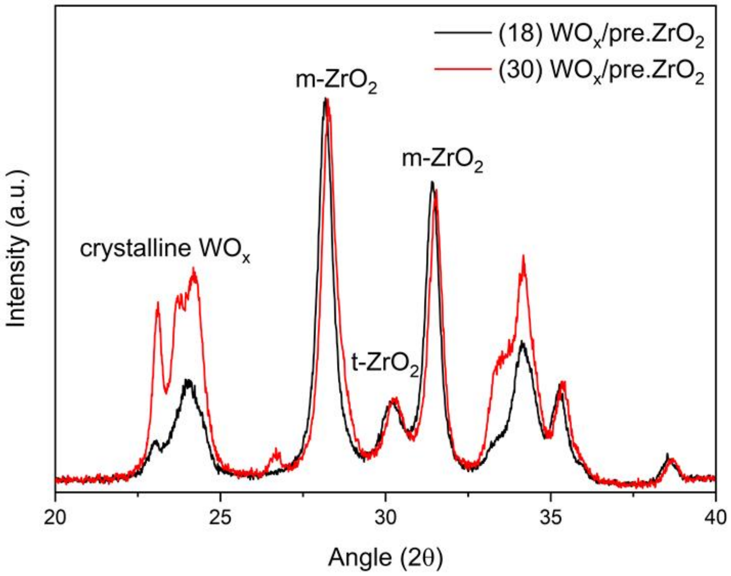

S-Figure 3.3 *XRD patterns of (upper figure) WOx/ZrO2 calcined from WOx/Zr(OH)4 (MEL Chemicals); (lower figure) the two WOx/ZrO2 samples prepared from crystalline ZrO2 (see Experimental in the main text). The surface W density was varied by increasing the calcination temperature. Crystallite sizes of WOx estimated by line broadening analysis are compiled in S-Table* 3.3*.*

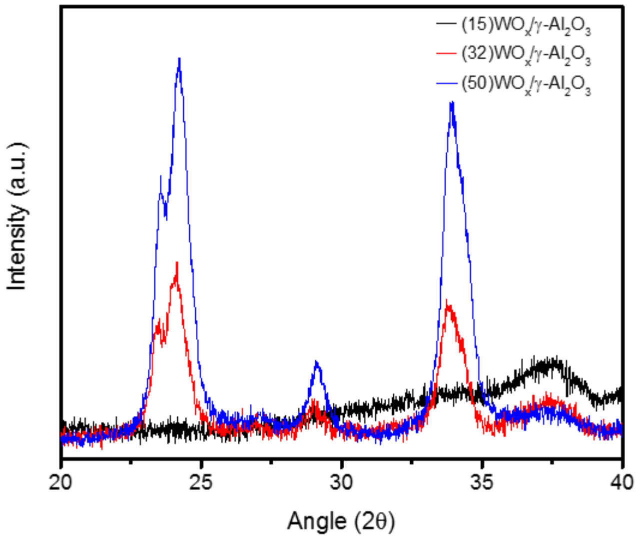

S-Figure 3.4 XRD patterns of WO$_x$/γ-Al$_2$O$_3$ synthesized by incipient wetness impregnation. The calculated W surface densities are 2.2, 6.5 and 16.1 W nm^{-2}, respectively, with increasing tungsten loading from 15 to 50 wt% (reported on the basis of WO$_3$ mass). Crystallite sizes of WO$_x$ estimated by line broadening analysis are compiled in S-Table 3.3

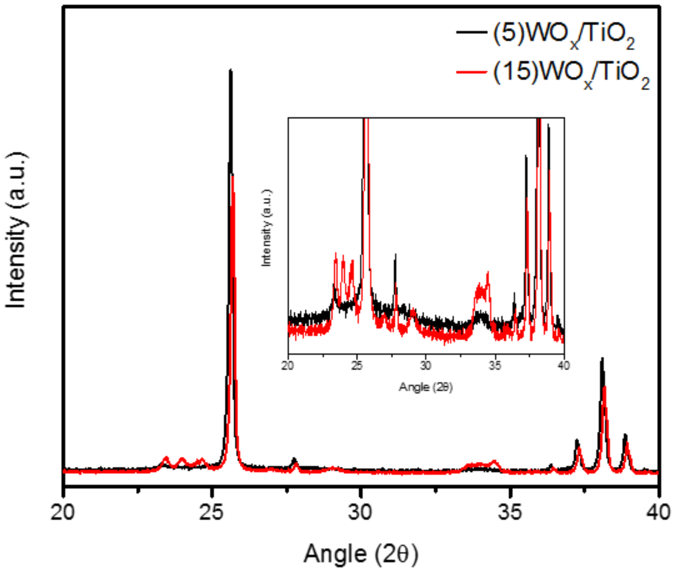

S-Figure 3.5 XRD patterns of tungsten catalysts supported on titania, synthesized by incipient wetness impregnation. The calculated W surface densities are 16.2 and 32.9 W nm^{-2} for tungsten loadings of 5 and 15 wt% (reported on the basis of WO$_3$ mass), respectively. Crystallite sizes of WO$_x$ estimated by line broadening analysis are compiled in S-Table 3.3.

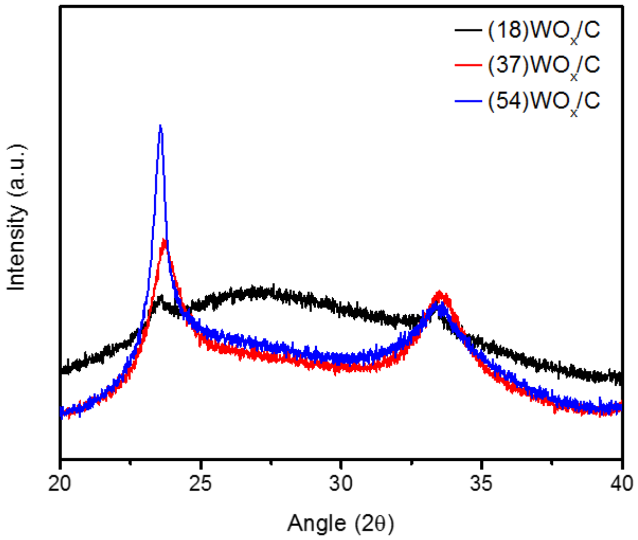

S-Figure 3.6 *XRD patterns of tungsten catalysts supported on activated carbon, synthesized by incipient wetness impregnation. The calculated W surface densities are 0.5, 1.4 and 2.9 W nm^{-2}, respectively, with increasing tungsten loading from 18 to 54 wt% (reported on the basis of WO_3 mass). Crystallite sizes of WO_x estimated by line broadening analysis are compiled in S-Table 3.3.*

When comparing peak shapes of the WO_x-reflections (2θ = 23.1°, 23.5° and 24.4°) in the XRD-patterns of S-Figure 3.3-6, one recognizes differences in the structure of the tungstate domains depending on the underlaying support material. For example, comparing (54)WO_x/C and (15)WO_x/Al_2O_3 with approximately the same surface density of 2-3 W nm^{-2}, the reflections of WO_x on activated carbon are broad, yet already showing the formation of crystalline WO_3, while on the tungstated alumina catalyst the WO_x domains are well dispersed and XRD-amorphous, in view of the absence of reflections at 2θ of 23.1°, 23.5° and 24.4°. With increasing W loading on alumina, the reflections at 23.1° and 23.5° gained in intensity due to the formation of larger WO_x crystallites. On WO_x/C, the only significant peak is observed at 23.1°. Similarly, a comparison of (50)WO_x/Al_2O_3 and (5)WO_x/TiO_2 with similar surface densities (~16 W nm^{-2}) shows that the tungstate domain is much better dispersed on TiO_2 compared to the alumina-supported counterpart (S-Figure 3.7). From these observations, in combination with the activity for alcohol dehydration reaction reported in Figure 3.1 (main text), we conclude that a better dispersion of WO_x does not play a key role ((54)WO_x/C being the most active and (15)WO_x/Al_2O_3 the least active), though the structural differences of the tungstate domains could account for some of the activity differences.

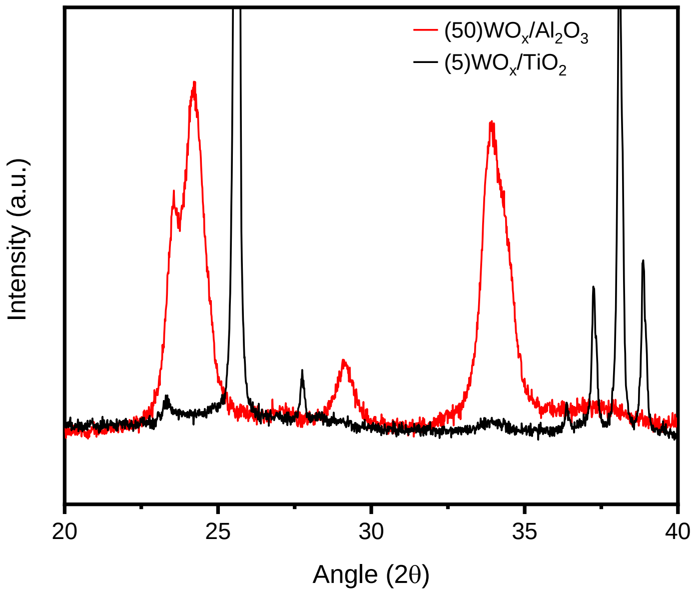

S-Figure 3.7 *A comparison of XRD patterns of representative* WO_x/TiO_2 *and* WO_x/Al_2O_3 *catalysts at similar surface coverage of* WO_x*-domains (~16 W nm*$^{-2}$*).*

3.4.4) Raman spectra

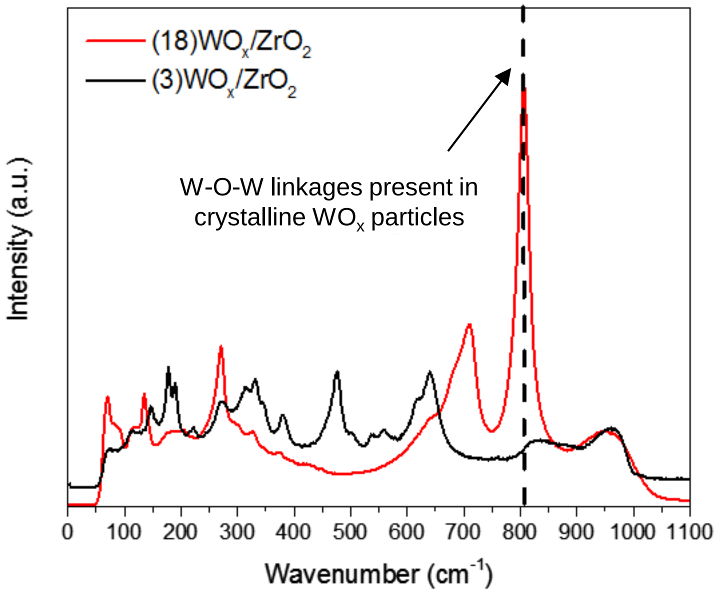

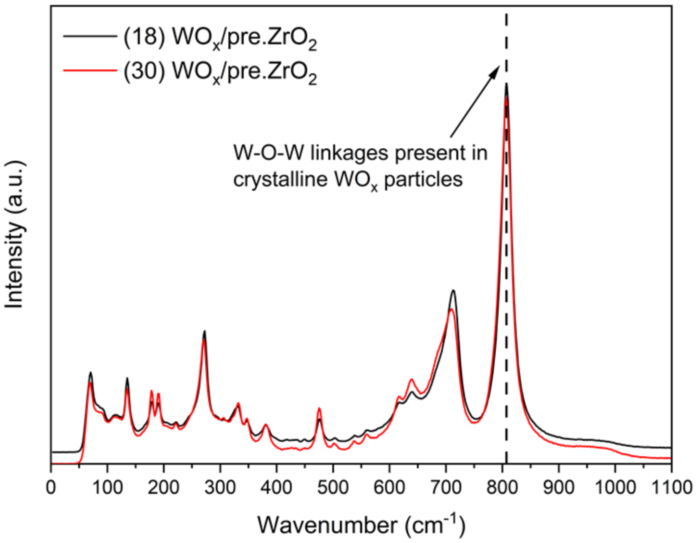

***S-Figure 3.8** Raman spectra of (upper figure) two selected WO_x/ZrO_2 catalysts within the second series (see Experimental in the main text), one below monolayer coverage (1.2 W nm^{-2}), the other around monolayer coverage (4.6 W nm^{-2}); (lower figure) two WO_x/ZrO_2 catalysts prepared from crystalline ZrO_2. Raman features of W-O-W linkages at 805 cm^{-1} are detectable after reaching the monolayer coverage (~4 W nm^{-2}) on ZrO_2.*

The Raman spectra of supported WO_x/ZrO_2 catalysts show bands attributed to crystalline m-WO_3 (133, 178, 187, 272, 327, 417, 437, 448, 715, 805 cm^{-1}), with the most prominent features appearing at 715 and 805 cm^{-1}, while vibrations of the crystalline ZrO_2 support dominate at lower Raman shifts.[5-3] For all oxide-supported materials, the feature at ~805 cm^{-1}, attributed to the presence of W-O-W linkages in crystalline WO_x structures (to be more precise, the stretching mode of W-O-W), is the most dominant among the WO_x-related bands, irrespective of the W loading. On ZrO_2-supported tungstate materials, this band becomes detectable only after reaching the monolayer coverage, whereas on Al_2O_3-supported samples, this band is already evident on a sample containing nominal submonolayer coverage ((15)WO_x/Al_2O_3, S-Figure 3.9). On TiO_2-supported tungstate catalysts, the 805 cm^{-1} peak is already visible on (5)WO_x/TiO_2, while the intensity increases by several fold on (5)WO_x/TiO_2, along with the appearance of the 715 cm^{-1} feature. Note also the Raman features (950–1015 cm^{-1}) that reflect a distribution of distorted WO_6 units in the framework associated with surface $O{=}WO_4$.

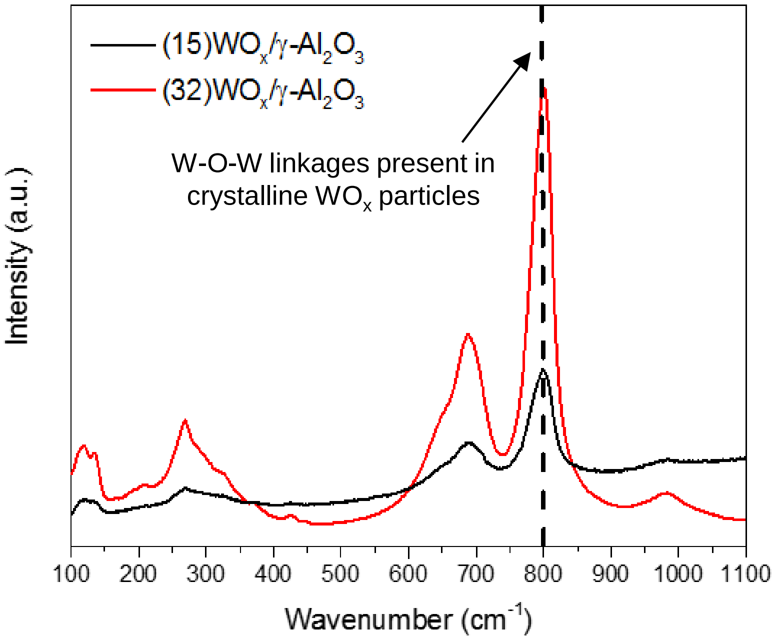

S-Figure 3.9 *Raman spectra for two selected tungstated alumina catalysts, one below monolayer coverage (2.2 W nm^{-2}), the other exceeding monolayer coverage (6.5 W nm^{-2}). Raman features of W-O-W linkages at 807 cm^{-1} are detectable even at a coverage of 2.2 W nm^{-2} on alumina surfaces.*

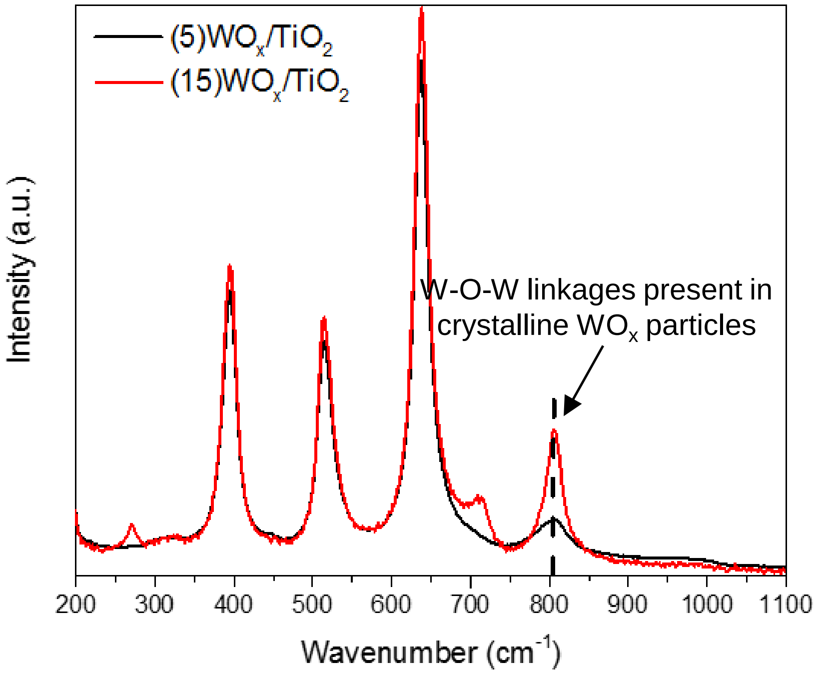

S-Figure 3.10 *Raman spectra for two selected WO$_x$/TiO$_2$ catalysts exceeding theoretical monolayer coverage. The corresponding surface densities of these materials are 16 and 33 W nm^{-2}, with increasing loading from 5 to 15 wt.% WO$_3$. Raman bands centered at 390, 515 and 639 cm^{-1} correspond to the B$_{1g}$, A$_{1g}$ or B$_{2g}$, and E$_g$ modes of the anatase tetragonal phase, respectively.*

S-Table 3.3 *WO_x-crystallite sizes estimated using the Scherrer equation (N.D. = not determined due to the lack of reflections).*

Support	wt.% WO_3	Surface W density ($W\ nm^{-2}$)	$d_{WOx\ crystallites}$ (nm)
Al_2O_3	15	2.2	N.D.
Al_2O_3	32	6.5	8.5
Al_2O_3	50	16.1	9.6
ZrO_2	16	4.1	N.D.
ZrO_2	16	5.6	8.8
ZrO_2	16	20.4	38.7
pre.ZrO_2[a]	18	14.2	15.8
pre.ZrO_2[a]	30	46.0	21.1
TiO_2	5	11.0	N.D.
TiO_2	15	32.5	N.D.
C	18	0.5	1.0
C	37	1.4	4.1
C	54	2.9	7.7

[a] The support was crystalline ZrO_2 formed by calcining the MEL-$Zr(OH)_4$ at 973 K (Experimental).

S-Table 3.4 *Turnover frequencies (TOFs) of representative tungstated catalysts for reactions with substituted cyclohexanols (2-methylcyclohexanol (2-MeCyOH), Sigma-Aldrich 99%, cis/trans mixture; 4-methylcyclohexanol (4-MeCyOH), Sigma-Aldrich 98%, cis/trans mixture; 1-methylcyclohexanol (1-MeCyOH), Sigma-Aldrich 96%). Activity measurements were carried out at standard conditions (473 K, 0.33 M alcohol in water, 0.1-0.2 g of catalyst); only reactions with 1-MeCyOH were carried out at lower temperature (383 K) due to its higher reactivity.*

Entry	**Alcohol, T_{rxn}**	**Support**	**TOF (s^{-1})**
1	CyOH, 473 K	$(32)WO_x/Al_2O_3$	2.6×10^{-2}
2		$(18)WO_x/ZrO_2$	8.7×10^{-2}
3		$(24)WO_x/C$	3.5×10^{-1}
4	2-MeCyOH, 473 K	$(32)WO_x/Al_2O_3$	8.0×10^{-2}
5		$(18)WO_x/ZrO_2$	2.3×10^{-1}
6		$(24)WO_x/C$	7.4×10^{-1}
7	4-MeCyOH, 473 K	$(32)WO_x/Al_2O_3$	1.9×10^{-2}
8		$(18)WO_x/ZrO_2$	4.2×10^{-2}
9		$(24)WO_x/C$	2.6×10^{-1}
10	1-MeCyOH, 383 K	$(32)WO_x/Al_2O_3$	4.9×10^{-3}
11		$(18)WO_x/ZrO_2$	2.4×10^{-2}
12		$(24)WO_x/C$	1.6×10^{-1}

3.4.5) IR spectroscopy of adsorbed CO_2

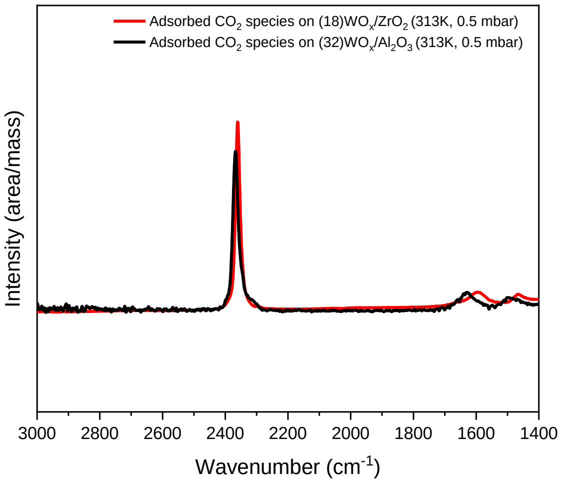

S-Figure 3.11 *IR spectra of adsorbed carbon dioxide on two representative tungstated materials. Bands of linearly adsorbed CO_2, carbonates, bridged carbonates and carboxylates are generally found at 2360, 1530-1620, 1620-1670 and 1350-1420 cm^{-1}, respectively. All spectra having been normalized to pellet area and mass, the ratio of integral intensities for the linearly adsorbed CO_2 band (2360 cm^{-1}) is qualitatively in agreement with the relative H^+ counts in Table 3.1.*

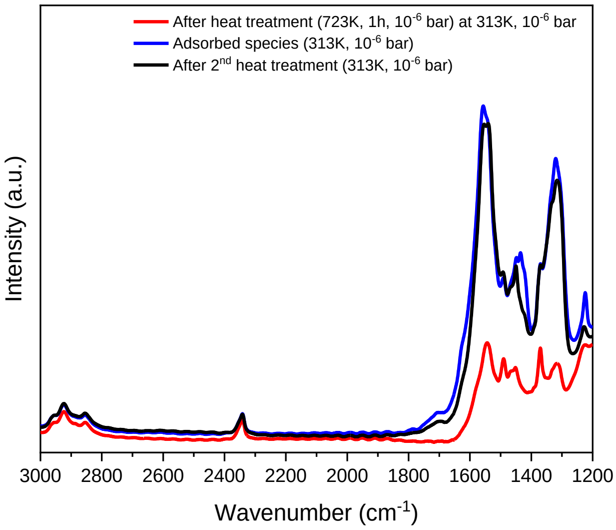

S-Figure 3.12 *IR-spectra of adsorbed carbon dioxide on ZrO_2 ($Zr(OH)_4$ preactivated at 973 K, 4 h in static air). Bands of linearly adsorbed CO_2, carbonates, bridged carbonates and carboxylates are generally found at 2360, 1530-1620, 1620-1670 and 1350-1420 cm^{-1}, respectively.*

3.4.6) Reaction order measurement

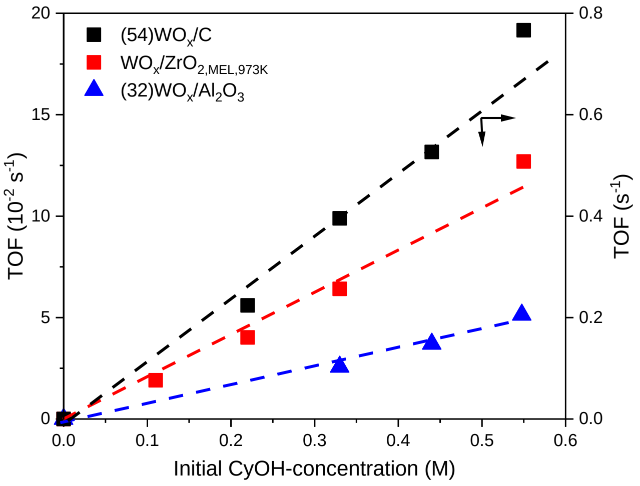

S-Figure 3.13 *Olefin formation rate is first order with respect to alcohol concentration for representative tungstated materials with comparable W surface densities (■ 2.9 W nm^{-2} WO_x/C, ● 4.1 W nm^{-2} WO_x/ZrO_2, ▲ 6.5 W nm^{-2} WO_x/Al_2O_3).*

3.4.7) Aqueous-phase cyclohexanol adsorption

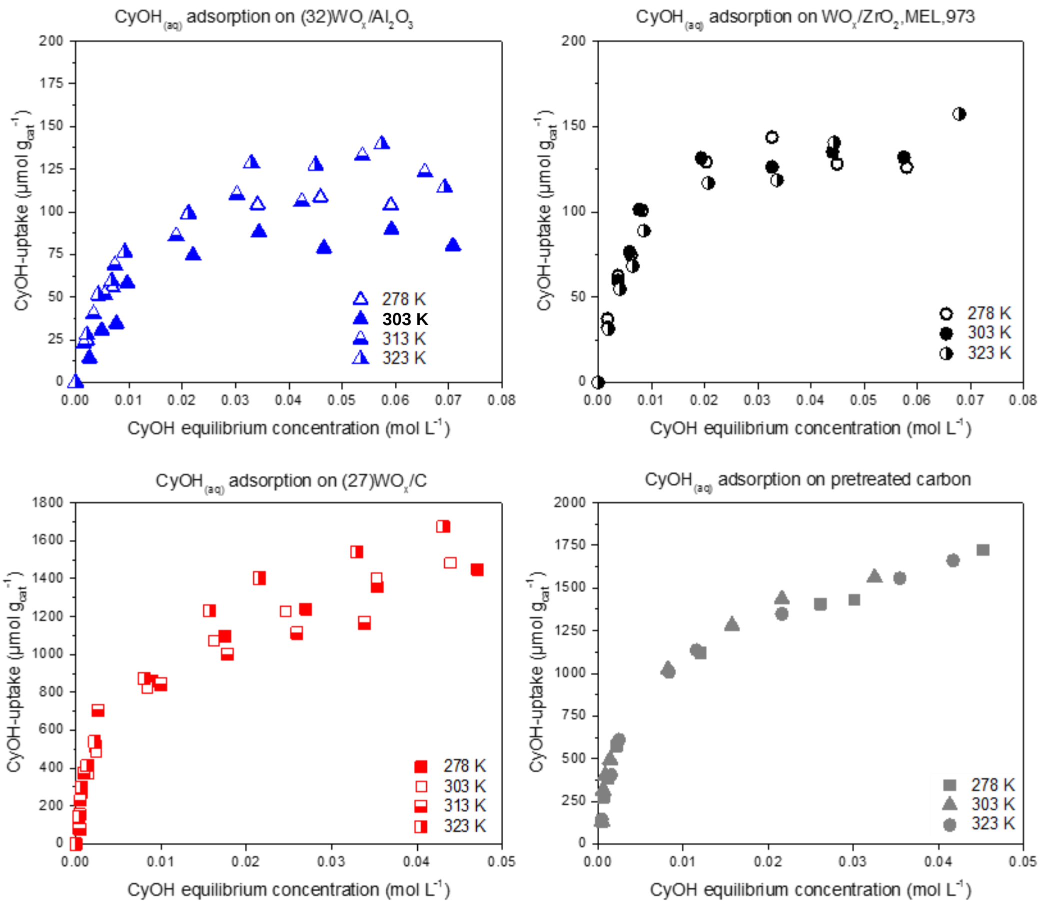

***S-Figure 3.14** Liquid phase adsorption of cyclohexanol from aqueous solutions (0.003-0.075 mol L^{-1}) on selected representative tungstated materials and pretreated activated carbon (973 K, 4 h in N_2).*

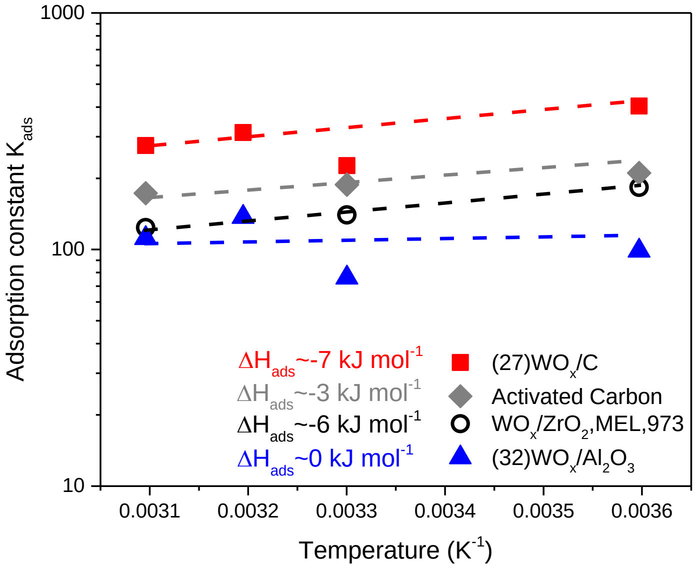

S-Figure 3.15 *Van't Hoff plots of adsorption constants (K_{ads}) determined from fitting the corresponding data in S-Figure 3.14 to Langmuir isotherms.*

At near ambient temperatures (278-323 K), the adsorption constant was similar between WOx/Al_2O_3 and WO_x/ZrO_2, while being a factor of 2-3 larger on WO_x/C than on WO_x/Al_2O_3. Based on the heat of adsorption, it can be predicted that the differences in the adsorption constant should become smaller between WO_x/C and WO_x/Al_2O_3 at reaction temperatures (e.g., 473 K), because the adsorption on the former catalyst would become less strong (i.e., K_{ads} decreases with T, since delta H_{ads} ~ -7 kJ mol^{-1}) while the adsorption on the latter should remain almost unchanged (i.e., K_{ads} hardly changes with T since delta H_{ads} ~ 0 kJ mol^{-1}) at reaction temperatures. Applying the same reasoning, the adsorption constant on WO_x/ZrO_2 should be smaller than that on WO_x/Al_2O_3 at reaction temperatures. By and large, the heat of adsorption values (S-Figure 3.15) suggest that the adsorption strength should be comparable at reaction temperatures. Nevertheless, the less satisfactory trendlines of the regressed K_{ads} in the Van't Hoff plots and the significant uncertainties in the adsorption enthalpy precluded a reliable extrapolation of these values to reaction temperatures, and thus a quantitative comparison of adsorption constants at reaction conditions was not made.

3.4.8) Gas-phase water adsorption measured by microbalance

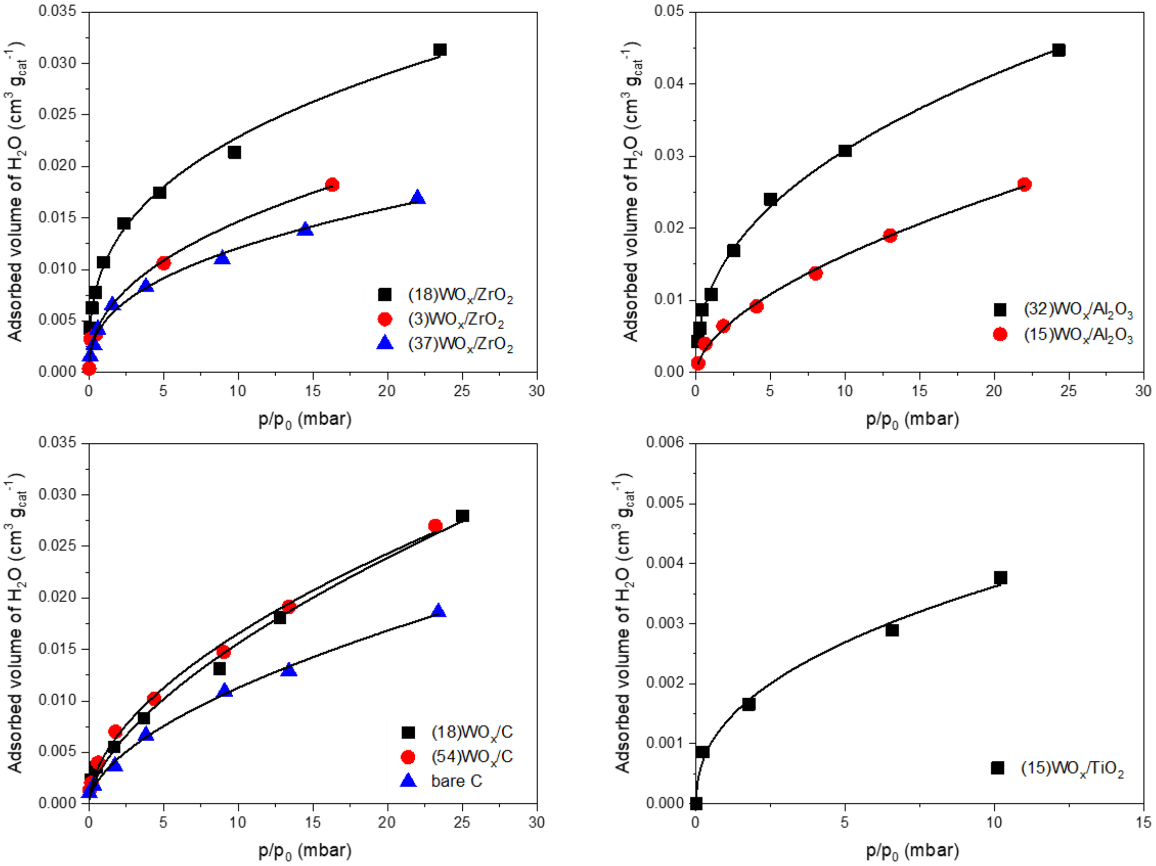

S-Figure 3.16 *Water adsorption at 313 K on representative materials.*

S-Figure 3.16 provides the water adsorption isotherms measured at 313 K for representative samples. This information was used to estimate the volume of the electrical double layer (EDL) surrounding the WO_x-domains on the catalyst surface. Specifically, the volumetric water uptake at 70 mbar (obtained from extrapolation, see below), which is the saturation vapor pressure of water at 313 K, was assumed to be equivalent to that of the EDL at reaction conditions (473 K, 40 bar N_2). It was also assumed that the titrated BAS (H_3O^+) are uniformly distributed in that volume to yield an approximation of an “ionic strength” (S-Table 3.5, column 4) in the EDL engulfing the tungstate domains. The values in column 4 of S-Table 3.5 are plotted as the x-axis in Figure 3.2A in the main text. In S-Note 1, it is established that the actual EDL and ionic strength maintains the same relationship over the temperature range 313-473 K.[4]

Extrapolation of measured isotherm data to P_{H2O} = 70 mbar was done by fitting the adsorption data to a Freundlich-type isotherm with the fit function $q(p) = K_F \cdot p^{\frac{1}{n}}$. The water uptake on bare activated carbon (pretreated in flowing N_2, at 973 K for 4 h) was subtracted from the values obtained for WO_x/C materials without any further correction for loss in surface area, due to the lack of knowledge about the actual exposed support surface.

S-Table 3.5 *Approximated ionic strength, volume of water adsorbed on WO_x domains (at 70 mbar and 313 K) and corresponding turnover frequencies (TOFs) of representative catalysts. For the calculation of the average distance between neighboring hydronium ions, we used the water-layer thickness of 0.49 nm obtained from S-Figure 3.17. Average distance between neighboring hydronium ions (d_{H+}) is not shown for samples with submonolayer WO_x-coverages, due to non-corrected adsorption of water on oxide supports and the inflated estimate of the EDL volume*

Catalyst	Adsorbed water, V_{water} (cm^3 g$_{cat}^{-1}$)	BAS concentration in a catalyst (µmol$_{BAS}$ g$_{cat}^{-1}$)	"Ionic strength" H^+/V_{water} (mol$_{H+}$ L^{-1})	Average distance between hydronium ions, d_{H+} (nm)	TOF at 473 K (s^{-1})
$(15)WO_x/Al_2O_3$	0.051	15	0.3	/	0.005
$(24)WO_x/Al_2O_3$	0.069	94	1.4	1.56	0.018
$(32)WO_x/Al_2O_3$	0.070	140	2.0	1.29	0.026
$(3)WO_x/ZrO_2$	0.034	4	0.1	/	0.017
$(18)WO_x/ZrO_2$	0.045	159	3.6	0.96	0.087
$(18)WO_x/pre.ZrO_2$	0.017	40	2.4	1.16	0.050
$(24)WO_x/ZrO_2$	0.043	123	2.9	1.07	0.088
$(37)WO_x/ZrO_2$	0.026	71	2.7	1.11	0.084
$(15)WO_x/TiO_2$	0.008	23	2.8	1.09	0.136
Activated carbon	0.035	Not measured	/	/	/
$(7)WO_x/C$	0.026	79	3.0	1.05	0.078
$(18)WO_x/C$	0.017	81	4.6	0.85	0.326
$(54)WO_x/C$	0.014	79	5.5	0.77	0.323

By dividing the values in the column 2 of S-Table 3.5 by the BET surface area (m² g$_{cat}^{-1}$, Table 3.1 in the main text) for catalysts, whose support surfaces are fully covered by tungstates (i.e., monolayer coverage), the thickness of the water layer is estimated to be 4.2, 5.2, 5.4 and 6.7 Å for $(18)WO_x/ZrO_2$, $(37)WO_x/ZrO_2$, $(32)WO_x/Al_2O_3$ and $(15)WO_x/TiO_2$, respectively. This magnitude appears to be in line with the knowledge that the typical thickness of the EDL is on the order of 1 nm or less,[5,6] suggesting that the measured volumetric uptake of water is a reasonable proxy of the EDL volume at reaction conditions.

As a reality check for the WO_x/C catalysts, we calculated the effective exposed area of WO_x crystallites based on X-ray diffraction results (S-Table 3.3). Assuming a hemispherical shape for WO_3 particles, one obtains the average geometric area and volume of such a WO_3 particle and thus can calculate the moles of W within the particle.

From the geometric area of hemispherical WO_3 and the amount of protons stabilized over that domain (H^+/W ratio; Table 3.2, main text), a H^+/nm^2 ratio and consequently the average distance between neighboring hydronium ions (d_{H+}) were obtained. For (18)WO_x/C and (54)WO_x/C, the values of d_{H+} were estimated to be 0.65 and 0.41 nm, respectively. These values are very similar to those estimated based on the gas-phase water uptake (S-Table 3.5, column 6), when assuming an average water-layer thickness of 0.49 nm around the WO_x-domain as determined from S-Figure 3.17.

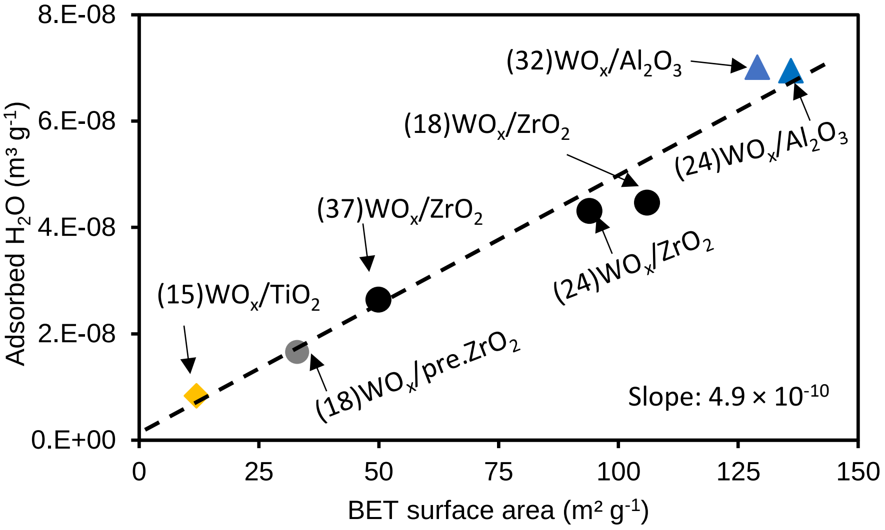

S-Figure 3.17 *Estimation of the average thickness of the water layer formed in equilibration with saturation vapor pressure of water at 313 K (70 mbar)*

3.4.9) S-Note 1

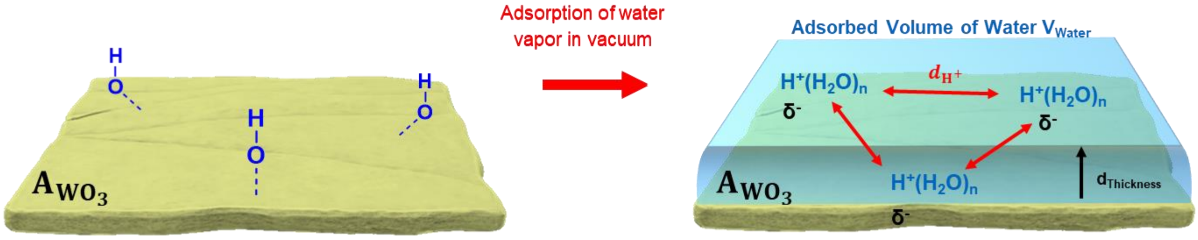

S-Figure 3.18 *Graphical model of water adsorption on* WO_x*-domain, adapted from the main text.* V_{Water} *is defined as the adsorbed water on* WO_x*-domain only (corrected for adsorption on support material),* $d_{Thickness}$ *can be seen as the multiplication of the kinetic diameter of* H_2O *(0.265 nm)*[50] *and the number of water-layers on the* WO_x*-surface and is determined from S-Figure 3.17.* $\boldsymbol{d_{H^+}}$ *is the average distance of hydronium ions on the tungsten oxide surface (*$\boldsymbol{A_{WO_3}}$*).*

$$A_{WO_3}\left[\frac{\mathrm{nm}^2}{\mathrm{g}}\right] = \frac{V_{Water}\left[\frac{\mathrm{nm}^3}{\mathrm{g}}\right]}{d_{Thickness}} \tag{S-Eq. 1}$$

$$d_{H^+}[\mathrm{nm}] = \sqrt{\frac{A_{WO_3}\left[\frac{\mathrm{nm}^2}{\mathrm{g}}\right]}{\mathrm{BAS}\left[\frac{\mathrm{\mu mol}_{H^+}}{\mathrm{g}}\right] \times N_A\left[\frac{1}{\mathrm{mol}}\right]}} \tag{S-Eq. 2}$$

The thickness of the EDL estimated from S-Table 3.5; S-Figure 3.17 and associated text for gas-phase suggests >1 monolayer of water surrounding the WO_x-surface, when considering the kinetic diameter of H_2O being 0.265 nm. Thus, applying S-Eq. 1 and S-Eq. 2 we obtain Figure 3.2B in the main text, describing the TOF as being an exponential function of the average distance ($\boldsymbol{d_{H^+}}$) of the interfacial hydronium ions near the active phase. Increasing the number of shells, by fixing the adsorbed volume (V_{Water}) reported in S-Table 3.5 (column 2), decreases consequently the accessible area of WO_3 (A_{WO_3}) that hosts the EDL, e.g., increasing the number of H_2O-layers to >10, leads to an average distance of the protons already in the range of a C-C bond length (0.154 nm). Thus, we conclude that the reported $\boldsymbol{d_{H^+}}$ values for one to two shells of water are in a reasonable magnitude.

3.4.10) S-Note 2

We further draw the reader's attention to the fact that the correlation of TOFs at 473 K are associated with ionic strength in the EDL estimated from water adsorption at 313

K (see S-Table 3.5 and associated text for details). To evaluate how the EDL dimension changes with temperature, we plot the Debye length from 273-523 K in S-Figure 3.18. Debye length is characteristic of the EDL length, which is a function of the dielectric constant of solvent (ε_r), ionic strength (I, mol L^{-1}) and temperature (T) (S-Eq. 3).[8]

$$\lambda_D = \sqrt{\frac{\varepsilon_r \varepsilon_0 k_B T}{2 * 10^3 N_A q_e^2 I}} \qquad \text{(S-Eq. 3)}$$

where ε_0 is the vacuum permittivity, k_B is the Boltzmann's constant, 10^3 is the conversion factor from the mol L^{-1} units of concentration into mol m^{-3}, N_A is the Avogadro's number, q_e is the elementary charge. In general, the Debye length increases with temperature, however in aqueous phase it is compensated by the decrease of dielectric constant of water (S-Figure 3.18). In consequence, the Debye length at 473 K is only 15% smaller than that at 313 K. It seems then reasonable to assume for the present study that the actual EDL dimension maintains the same relationship over the temperature range 313-473 K.

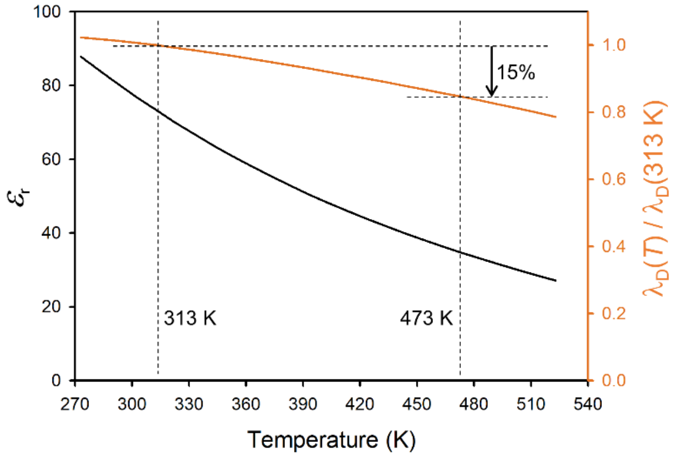

S-Figure 3.19 Dielectric constant of water (ε_r) and Debye length (λ_D) normalized to the value at 313 K as a function of temperature (Data from the reference: Uematsu, M. & Franck, E. U. Static dielectric constant of water and steam[9]).

3.4.11) References

1 Barton, D. G., Shtein, M., Wilson, R. D., Soled, S. L. & Iglesia, E. Structure and Electronic Properties of Solid Acids Based on Tungsten Oxide Nanostructures. *The Journal of Physical Chemistry B* **103**, 630-640, doi:10.1021/jp983555d (1999).

2 Hino, M. & Arata, K. Synthesis of solid superacid of tungsten oxide supported on zirconia and its catalytic action for reactions of butane and pentane. *Journal of the Chemical Society, Chemical Communications*, 1259-1260, doi:10.1039/C39880001259 (1988).

3 Horsley, J. A., Wachs, I. E., Brown, J. M., Via, G. H. & Hardcastle, F. D. Structure of surface tungsten oxide species in the tungsten trioxide/alumina supported oxide system from x-ray absorption near-edge spectroscopy and Raman spectroscopy. *The Journal of Physical Chemistry* **91**, 4014-4020, doi:10.1021/j100299a018 (1987).

4 Kuba, S. *et al.* Redox properties of tungstated zirconia catalysts: Relevance to the activation of n-alkanes. *Physical Chemistry Chemical Physics* **3**, 146-154, doi:10.1039/B007774G (2001).

5 Ross-Medgaarden, E. I. *et al.* New insights into the nature of the acidic catalytic active sites present in ZrO2-supported tungsten oxide catalysts. *Journal of Catalysis* **256**, 108-125, doi:https://doi.org/10.1016/j.jcat.2008.03.003 (2008).

6 Ross-Medgaarden, E. I. & Wachs, I. E. Structural Determination of Bulk and Surface Tungsten Oxides with UV−vis Diffuse Reflectance Spectroscopy and Raman Spectroscopy. *The Journal of Physical Chemistry C* **111**, 15089-15099, doi:10.1021/jp074219c (2007).

7 Scheithauer, M. *et al.* Characterization of WOx/ZrO2by Vibrational Spectroscopy andn-Pentane Isomerization Catalysis. *Journal of Catalysis* **180**, 1-13, doi:https://doi.org/10.1006/jcat.1998.2237 (1998).

8 Scheithauer, M., Grasselli, R. K. & Knözinger, H. Genesis and Structure of WOx/ZrO2 Solid Acid Catalysts. *Langmuir* **14**, 3019-3029, doi:10.1021/la971399g (1998).

9 Wachs, I. E. Raman and IR studies of surface metal oxide species on oxide supports: Supported metal oxide catalysts. *Catalysis Today* **27**, 437-455, doi:https://doi.org/10.1016/0920-5861(95)00203-0 (1996).

10 Zhou, W. *et al.* Identification of active Zr–WOx clusters on a ZrO2 support for solid acid catalysts. *Nature Chemistry* **1**, 722-728, doi:10.1038/nchem.433 (2009).

11 Zhou, W. *et al.* Nature of Catalytically Active Sites in the Supported WO3/ZrO2 Solid Acid System: A Current Perspective. *ACS Catalysis* **7**, 2181-2198, doi:10.1021/acscatal.6b03697 (2017).

12 Baertsch, C. D., Komala, K. T., Chua, Y.-H. & Iglesia, E. Genesis of Brønsted Acid Sites during Dehydration of 2-Butanol on Tungsten Oxide Catalysts. *Journal of Catalysis* **205**, 44-57, doi:https://doi.org/10.1006/jcat.2001.3426 (2002).

13 Macht, J. *et al.* Support effects on Brønsted acid site densities and alcohol dehydration turnover rates on tungsten oxide domains. *Journal of Catalysis* **227**, 479-491, doi:https://doi.org/10.1016/j.jcat.2004.08.014 (2004).

14 Herrera, J. E. *et al.* Synthesis, characterization, and catalytic function of novel highly dispersed tungsten oxide catalysts on mesoporous silica. *Journal of Catalysis* **239**, 200-211, doi:https://doi.org/10.1016/j.jcat.2006.01.034 (2006).

15 Shi, D. *et al.* WOx supported on γ-Al2O3 with different morphologies as model catalysts for alkanol dehydration. *Journal of Catalysis* **363**, 1-8, doi:https://doi.org/10.1016/j.jcat.2018.04.004 (2018).

16 Mallesham, B., Sudarsanam, P., Raju, G. & Reddy, B. M. Design of highly efficient Mo and W-promoted SnO_2 solid acids for heterogeneous catalysis: acetalization of bio-glycerol. *Green Chemistry* **15**, 478-489, doi:10.1039/C2GC36152C (2013).

17 Park, Y.-M., Chung, S.-H., Eom, H. J., Lee, J.-S. & Lee, K.-Y. Tungsten oxide zirconia as solid superacid catalyst for esterification of waste acid oil (dark oil). *Bioresource Technology* **101**, 6589-6593, doi:https://doi.org/10.1016/j.biortech.2010.03.109 (2010).

18 Liu, Y., Luo, C. & Liu, H. Tungsten Trioxide Promoted Selective Conversion of Cellulose into Propylene Glycol and Ethylene Glycol on a Ruthenium Catalyst. *Angewandte Chemie International Edition* **51**, 3249-3253, doi:10.1002/anie.201200351 (2012).

19 Baertsch, C. D., Soled, S. L. & Iglesia, E. Isotopic and Chemical Titration of Acid Sites in Tungsten Oxide Domains Supported on Zirconia. *The Journal of Physical Chemistry B* **105**, 1320-1330, doi:10.1021/jp003073d (2001).

20 Barton, D. G., Soled, S. L., Meitzner, G. D., Fuentes, G. A. & Iglesia, E. Structural and Catalytic Characterization of Solid Acids Based on Zirconia Modified by Tungsten Oxide. *Journal of Catalysis* **181**, 57-72, doi:https://doi.org/10.1006/jcat.1998.2269 (1999).

21 Macht, J. & Iglesia, E. Structure and function of oxide nanostructures: catalytic consequences of size and composition. *Physical Chemistry Chemical Physics* **10**, 5331-5343, doi:10.1039/B805251D (2008).

22 Shi, H., Eckstein, S., Vjunov, A., Camaioni, D. M. & Lercher, J. A. Tailoring nanoscopic confines to maximize catalytic activity of hydronium ions. *Nature Communications* **8**, 15442, doi:10.1038/ncomms15442

https://www.nature.com/articles/ncomms15442#supplementary-information (2017).

23 Wang, M. *et al.* Genesis and Stability of Hydronium Ions in Zeolite Channels. *Journal of the American Chemical Society* **141**, 3444-3455, doi:10.1021/jacs.8b07969 (2019).

24 de Jong, K. P. *Synthesis of Solid Catalysts*. (Wiley, 2009).

25 Anik, M. & Cansizoglu, T. Dissolution kinetics of WO_3 in acidic solutions. *Journal of Applied Electrochemistry* **36**, 603-608, doi:10.1007/s10800-006-9113-3 (2006).

26 Sudrajat, H. & Babel, S. Role of reactive species in the photocatalytic degradation of amaranth by highly active N-doped $$\mathbf{WO}_{\mathbf{3}}$$WO3. *Bulletin of Materials Science* **40**, 1421-1428, doi:10.1007/s12034-017-1502-1 (2017).

27 Liu, Y. *et al.* Enhancing the catalytic activity of hydronium ions through constrained environments. *Nature Communications* **8**, 14113, doi:10.1038/ncomms14113

https://www.nature.com/articles/ncomms14113#supplementary-information (2017).

28 Ping, Y. & Galli, G. Optimizing the Band Edges of Tungsten Trioxide for Water Oxidation: A First-Principles Study. *The Journal of Physical Chemistry C* **118**, 6019-6028, doi:10.1021/jp410497f (2014).

29 Gould, N. S. & Xu, B. Quantification of acid site densities on zeolites in the presence of solvents via determination of extinction coefficients of adsorbed pyridine. *Journal of Catalysis* **358**, 80-88, doi:https://doi.org/10.1016/j.jcat.2017.11.016 (2018).

30 dos Santos, V. C., Wilson, K., Lee, A. F. & Nakagaki, S. Physicochemical properties of WO_x/ZrO_2 catalysts for palmitic acid esterification. *Applied Catalysis B: Environmental* **162**, 75-84, doi:https://doi.org/10.1016/j.apcatb.2014.06.036 (2015).

31 Martínez, A., Prieto, G., Arribas, M. A. & Concepción, P. Hydroconversion of n-hexadecane over $Pt/WO_x–ZrO_2$ catalysts prepared by a PVA-template

coprecipitation route: The effect of tungsten surface coverage on activity and selectivity. *Applied Catalysis A: General* **309**, 224-236, doi:https://doi.org/10.1016/j.apcata.2006.05.010 (2006).

32 Law, H. Y., Blanchard, J., Carrier, X. & Thomas, C. NOx-TPD as a Tool to Estimate the Accessible Zirconia Surface of ZrO2-Containing Materials. *The Journal of Physical Chemistry C* **114**, 9731-9738, doi:10.1021/jp9089535 (2010).

33 Lyklema, J. in *Fundamentals of Interface and Colloid Science* Vol. 2 751 (1995).

34 Barton, D. G., Soled, S. L. & Iglesia, E. Solid acid catalysts based on supported tungsten oxides. *Topics in Catalysis* **6**, 87-99, doi:10.1023/A:1019126708945 (1998).

35 Albanese, E., Di Valentin, C. & Pacchioni, G. H2O Adsorption on WO3 and WO3–x (001) Surfaces. *ACS Applied Materials & Interfaces* **9**, 23212-23221, doi:10.1021/acsami.7b06139 (2017).

36 Hurtado-Aular, O., Vidal, A. B., Sierraalta, A. & Añez, R. Periodic DFT study of water adsorption on m-WO3(001), m-WO3(100), h-WO3(001) and h-WO3(100). Role of hydroxyl groups on the stability of polar hexagonal surfaces. *Surface Science* **694**, 121558, doi:https://doi.org/10.1016/j.susc.2019.121558 (2020).

37 Cui, Z., Feng, X., Li, H. & Tan, T. Interconversion of Lewis acid and Brønsted acid catalysts in biomass-derived paraxylene synthesis. *Chemical Engineering Science* **227**, 115942, doi:https://doi.org/10.1016/j.ces.2020.115942 (2020).

38 Weingarten, R., Tompsett, G. A., Conner, W. C. & Huber, G. W. Design of solid acid catalysts for aqueous-phase dehydration of carbohydrates: The role of Lewis and Brønsted acid sites. *Journal of Catalysis* **279**, 174-182, doi:https://doi.org/10.1016/j.jcat.2011.01.013 (2011).

39 He, Y. *et al.* Selective catalytic reduction of NO by NH3 with WO3-TiO2 catalysts: Influence of catalyst synthesis method. *Applied Catalysis B: Environmental* **188**, 123-133, doi:https://doi.org/10.1016/j.apcatb.2016.01.072 (2016).

40 Vuurman, M. A., Wachs, I. E. & Hirt, A. M. Structural determination of supported vanadium pentoxide-tungsten trioxide-titania catalysts by in situ Raman spectroscopy and x-ray photoelectron spectroscopy. *The Journal of Physical Chemistry* **95**, 9928-9937, doi:10.1021/j100177a059 (1991).

41 Hintermeier, P. H. *et al.* Hydronium-Ion-Catalyzed Elimination Pathways of Substituted Cyclohexanols in Zeolite H-ZSM5. *ACS Catalysis* **7**, 7822-7829, doi:10.1021/acscatal.7b01582 (2017).

42 Bates, J. S., Bukowski, B. C., Greeley, J. & Gounder, R. Correction: Structure and solvation of confined water and water–ethanol clusters within microporous Brønsted acids and their effects on ethanol dehydration catalysis. *Chemical Science* **11**, 8323-8324, doi:10.1039/D0SC90162H (2020).

43 Cordon, M. J. *et al.* Dominant Role of Entropy in Stabilizing Sugar Isomerization Transition States within Hydrophobic Zeolite Pores. *Journal of the American Chemical Society* **140**, 14244-14266, doi:10.1021/jacs.8b08336 (2018).

44 Nouri-Khorasani, A., Malek, K. & Eikerling, M. Molecular Modeling of Hydronium Ion and Water Distribution in Water-Filled Pt Nanochannels with Corrugated Walls. *Electrocatalysis* **5**, 167-176, doi:10.1007/s12678-013-0174-x (2014).

45 Eckstein, S. *et al.* Influence of Hydronium Ions in Zeolites on Sorption. *Angewandte Chemie International Edition* **58**, 3450-3455, doi:10.1002/anie.201812184 (2019).

46 Emanuele, G. *et al. Nature Portfolio*, doi:10.21203/rs.3.rs-79664/v1 (2021).

47 Vjunov, A. *et al.* Tracking the Chemical Transformations at the Brønsted Acid Site upon Water-Induced Deprotonation in a Zeolite Pore. *Chemistry of Materials* **29**, 9030-9042, doi:10.1021/acs.chemmater.7b02133 (2017).

48 Shaoxian, B. & Shizhu, W. in *Gas Thermohydrodynamic Lubrication and Seals* (eds Bai Shaoxian & Wen Shizhu) 1-14 (Academic Press, 2019).

49 Fokkink, L. G. J., de Keizer, A. & Lyklema, J. Temperature dependence of the electrical double layer on oxides: Rutile and hematite. *Journal of Colloid and*

Interface Science **127**, 116-131, doi:https://doi.org/10.1016/0021-9797(89)90012-X (1989).

50 Ahmad Fauzi Ismail, K. C. K., Takeshi Matsuura. *Fundamentals of Gas Permeation Through Membranes. In: Gas Separation Membranes.*, 14 (2015).

51 Ji, W., Hu, J. & Chen, Y. The structure and surface acidity of zirconia-supported tungsten oxides. *Catalysis Letters* **53**, 15-21, doi:10.1023/A:1019041402892 (1998).

4) Distinct pathways of cyclohexanol dehydration on Lewis and Brønsted acid sites of tungsten-oxide based catalysts

Niklas Pfriem,[1] Florian Zahn,[1] Yihong Lou,[1] Hui Shi,[2,*] Gary L. Haller[1,3] and Johannes A. Lercher[1,4,*]

[1] Department of Chemistry and Catalysis Research Center, TU München, Garching 85747, Germany

[2] School of Chemistry and Chemical Engineering, Yangzhou University, Yangzhou, Jiangsu 225009, China

[3] Yale University, Department of Chemical and Environmental Engineering, New Haven, CT 06520-8682, USA

[4] Institute for Integrated Catalysis, Pacific Northwest National Laboratory, P.O. Box 999, Richland, WA 99352, United States

*Correspondence to: shihui@yzu.edu.cn (H.S.); johannes.lercher@ch.tum.de (J.A.L.)

Authors contributions: H.S. and J.A.L. conceived the research; N.P. measured catalytic activities, analyzed the physicochemical properties of the catalysts and drafted the manuscript, F.Z. and Y.L. helped obtaining reaction data, G.L.H. helped analyzing the data.

This work has not been published

4.1) Abstract

Apolar phase cyclohexanol dehydration in decalin has been investigated over tungstate zirconia catalysts (WO_x/ZrO_2) at relatively mild reaction conditions (423 K). Dehydration in apolar phase occurs via a Bronsted acid catalyzed pathway leading to surface-monomer or -dimer species, showing a strong initial alcohol concentration dependence. To account for the differences of condensed phase to gas phase, acid site quantification is carried out via in-situ titration of various base-molecules. In contrast to previous published studies, a full suppression of the dehydration activity was not achieved by increasing the base load to WO_x/ZrO_2 materials. A substantial residue activity is recognized that is identified by kinetic isotope effects (KIE) and intensive kinetic studies to be a result of Lewis acid centers on the tungsten oxide domain, catalyzing via a E2-like pathway. We show that we can classify surface sites on WO_x/ZrO_2 catalysts to active sites that bind strong (piperidine) and weaker bases (pyridines) and are the major contributor (70-90% at 423K) to catalytic activity. We identified weak acid sites that do not bind pyridine/DTBP, but bind piperidine, and are inactive for dehydration. Last, we recognize weak acid sites that bind none of the investigated N-titrants, but which are catalytically active (10-30% of total activity).The knowledge about these surface sites allows to correctly account for their respective activity (TOFs).

4.2) Introduction

(Mixed-) metal oxides became a standard choice for acid catalyzed reactions in the last centuries [1-4] due to their thermal stability [5,6] and acid strength [7,8]. Tungsten oxide based solid acids have been previously employed as suitable catalysts in gas-phase isomerization reactions,[7,9-18] alcohol dehydration [8,12,19-21] and liquid-phase upgrading processes of biomass-derived feedstocks (e.g., sugars, bio-oils[22-24], and long-chain alcohols [25,26]). In this work we focus on the alcohol dehydration only, which can serve as a probe to explore the catalytic site requirements and reaction pathways over mixed metal oxides containing both Brønsted acid sites (BAS) and Lewis acid sites (LAS). Activities and mechanisms of Lewis acid catalyzed alcohol dehydration are reported in detail over γ-alumina [3,4], zirconia or titania [27,28] catalysts. The BAS catalyzed alcohol conversion is known to proceed via monomer- and dimer-mediated pathways over strong solid acids such as various zeolites in gas [29] and liquid phase [30,31]. Typically the differentiation and quantification of both types of acid sites is done by adsorption of basic probe molecules such as pyridine, 2,6-di-tertbutylpyridine or ammonia in the gas phase phase.[8,32-34] Alternatively, Iglesia et al. titrated the active BAS in-situ during the reaction by increasing the titrant concentration leading to a suppression of the total rate.[19] Results, however, always suggested the LAS activity to be insignificant when comparing with the proton catalyzed pathway on catalyst systems containing both competing types of active species. [26,30]

In this work we doped tungsten oxide on zirconia (WO_x/ZrO_2) to achieve a stable and active catalyst domain that consist of both, BAS and LAS. Cyclohexanol is used as a alcohol representative for a class of molecules coming from biomass upgrading reactions.[35] Macht and Iglesia [36] report the activity of BAS on tungsten domains in the gas phase for butanol dehydration to be intrinsically independent of the support material. They classify the contribution of LAS catalysis as negligible and therefore do not investigate the active sites in terms of its nature and dehydration mechanism. However, Larsen et al. reported that the dehydration of short chain alcohols such as 1-propanol, 2-propanol, and tert-butanol over WO_x/ZrO_2 proceeds solely over Lewis-acid sites [26,37] and structure-function relationships on facetted titania are known to affect the activity in 2-propanol dehydration.[27] Synergistic effects between both LAS and BAS have been published with theoretical and experimental evidence e.g. for the etherification of glycerol and other alcohols from the biomass upgrading family. [26,38,39] Bell et al. reports a noteworthy LAS contribution in the etherification of 1-dodecanol at 393 K over tungstated zirconia in an aprotic solvent. [26] In contrast to Iglesia they propose a stand-alone activity of LAS besides the dominant BAS activity that is attributed to W Lewis-acid sites only. These findings are based on in-situ titration with sterically hindered pyridine, poisoning the surface Brønsted sites only during the reaction. 1-dodecanol consumption still occurs after complete suppression of the BAS contribution, which is assigned to active Lewis acid sites. However, the site specific activities of LAS are in general recognized as orders of magnitude lower than BAS catalyzed. As a consequence literature lacks so far from understanding the mechanisms of alcohol dehydration over tungsten oxide based Lewis acids and how the nature of the LAS impacts on the alcohol dehydration, considering that LAS on the basis of zirconia were found to be inactive for etherification reactions in the liquid phase. Understanding and tuning the Lewis acid catalysis in parallel to the established proton catalyzed pathways, is crucial for an optimized catalyst design.

4.3) Experimental

4.3.1) Preparation and characterization of tungsten oxide-based catalysts

Information about chemicals, catalyst synthesis and characterization, are partly taken from Reference ([40]) as materials may be used in both studies.

All chemicals commercially obtained were used without further purification. Zirconium hydroxide was obtained in the form of $Zr(OH)_4$ (MEL chemicals, batch number: PRB310). Commercial boehmite (CATAPAL® B ALUMINA) was purchased from Sasol. Doubly deionized water (resistivity ~18 MΩ·cm) and ammonium metatungstate hydrate (Sigma-Aldrich, 99.99% trace metals basis) were used to prepare the solution used for impregnation. Cyclohexanol (ReagentPlus®, 99%, Sigma-Aldrich) or cyclohexanol-d_{12} (≥ 98 atom% D, Sigma-Aldrich) was used as the reactant. Decahydronaphthalene (decalin, mixture of cis-and trans isomers, ≥ 99.0%, Sigma-Aldrich) was used as the solvent. Cyclohexen-1-one (≥ 95%, Sigma Aldrich) was added post-reaction as a standard for gas chromatography (GC) analysis. Pyridine (anhydrous, 99.8%, Sigma-Aldrich), 2,6-di-tert-butylpyridine (≥ 95%, Sigma-Aldrich) and piperidine (99%, Sigma-Aldrich) were used during the titration experiments.

A series of WO_x/ZrO_2 catalysts were prepared by incipient wetness impregnation of $Zr(OH)_4$ with aqueous solutions of ammonium metatungstate hydrate containing desired quantities of tungsten. The impregnated sample was dried in static air at 383 K for 12 h, followed by calcination in flowing synthetic air (20 ml min^{-1} g^{-1}) for 4 h at 973 K (ramp: 10 K min^{-1}), and then cooled to room temperature. Tungsten oxide loadings of 8-37 wt.% (in the form of WO_3) were achieved, corresponding to surface densities of 2-20 W/nm^2, calculated using an established method [12]. To prepare pure zirconia and γ-alumina used for control experiments, $Zr(OH)_4$ and boehmite were calcined in flowing synthetic air (20 ml min^{-1} g^{-1}) for 4 h at 973 K (ramp: 10 K min^{-1}).

The determination of weight loadings of W was carried out by the Microanalytical Laboratory at TU München using acidic digestion and subsequent photometric determination using a Shimadzu UV-160 photometer. The BET specific surface areas and pore volumes of the investigated materials were determined by N_2 physisorption, following a standardized protocol. The samples were first activated in vacuum at 473 K, before collecting the N_2 sorption isotherms at liquid nitrogen temperature (77 K) using a PMI Automatic Sorptometer. Powder X-ray diffraction (XRD) was performed on an instrument (Empyrean, PANalytical) equipped with a copper X-ray tube (Cu-K_α radiation, 0.154 nm), a Ni K_β-filter, and a solid-state detector (X'Celerator) operated at 45 kV and 40 mA with a step size of 0.017° and scan time of 115 s per step. Reflection transmission mode from 5 to 70° (2θ) was performed at ambient conditions on samples pressed on a silicon single crystal with a (111) surface. Infrared (IR) spectra of adsorbed pyridine (or ammonia) were obtained with an Perkin-Elmer 2000 spectrometer with a resolution of 4 cm^{-1}. All investigated catalysts and materials were placed as a self-supporting pellet to the machine and activated in vacuum (P=10^{-6} mbar) at 450°C for 1 h (10 K min^{-1}) before approaching the measurement temperature (423 K for pyridine adsorption, 323 K for ammonia isotherms). In a typical pyridine adsorption experiment, the sample as then equilibrated with 0.1 mbar pyridine for 30min followed by outgassing for 1 h. The recorded spectra represents the total chemisorbed pyridine. As a last step, the materials were reheated to 450°C (10 K min^{-1}, 1 h) to desorb weakly adsorbed pyridine and thus yield the number of strong Brønsted (BAS) and Lewis acid sites (LAS). The concentrations of Brønsted and Lewis acid sites were calculated from the integral intensities of the peaks at 1540 and 1450 cm^{-1}, respectively, by applying a molar integral extinction coefficient of 1.67 and 2.22 cm µmol^{-1}.[41] Ammonia isotherms were typically obtained at 323 K, exposing the sample to an increasing pressure of ammonia (0.002-0.3 mbar) while keeping isothermal conditions. All spectra were recorded when adsorption equilibria were reached and the cell was brought back to vacuum (~10^{-6} mbar). Details of the peak assignment from IR spectra with adsorbed ammonia are presented in Section 3.4 and based on well known protocols.[42]

4.3.2) Rate assessments in an isothermal, gradientless stirred tank reactor

Cyclohexanol dehydration was performed in a 300 ml Hastelloy Parr reactor. In a typical experiment, 100 mL of a 0.05-1.0 M cyclohexanol solution (solvent: decalin) and ~200 mg of catalyst were loaded in the reactor. The sealed reactor was then flushed three times with 20 bar N_2, before being pressurizing to an initial N_2-pressure of 40 bar at ambient temperature. The mixture was then heated to the target temperature (T_R, e.g., 473 K). Agitation (700 rpm) was started when the temperature reached (T_R -10), to ensure a negligible conversion during heat-up (confirmed by independent measurements). The reaction time (t_R) was recorded after reaching T_R (time zero). An aliquot (~0.5 mL) of the reaction mixture was sampled at different time intervals through a dip tube connected to a 2-μm filter submerged under the solution. Approximately 0.5 mL of a cyclohexen-1-one solution (0.05 wt.% in decalin) was added as an internal standard to the liquid sample and the mixture was then analyzed by a gas chromatograph (GC, Shimadzu 2010) equipped with a HP-5 capillary column (30 m × 250 μm) and flame ionization detector (FID). Kinetic isotope effects (KIEs; r_H/r_D) were measured by replacing non-deuterated cyclohexanol with cyclohexanol-d_{12}, whose reactions were carried out with the procedure described above. The carbon balance for all experiments was closed to within ± 5 %. Rates per gram of catalyst did not change with the catalyst loading in the reactor. Further increasing the stirring rate also did not lead to appreciable changes in conversion.

Discrimination between acid sites, i.e., Brønsted acid sites (BAS) and Lewis acid sites (LAS), was achieved by titration experiments using pyridine, 2,6-di-tert-butylpyridine and piperidine under reaction conditions. Specifically, different quantities of decalin solutions of a given titrant were added to the starting reaction mixture, and then rates were determined, using the protocol described above, on these pre-titrated samples. The amount of titrant adsorbed on the catalyst was measured from its residual concentration in the solution using the same chromatographic protocols as for other catalytic reactions.

4.4) Results and Discussion

4.4.1) Effect of tungsten surface density on the rate of cyclohexanol dehydration in decalin

The effect of W surface density on the rate of cyclohexanol dehydration was studied for ZrO_2-supported tungstate catalysts. As the W surface densities increased, the prevalent WO_x-domain structures in the series of catalysts evolved from isolated monotungstates through two-dimensional polytungstates to three-dimensional crystalline WO_x nanoparticles, according to the characterization data (S-Figure 4.1-2 and S-Table 4.1-3) and consistent with the literature [7,10,12,13,19,43,44].

Cyclohexanol dehydration in decalin yielded cyclohexene as the predominant product (> 99% selectivity) on the studied WO_x/ZrO_2 catalysts at all tested temperatures (403-473 K). The olefin formation rates were obtained at relatively low conversions (< 20%) and normalized to the total W content (Table 4.1). A maximum in the mass-specific rate of olefin formation was observed at W surface densities of 4-7 W nm^{-2}, corresponding to the theoretical monolayer coverage that was calculated by assuming corner-sharing WO_x octahedra with bond distances derived from monoclinic WO_3.[36,44,45] Bare ZrO_2 was virtually inactive at the same conditions (S-Table 4.2), indicating that LAS and BAS associated with the supports do not play any catalytic role.

The physicochemical properties of tungstated catalysts and the rate variations with W surface density have been extensively studied in the literature and our findings here regarding the rate maxima (Table 4.1) are in general agreement with previous publications [7,8,19,36,44,46]. Tungstate domains of medium size are shown to offer the best compromise between accessibility and delocalization of negative charges formed via reduction of tungstate anions to $H^{\delta+}(WO_3)_n^{\delta-}$. For example, Barton, et al. [7] argued that isolated monotungstates that exist at low W surface densities cannot delocalize the negative charge required for the formation of BAS, whereas an excess negative charge may be delocalized over polytungstate species that form at intermediate WO_x surface densities, hence the high activity on the latter type of domains. Exceeding the monolayer coverage, however, leads to the formation of WO_x crystals that become less intimately connected to the support surfaces and reside predominantly at inaccessible locations, when compared to the monolayer structure, causing the W-based reaction rates to decrease.[19] Taken together, dehydration rates per W atom (Table 4.1) reflect the convoluted effects of the dispersion of WO_x domains and the reactivities of BAS and LAS coexisting in these samples.

In the following subsections, detailed kinetic evaluations are presented for representative materials chosen from a series with different W-loadings corresponding to sub-monolayer, monolayer and supra-monolayer regimes.[36] We specifically focus on the evolution of W surface density on the concentration and strength of LAS and BAS and their catalytic consequences. [36]

Table 4.1 *Catalyst mass based and W-based dehydration rates. Reaction conditions: 423 K, 1.0 M CyOH in decalin. (Only strictly comparable conditions, surface-dimer regime, see also Figure 4.2)*

Catalyst	Prior-titration dehydration rate (423 K)	
	Catalyst mass based (μmol g^{-1} s^{-1})	W-based (10^{-3} mol mol_W^{-1} s^{-1})
(8)WO_x/ZrO_2	0.22	0.6
(18)WO_x/ZrO_2	8.24	11.2
(37)WO_x/ZrO_2	7.24	4.6

4.4.2) Titration of acid sites by different bases varying in strength and steric hindrance

BAS and LAS of varying strength and concentrations coexist on supported tungstate catalysts [8,47,48]. Titration methods can be employed to measure acid site concentrations during catalysis and to discern the individual catalytic involvement of BAS and LAS[19] [26] . Three organic base titrants were used in this work, all being similar in size to cyclohexanol. Pyridine (proton affinity: 930 kJ mol^{-1}) and piperidine (proton affinity: 954 kJ mol^{-1}) are known to adsorb on both BAS and LAS, while 2,6-di-tert-butylpyridine (DTBP) almost exclusively adsorbs on BAS but cannot coordinate to LAS because of steric hindrance around its nitrogen atom [8,34,49]. The strength of the acid sites also plays a role, potentially rendering adsorption on some weak sites hardly possible at reaction conditions.

Table 4.2 *BAS concentration (BAS$_{titration}$) determined via titration of catalysts using 2,6-di-tert-butylpyridine (DTBP) and pyridine, rates corrected for post-titration rates and normalized to total Brønsted acid sites determined by in-situ titration. Note: Post-titration rates are independent of the alcohol concentration (shown later). BAS counts are independent of initial alcohol concentration and temperature (shown in SI). Reaction conditions: 443 K, 1.0 M CyOH in decalin. (Only strictly comparable conditions, surface-dimer regime, see also Figure 4.2)*

Catalyst	Post-titration residue mass-specific activity (µmol g^{-1} s^{-1})	Corrected mass-specific dehydration rate (µmol g^{-1} s^{-1})	BAS$_{titration}$ (µmol g^{-1})	TOF$_{BAS}$ (s^{-1})
(8)WO_x/ZrO_2	0.13	0.09	6	0.02
(18)WO_x/ZrO_2	3.90	4.33	100	0.04
(37)WO_x/ZrO_2	2.88	4.39	67	0.07

Dehydration rates decreased linearly with increasing titrant uptake for all three organic base titrants (Figure 4.1(A), see also S-Figure 4.6-8). Independent of the catalyst loading, however, a full suppression of the dehydration rate was not achieved by either pyridine or DTBP. Our observations for cyclohexanol in-situ titration apparently contrast those reported by Macht et al. for gas-phase 2-butanol dehydration on various supported tungstate catalysts; those authors showed that titrant uptakes were greater for pyridine than for DTBP and that pyridine titration suppressed 2-butanol dehydration activity almost completely[19]. Rorrer and Bell also found for liquid-phase 1-dodecanol etherification and unimolecular dehydration that no alkene was formed once all BAS on WO_x/ZrO_2 were poisoned by pyridine or DTBP at ~400 K.[26]

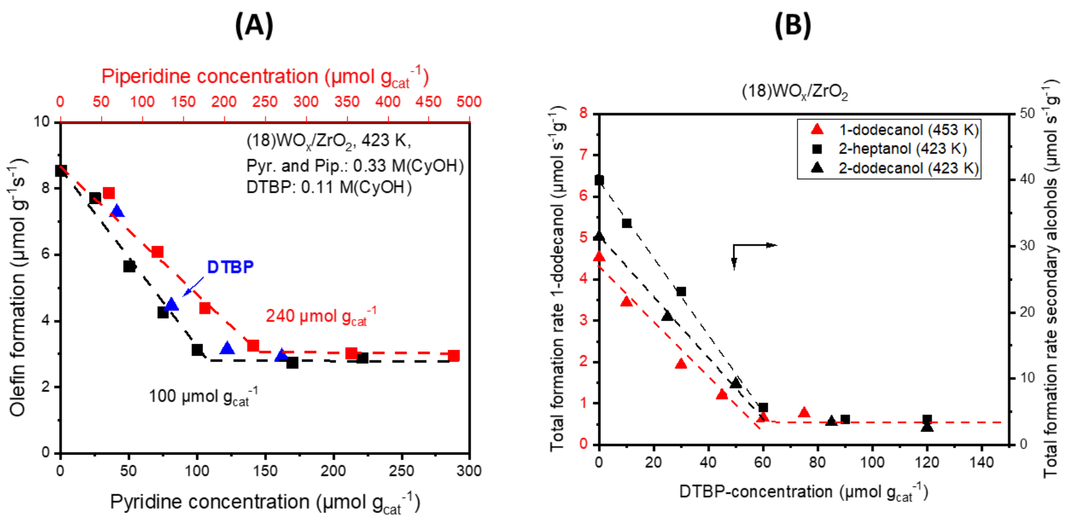

Figure 4.1 *(A)Titration of acid sites on an exemplary WO_x/ZrO_2 catalyst. (See also S-Figure 4.6-8 for the other two materials) All data points were from independent batch measurements with varying concentrations of the titrant added in the mixture. Titration experiments were performed at an alcohol concentration of either 0.11 M or 0.33 M. The temperature is set to 423 K. (B) Base Titration of (18)WO_x/ZrO_2 with DTBP at 423K or 453K for primary and secondary alcohols. For all linear alcohols the initial concentration is fixed to 0.05 mol L^{-1}.*

To address the origin of the different titration behavior, in-situ titration experiments with DTBP were carried out varying the nature of the substrate from linear primary alcohols (1-dodecanol) to linear secondary alcohols (2-heptanol, 2-dodecanol). The formation rate (Figure 4.1(B)) of the tungstated zirconia catalyst being considered as covered by a WO_x-monolayer becomes suppressed from originally ~40 µmol g_{cat}^{-1} (2-heptanol) to a plateau at around ~4 µmol g_{cat}^{-1} when increasing the base concentration. Similarly, the dehydration rate of 2-dodecanol is suppressed from ~31 µmol g_{cat}^{-1} to ~2 µmol g_{cat}^{-1}. Thus, the plateau regime of the linear secondary alcohols is much less in activity when comparing the rate ratio: rate(total observed rate)/rate(post-titration). This ratio is 3 for cyclohexanol over 18WO_x/ZrO_2, 10 for 2-heptanol and 12 for 2-dodecanol. For better comparison to Rorrer and Bell [26] the same analysis was carried out for a primary alcohol (1-dodecanol). The rate gets suppressed by a factor of 11 for 1-dodecanol. Note that the actual titrated sites with linear (long chain) alcohols are less than compared to titration with cyclic cyclohexanol. One possible explanation for the diverging site counts, assuming the used catalyst batch for these experiments is identical in site counts as for CyOH-titration, could be steric effects of the linear alcohols, considering a portion of sites being inaccessible for these classes of alcohols. The active sites would be potentially strong BAS, as their rate could be suppressed to a minimum. Inaccessible BAS and LAS do not contribute significantly to the activity, so near complete titration is possible. These results suggest that our observations in Figure 4.1(A) do not fully contrast Rorrer and Bell. [26] Titration of cyclohexanol dehydration with a significant plateau activity at high base concentrations, is most likely due to the cyclic secondary alcohol structure of cyclohexanol, accessing additional sites for reaction. For completeness, we tested the acid site counts and found them not to be function of temperature or alcohol concentration, when obtained with in-situ titration approach (S-Figure 4. 9-10).

In the present work, piperidine did not affect the post-titration activity on WO_x/ZrO_2 catalysts. For this series of catalysts, the maximum uptake of piperidine was significantly higher than of those of the two pyridines (Figure 4.1(A)). This is expected, since piperidine being a stronger base than the pyridines and should be able to probe both strong and relatively weak acid sites.[50] However, the same residual activity after reaching maximum uptakes of the three bases on $(18)WO_x/ZrO_2$ indicates that the sites, which cannot be titrated by pyridine but can bind piperidine, are inactive for dehydration. The concentration of these inactive sites on WO_x/ZrO_2 may be estimated from the difference between pyridine and piperidine uptakes, which was the smallest on $(37)WO_x/ZrO_2$ with the lowest dispersion of WO_x domains. The remaining active sites on WO_x/ZrO_2 after piperidine titration appear to be substantially weaker in acid strength such that even piperidine cannot be adsorbed on these sites.

Altogether, we have on WO_x/ZrO_2 catalysts at least three classes of sites: (1) active sites that bind all three titrants and are the major contributor (70-90% at 423 K) to catalytic activity; (2) weak acid sites that do not bind pyridine/DTBP, but bind piperidine, and are inactive for dehydration; (3) weak acid sites that bind none of the N-titrants, but which are catalytically active (10-30% of total activity). The inactive acid sites and those responsible for the residual dehydration rates may be weak BAS or LAS, though their precise chemical identities cannot be determined from these experiments. It is interesting to consider the fact that type 3 sites are not capable of binding piperidine but can catalyze dehydration, while type 2 sites can bind piperidine but cannot catalyze dehydration. It is unlikely that both are classifiable as BAS, because in such cases, the weaker sites (type 3, active, non-piperidine-binding) should not show a higher catalytic activity than the stronger sites (type 2, inactive, piperidine-binding). In turn, it may be argued that type 2 and type 3 sites are of disparate nature, one being BAS and the other being LAS. We conclude that the pyridine/DTBP poisons these active BAS, while terminal W-OH and Zr-OH, as well as peripheral W-O(H)-M (M = Al, Zr) structures, are potential candidates for weak, inactive BAS. Because the Zr-OH groups are minimally exposed on catalysts covered with tungstate-monolayers or crystallites (S-Figure 4.5), the weak BAS are more likely to be W-OH linkages on (18)WO_x/ZrO_2 and (37)WO_x/ZrO_2.

The site counts of relatively strong and catalytically relevant BAS were obtained from the uptakes of DTBP (or pyridine), assuming that DTBP adsorbs on these sites with a 1:1 stoichiometry. Although these BAS concentrations did not entirely follow the same trend as the values obtained from the quantitative analysis of IR spectra of adsorbed pyridine (i.e., gas phase measurements, S-Table 4.4, S-Figure 4.5), the set of values were of comparable magnitude to each other. For example, in situ titration experiments gave BAS concentrations of 6, 100, 67 µmol g^{-1} for the three WO_x/ZrO_2 catalysts, compared to 2, 60, 11 µmol g^{-1} determined by IR (S-Table 4.4). According to the in situ BAS counts, the H^+/W ratio drastically increased from 0.014 (submonolayer) to 0.141 (monolayer) and then decreased to 0.037 (supramonolayer) with increasing WO_x loading on ZrO_2, which is in line with previous findings.[36]

Surprisingly, the maximum uptake of pyridine was either identical to, or slightly higher than (likely for steric reasons), that of DTBP, which suggests that during liquid-phase catalysis, pyridine is almost exclusively adsorbed on BAS while being hardly adsorbed on the LAS. In contrast, a substantial amount of LAS was probed by pyridine during gas-phase IR measurements, though a large fraction of those appeared to be rather weak in acid strength (S-Table 4.3). Moreover, pyridine was found to saturate both BAS and LAS on tungstate catalysts during gas-phase dehydration of 2-butanol.[8,19] In line with our observation, however, Rorrer and Bell found that pyridine and DTBP uptakes required to fully suppress liquid-phase etherification and dehydration rates of 1-dodecanol were nearly the same on a WO_x/ZrO_2 catalyst.[26] These results lead us to hypothesize that the very different conditions for gas-phase and liquid-phase experiments, including the adsorption of alcohol and solvent on BAS and LAS for the latter case, are responsible for such discrepancies in the binding ability of pyridine on BAS and LAS.

Turnover frequencies (TOFs) were obtained by normalizing the mass-specific rates to the site counts determined by in situ titration. The TOF (corrected rates for post-titration activity) of the catalytically relevant BAS was estimated to be 0.02-0.07 s^{-1} among the three catalysts at 423 K and increasing with the weight loading. The remaining activity after pyridine/DTBP titration was substantial, accounting for 10-30% of the total activity (Table 4.2 and Figure 4.1). From this data it was not possible to obtain upper-bound estimates for the concentration of catalytically active LAS.

4.4.3) Rate dependences on the alcohol concentration over tungstate catalysts

It has been well established that alcohol dehydration rates on Brønsted acidic solids (zeolites and polyoxometallates) in the gas phase and in apolar liquids decrease asymptotically with increasing alcohol partial pressures or concentrations [29,51-55]. This characteristic feature, often attributed to the formation of a much less reactive surface dimer species on BAS, is also observed here over the series of tungstated catalysts at a temperatures of 423 K (Figure 4.2 (A)). A typical reaction mechanism accounting for such kinetics involves the monomer- and dimer-mediated pathways that have been extensively discussed in prior contributions.[29,30] This mechanism (Figure 4.3) appears to be universally applicable for BAS-catalyzed alcohol dehydration, as long as the dimer formation is not prohibited by spatial constraints.

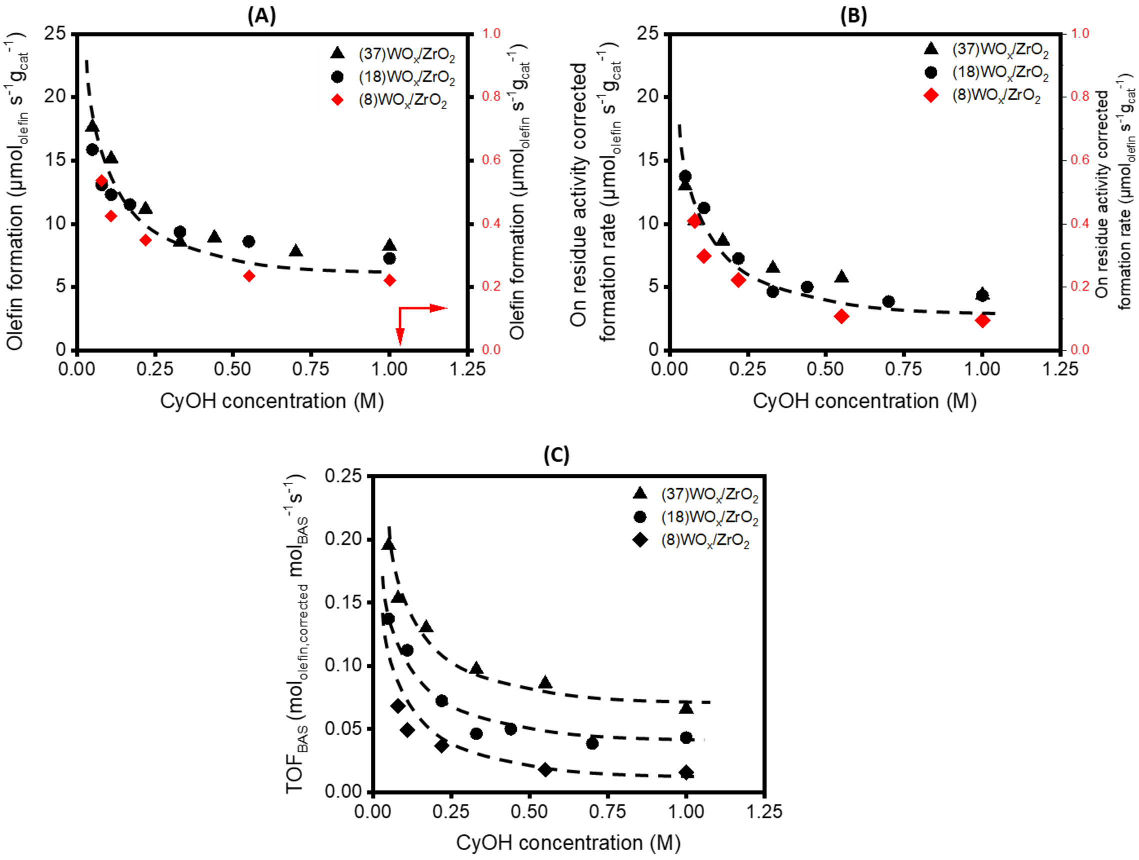

Figure 4.2 *(A) Rates of cyclohexene formation as a function of cyclohexanol concentration. Cyclohexanol dehydration was performed in an alcohol concentration range of 0.05-1.0 M in decalin (other conditions: 0.05-0.4 g_{cat}, 40 bar N_2, 423 K, conversion ≤ 20%). Rates were corrected for residue activity (B) and normalized to titratable BAS counts (C).*

Based on the mechanism illustrated in (Figure 4.3), the following rate expressions have been derived for olefin formation via monomer- and dimer-mediated elimination routes on catalytically active BAS:

$$\frac{r_{BAS}}{[H^+]_0}=\frac{k_M K_1[CyOH]+k_D K_1 K_2[CyOH]^2}{1+K_1[CyOH]+K_1 K_2[CyOH]^2} \qquad \text{(Eq. 4.1)}$$

where k_M and k_D are the intrinsic rate constants of water elimination from the monomer and dimer pathways, respectively; K_1 is the equilibrium constant for alcohol adsorption on the BAS and K_2 is the equilibrium constant for alcohol dimer formation from an alcohol monomer interacting with a liquid-phase alcohol; $[H^+]_0$ represents the pyridine-titrated concentration of BAS (Table 4.2). These equations and their derivations have been reported previously [29], so the details are not repeated here. While Eq. 4.1 is the general form of rate expression encompassing all coverages, Eq. 4.2 can be derived by assuming active BAS to be fully covered with alcohol-derived species ($1 << K_1[CyOH]+K_1K_2[CyOH]^2$):

$$\frac{r_{BAS}}{[H^+]_0}=\frac{k_M+k_D K_2[CyOH]}{1+K_2[CyOH]} \qquad \text{(Eq. 4.2)}$$

At both low and relatively high concentrations of cyclohexanol, modest H/D kinetic isotope effects (KIEs) of 1.2-1.4 were registered on representative WO_x/ZrO_2 catalysts, suggesting that both monomer and dimer routes proceed via rate-determining C-O bond cleavage with limited C-H_β bond cleavage at the transition state.

However, Eq. 4.2 only considers the rate contribution from the pyridine/DTBP-titrated BAS, while we clearly showed the presence of another set of catalytically active sites (Figure 4.1 (A)). Distinct from the negative rate dependence on alcohol concentration for the pristine catalysts, the rates measured on the counterparts pre-titrated with pyridine (separate batch experiments) were insensitive to changes in the alcohol concentration (Figure 4.4). The zero-order kinetics on the pyridine-poisoned catalysts suggests that the active sites that persist after pyridine titration are not BAS, which would exhibit decreasing activity with increasing cyclohexanol concentration (assuming the same behavior as delocalized protons). In turn, these results add further evidence, in addition to arguments presented in the previous section, that LAS are responsible for the residual activity after pyridine/DTBP titration.

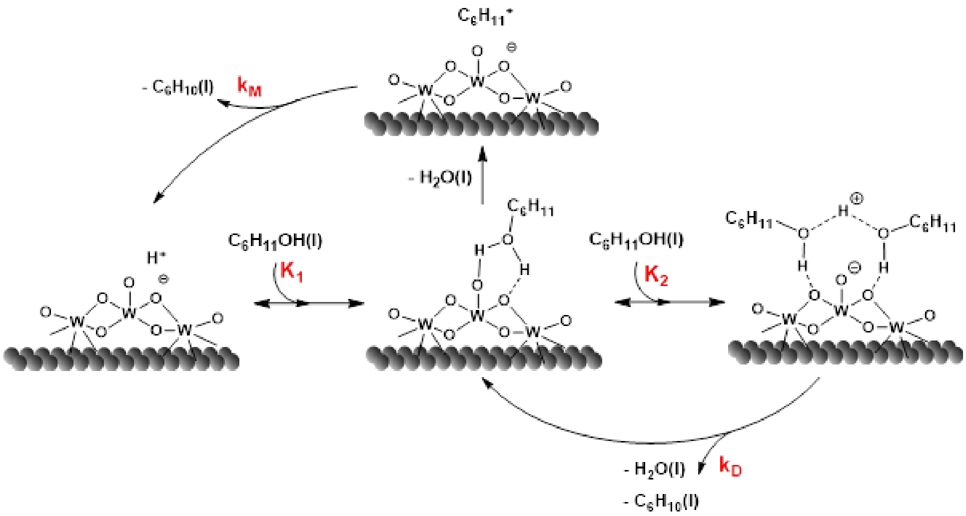

Figure 4.3 *An illustration of a plausible sequence of steps involved in intramolecular dehydration of cyclohexanol catalyzed by BAS on tungstate domains.* [29,30]

For the studied WO_x/ZrO_2 (18 and 37 wt% WO_3-loading) catalysts with (supra)monolayer coverages of WO_x domains, the support surfaces are minimally exposed, as demonstrated in previous works[7,14,56] and verified here (S-Figure 4.3) by IR spectra of CO_2 adsorption showing no carbonate formation (CO_2 adsorbs on ZrO_2 but not on WO_3). Moreover, bare ZrO_2 supports showed negligible activities at these conditions (S-Table 4.2). Thus, sites on support surfaces are not responsible for the residual rates after titration with pyridine or DTBP. Instead, tungsten centers must represent the major form of LAS that are active on these catalysts. As a result, the additional sites that are titrated by piperidine on (18)WO_x/ZrO_2 and (37)WO_x/ZrO_2 catalysts are concluded to be weak BAS that do not retain pyridines and are inactive for dehydration.

To provide insights into the mechanism of LAS-catalyzed dehydration, H/D KIEs were measured for the pair of non-deuterated and perdeuterated cyclohexanol reactants on the pyridine-poisoned catalysts where only LAS are active for dehydration. Given that the dehydration of alcohols on metal oxides (e.g., TiO_2, ZrO_2, γ-Al_2O_3) preferentially proceeds via an E2-type elimination route requiring Lewis acid-base pairs and involving a transition state (TS) with some carbenium-ion character[28], the magnitude of KIEs likely reflects the different progress of bond breaking and making in the concerted elimination TS, rather than a shift in the RDS for a stepwise elimination route. H/D kinetic isotope effects measured for pyridine-titrated WO_x/ZrO_2 catalysts on which all catalytically relevant BAS were poisoned and only LAS remained available for catalysis, showed a KIE of 1.4 (for (18) WO_x/ZrO_2) and 1.4 (for (37) WO_x/ZrO_2). These modest KIEs typically arise from rehybridization of the C_α from sp^3 to sp^2, indicating a substantial degree of C_α-O bond cleavage in the TS of the rate-determining step (RDS).[57] It may be that the C_β-H(D) bond cleavage (proton abstraction) does not substantially occur, or that both the C_β-H(D) bond scission and the O_{cat}-H(D) bond formation are almost complete, or that the TS is nearly symmetrical with respect to the C_β-H(D) bond scission and O_{cat}-H(D) bond formation.

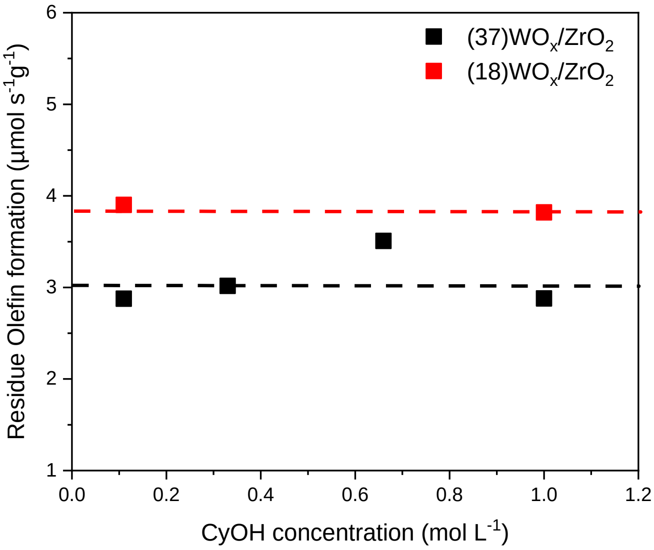

Figure 4.4 *Insensitivity of olefin formation rate to the variation in cyclohexanol concentration on pre-titrated tungstate catalysts. Titrant concentration (pyridine) was chosen to ensure a complete suppression of BAS activity on both materials. Other conditions were: 423 K, 40 bar, 0.1* g_{cat}

Knowing the main contributor to the activity being (titratable) BAS and tungsten centers (LAS) being responsible for the residue activity, the total rate equation can be expressed as Eq. 4.3 comprising rate contributions from catalytically active BAS and LAS (r_{BAS}+r_{LAS}):

$$r_{total} = r_{BAS} + r_{LAS} = [BAS]TOF_{BAS} + [LAS]TOF_{LAS} \qquad \text{(Eq. 4.3)}$$

in which r_{LAS} corresponds to the residual rate after pyridine/DTBP titration. At full coverages of both BAS and LAS, we have:

$$r_{total} = [BAS]\frac{k_M + k_D K_2[\mathrm{CyOH}]}{1 + K_2[\mathrm{CyOH}]} + [LAS]k_{LAS} \qquad \text{(Eq. 4.4)}$$

in which k_{LAS} is the zero-order rate constant (equal to rates measured for LAS-catalyzed dehydration in zero-order regime, Figure 4.4).

For the present study, Eq. 4.2 and Eq. 4.4 satisfactorily describes all experimental data measured at temperatures no higher than 453 K. Further increasing the temperature caused the fraction of unoccupied BAS to increase and the formation of surface alcohol monomers and dimers to become less favorable (more so for alcohol dimers than for monomers). Consequently, the reaction order in alcohol eventually shifted to positive values at T > 453 K (not shown). We restrain the analysis to the kinetic regime with negative reaction orders, for which the TOF_{BAS}-concentration curves can be obtained with Eq. 4.2 to calculate the intrinsic kinetic and thermodynamic parameters (k_M, k_D and K_2). A detailed analysis of the activation parameters is beyond the scope of this work, it requires high quality data for multiple temperatures and can be subject to future studies.

4.5) Conclusion

Alcohol dehydration reactions on tungstate zirconia catalysts can be titrated in condensed apolar phase by base molecules such as pyridines or piperidines. In contrast to gas phase results, where uptakes were greater for pyridine than for DTBP both yield in condensed phase approximately the same uptake. The steric hindrance of the alcohol determines the titration behavior, as it was shown for cyclic, secondary alcohols, and show a significant residue activity when titrated by strong bases, while rates of primary (long chain) alcohols can be suppressed to near total loss of activity. The activity in apolar phase comes dominantly from BAS sites, catalyzing the reaction via a monomer- and dimer-mediated route, which is known in the literature for zeolite catalysis and as we have shown are also true for mesoporous mixed oxide systems. Beyond that we showed that weak Lewis acid sites contribute to up to 30% of the overall activity, following an E2-like mechanism.

4.6) Supporting Information

Distinct pathways of cyclohexanol dehydration on Lewis and Brønsted acid sites of tungsten-oxide based catalysts

Content:

Supporting kinetic analysis:

Supporting characterization:

Stability tests:

***S-Table 4.1** General properties of the tungstated catalysts studied in this work. See also* [40]

Catalyst	WO_x-loading (wt.%)[a]	BET surface area (m^2 g^{-1})	W-surface density (W nm^{-2})
(8)WO_x/ZrO_2	8	90	2.3
(18)WO_x/ZrO_2	18	106	4.6
(37)WO_x/ZrO_2	37	50	19.5

[a] Measured loadings in the form of WO_3.

***S-Table 4.2** Measurements of the catalytic activities of bare supports. Conditions: 0.4 g of catalyst, T = 443 K, 40 bar N_2 and 0.33 M CyOH in decalin.*

Support	BET surface area m^2 g^{-1}	Olefin formation rate µmol $s^{-1}g_{cat}^{-1}$
ZrO_2	166	$<10^{-3}$

4.6.1) X-ray diffraction

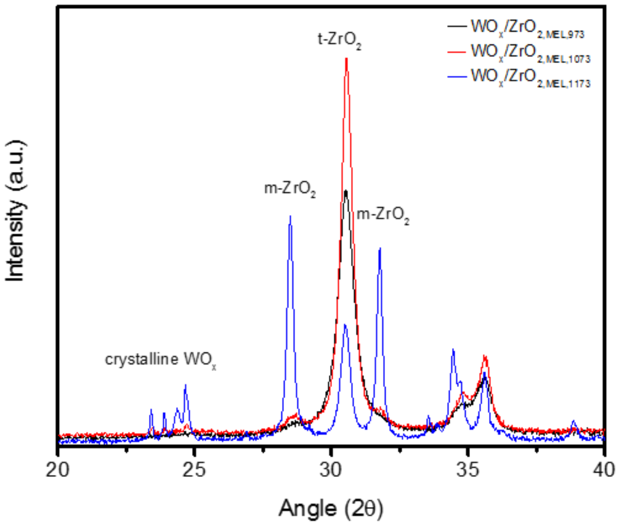

S-Figure 4.1 *XRD patterns of tungsten catalysts supported on* ZrO_2*, purchased from MEL Chemicals. The surface W density is varied by increasing the calcination temperature. The calculated W surface densities are 4.1, 5.6 and 20.4 W* nm^{-2}*, respectively, with increasing calcination temperature from 973 to 1173 K. Crystallite sizes of* WO_x *estimated by line broadening analysis are compiled in S-Table 4.2.*

4.6.2) Raman spectra

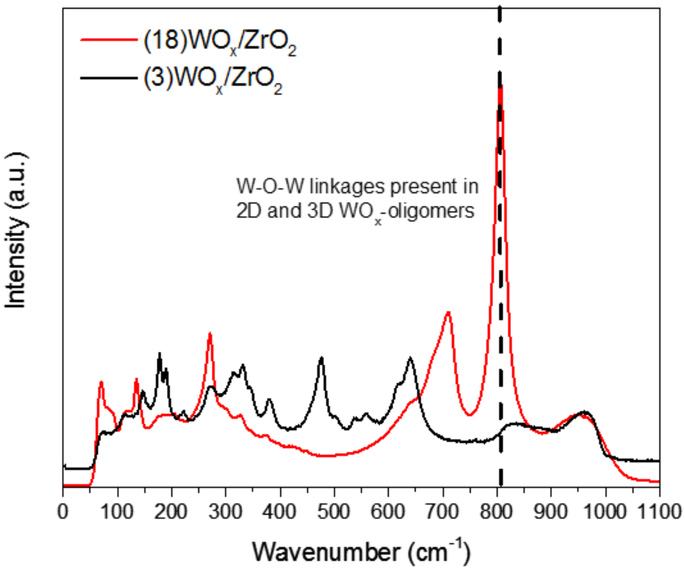

S-Figure 4.2 *Raman spectra for two selected tungstated zirconia catalysts, one below monolayer coverage (1.2 W* nm^{-2}*), the other around monolayer coverage (4.6 W* nm^{-2}*). Raman features of W-O-W linkages at 805* cm^{-1} *are detectable after reaching the monolayer coverage (~4 W* nm^{-2}*) on* ZrO_2*.*

The Raman spectra of supported WO_x/ZrO_2 catalysts show bands attributed to crystalline m-WO_3 (133, 178, 187, 272, 327, 417, 437, 448, 715, 805 cm^{-1}), with the most prominent features appearing at 715 and 805 cm^{-1}, while vibrations of the crystalline ZrO_2 support dominate at lower Raman shifts.[12] For all oxide-supported materials, the feature at ~805 cm^{-1} is the most dominant irrespective of the W loading. On ZrO_2-supported tungstate materials, this band becomes detectable only after reaching the monolayer coverage. Note also the Raman features (950–1015 cm^{-1}) that reflect a distribution of distorted WO_6 units in the framework associated with surface $O{=}WO_4$.

S-Table 4.3 *WO_x-crystallite sizes estimated using the Scherrer equation (N.D. = not determined due to the lack of reflections).*

Support	wt.% WO_3	Surface W density (W nm^{-2})	$d_{WOx\ crystallites}$ (nm)
ZrO_2	15	4.8	N.D.
ZrO_2	15	5.6	8.8
ZrO_2	15	20.4	38.7

4.6.3) IR spectroscopy of adsorbed CO_2

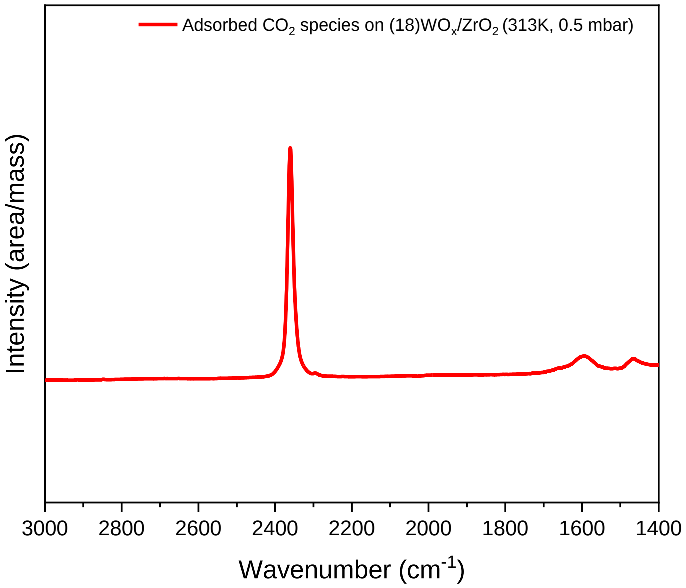

S-Figure 4.3 *IR spectra of adsorbed carbon dioxide on one representative tungstated materials. Bands of linearly adsorbed* CO_2*, carbonates, bridged carbonates and carboxylates are generally found at 2360, 1530-1620, 1620-1670 and 1350-1420* cm^{-1}*, respectively.*

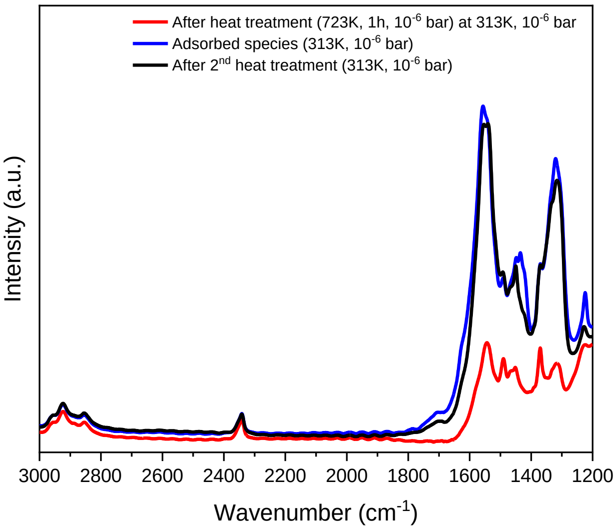

S-Figure 4.4 *IR-spectra of adsorbed carbon dioxide on* ZrO_2 *(*$Zr(OH)_4$ *preactivated at 973 K, 4 h in static air). Bands of linearly adsorbed* CO_2*, carbonates, bridged carbonates and carboxylates are generally found at 2360, 1530-1620, 1620-1670 and 1350-1420* cm^{-1}*, respectively.*

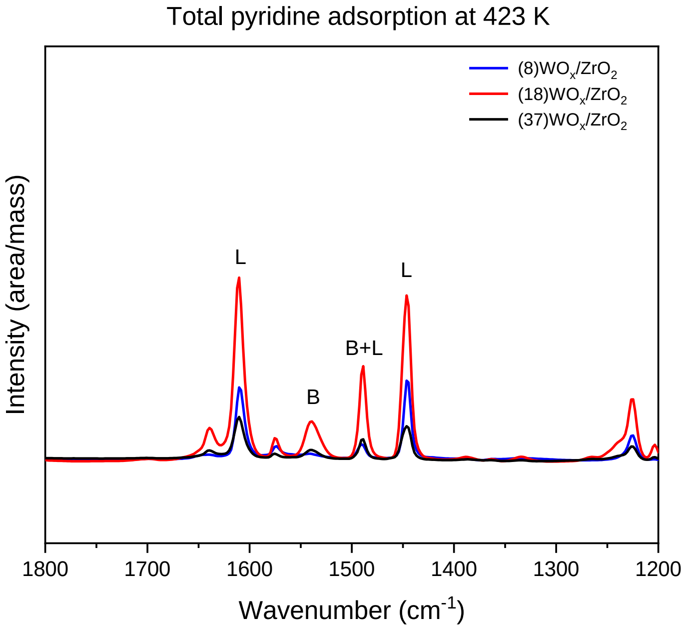

S-Figure 4.5 *Infrared spectra of tungstated zirconia catalysts with adsorbed pyridine.*

4.6.4) Titration of acidic sites during cyclohexanol dehydration

S-Table 4.4 *BAS and LAS concentrations measured by IR spectroscopy of pyridine adsorption on the studied tungstated catalysts.*

Catalyst	BAS (Pyr-IR)[a]	LAS (Pyr-IR)[a]	BAS (Pyr-IR)[a]	LAS (Pyr-IR)[a]
	µmol g^{-1}	µmol g^{-1}	µmol g^{-1}	µmol g^{-1}
(8)WO$_x$/ZrO$_2$	2	39	1	25
(18)WO$_x$/ZrO$_2$	60	103	24	43
(37)WO$_x$/ZrO$_2$	11	22	1	2

[a] Determined by quantitative analysis (integrated areas) of IR bands of pyridinium ions (~1540 cm^{-1}) and coordinatively bound pyridine (~1450 cm^{-1}), respectively. Pyridine adsorption and IR measurement was both performed at 423 K.

Liquid phase (in-situ):

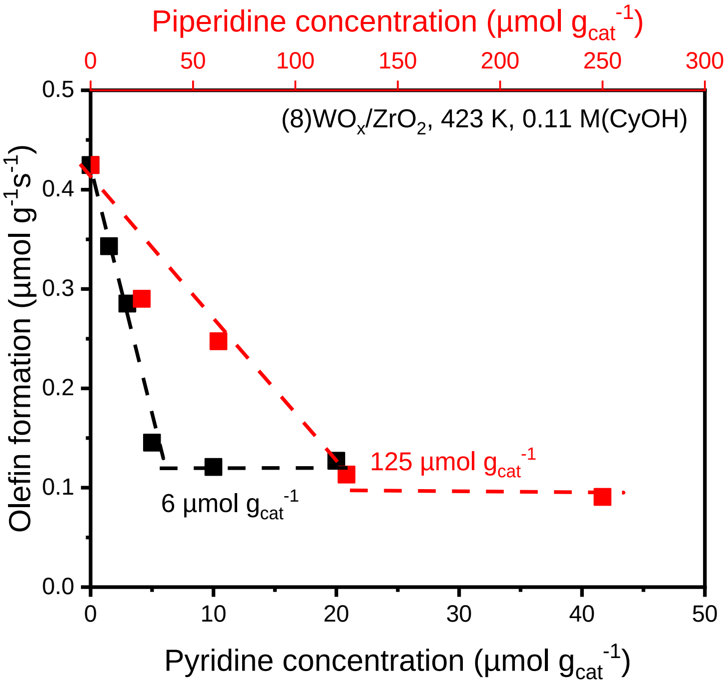

S-Figure 4.6 *Titration of (8)WO$_x$/ZrO$_2$ with pyridine (black, x-axis bottom) and piperidine (red, x-axis top) at 423 K and 0.11 M cyclohexanol. The value from which an increase of base molecules did not cause any further rate-suppression is depicted as guidance. Note that the x-axis represents the theoretical base uptakes. After no further suppression is possible, the remaining base is solvated in the bulk liquid. Also note that the initial CyOH concentration has no impact on the number of titratable sites (See S-Figure 4.7).*

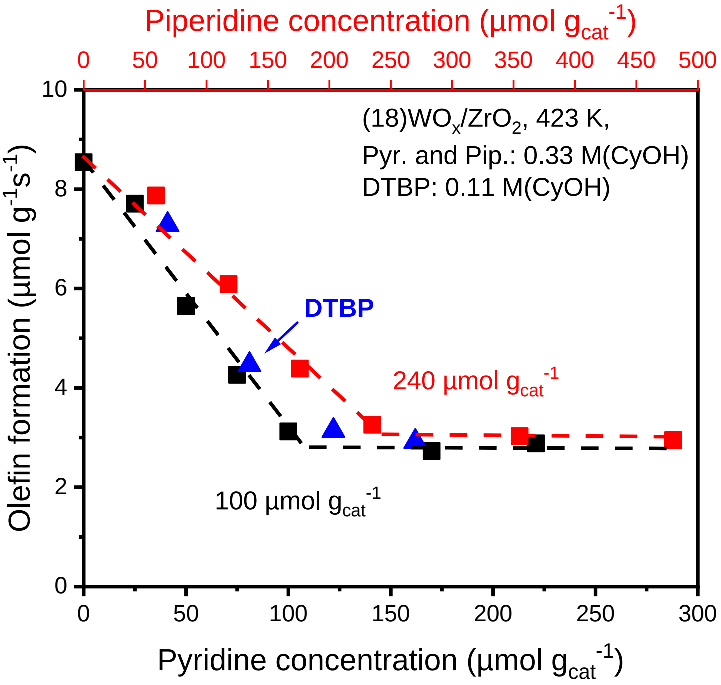

S-Figure 4.7 *Adapted from Figure 4.1(A) (main text). Titration of (18)WO$_x$/ZrO$_2$ with pyridine (black, x-axis bottom), DTBP (blue, x-axis bottom) and piperidine (red, x-axis* *top) at 423 K and 0.11-0.33 M cyclohexanol. The value from which an increase of base molecules did not cause any further rate-suppression is depicted as guidance. Note that the x-axis represents the theoretical base uptakes. After no further suppression is possible, the remaining base is solvated in the bulk liquid. Also note that the initial CyOH concentration has no impact on the number of titratable sites (See S-Figure 4.7).*

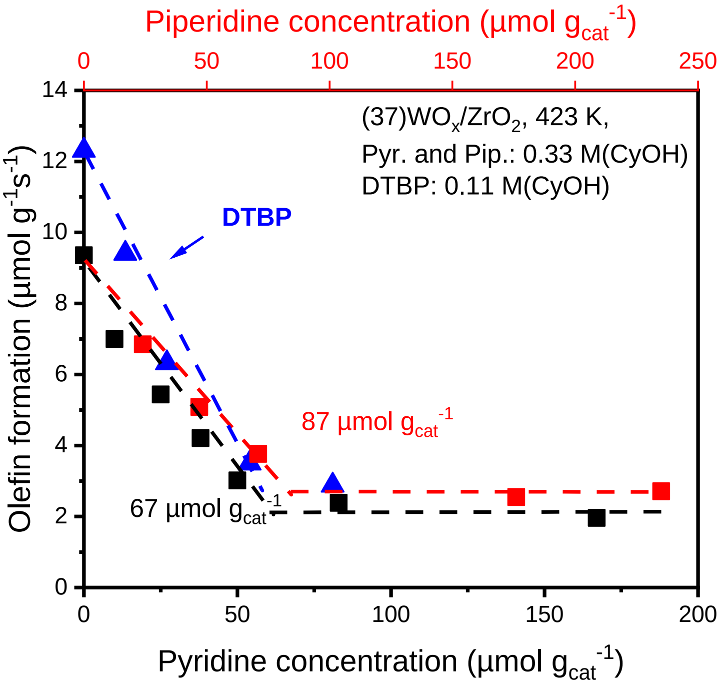

S-Figure 4.8 *Titration of (37)WO_x/ZrO_2 with pyridine (black, x-axis bottom) and piperidine (red, x-axis top) at 423 K and 0.11-0.33 M cyclohexanol. The value from which an increase of base molecules did not cause any further rate-suppression is depicted as guidance. Note that the x-axis represents the theoretical base uptakes. After no further suppression is possible, the remaining base is solvated in the bulk liquid. Also note that the initial CyOH concentration has no impact on the number of titratable sites (See S-Figure 4.7).*

To test if the titration method has a function of initial concentration, titration was carried out at two different initial concentrations. The results suggest that the site counts are independent of the initial alcohol concentration.

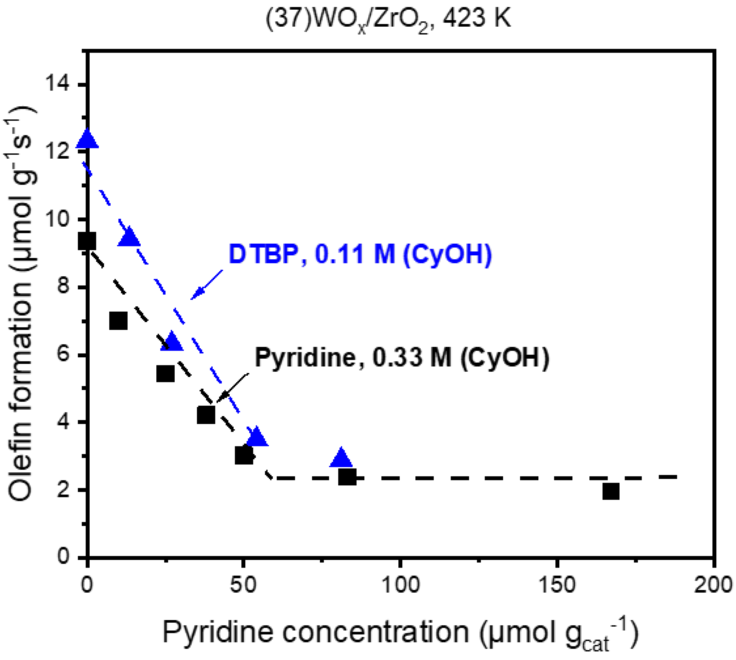

S-Figure 4.9 *A) Titration of (37)WO$_x$/ZrO$_2$ with pyridine (0.33 M initial CyOH-concentration) and DTBP (0.11 M initial CyOH-concentration) at 453 K*

To test if the titration method has a function of temperature, titration was carried out at two different reaction temperatures. The results suggest that the site counts are independent of the temperature (in this particular regime, increasing the temperature drastically will result in a different adsorption behavior of the tirant).

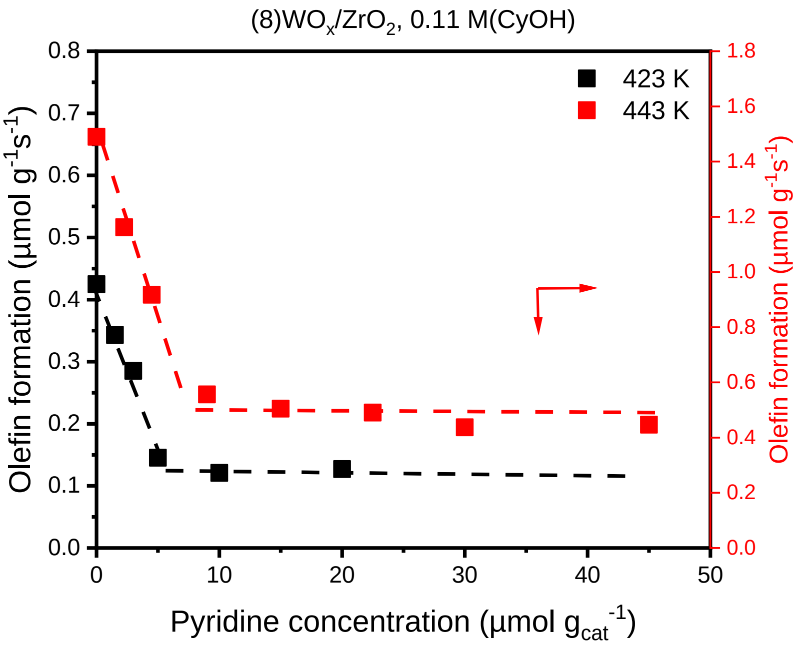

S-Figure 4.10 *Titration of (8)WO$_x$/ZrO$_2$ with pyridine (0.11 M initial CyOH-concentration) at 423 K and 443 K.*

4.6.5) Note on the mechanism causing a negative fractional order

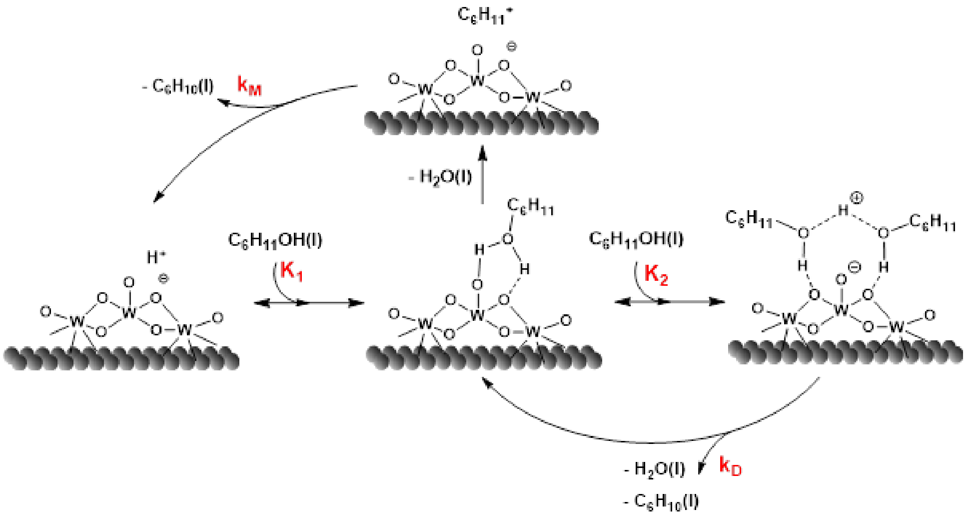

S-Figure 4.11 *(Adapted from main text). An illustration of a plausible sequence of steps involved in intramolecular dehydration of cyclohexanol catalyzed by BAS on tungstate domains.*

Based on the mechanism illustrated in the above Figure, the following rate expressions have been derived for olefin formation via monomer- and dimer-mediated elimination routes on catalytically active BAS (see main text for references):

$$\frac{r_{BAS}}{[H^+]_0} = \frac{k_M K_1 [CyOH] + k_D K_1 K_2 [CyOH]^2}{1 + K_1 [CyOH] + K_1 K_2 [CyOH]^2} \qquad \text{(Eq. 4.1)}$$

Considering that the rate constants (k_M and k_D) and equilibrium constants (K_1 and K_2) are temperature dependent one can simulate the shape of the concentration function. k_M and k_D will increase with temperature (T1 < T2 < T3) while K_1 and K_2 will decrease. Depending on the parameters one can yield experimentally a clearly negative fractional order or a positive order flattening at higher alcohol concentrations. The temperature function on the parameters are unknown and are likely different among the parameters. However, this gives a first impression on the complexity of the reaction system.

S-Table 4.5 *Kinetic regimes in apolar phase CyOH-dehydrations*

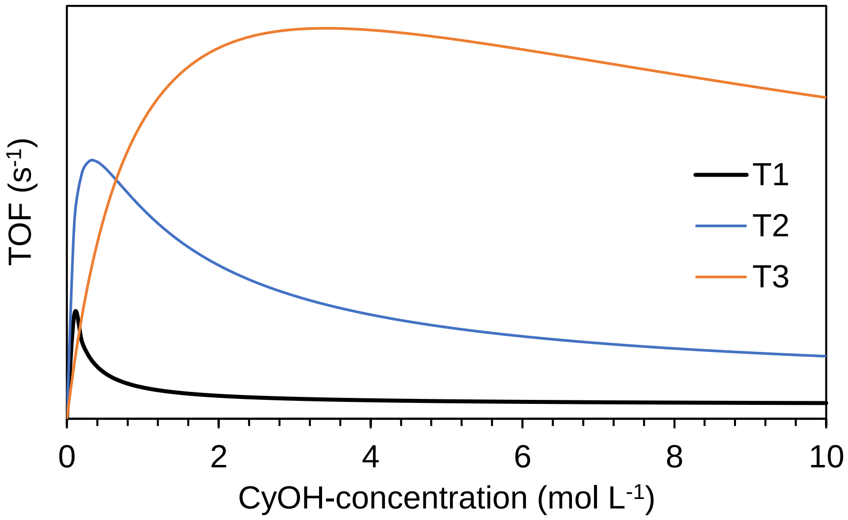

S-Table 4.6 *Parameters used for simulation of kinetic regimes of the above figure*

Parameter	T1	T2	T3
k_M	30	60	90
k_D	2	4	8
K_1	100	10	1
K_2	10	1	0.1

4.6.6) References

1 Kang, M., DeWilde, J. F. & Bhan, A. Kinetics and Mechanism of Alcohol Dehydration on γ-Al2O3: Effects of Carbon Chain Length and Substitution. *ACS Catalysis* **5**, 602-612, doi:10.1021/cs501471r (2015).

2 Wachs, I. E., Kim, T. & Ross, E. I. Catalysis science of the solid acidity of model supported tungsten oxide catalysts. *Catalysis Today* **116**, 162-168, doi:https://doi.org/10.1016/j.cattod.2006.02.085 (2006).

3 Knözinger, H. Dehydration of Alcohols on Aluminum Oxide. *Angewandte Chemie International Edition in English* **7**, 791-805, doi:10.1002/anie.196807911 (1968).

4 Knözinger, H. & Scheglila, A. The dehydration of alcohols on alumina: XII. Kinetic isotope effects in the olefin formation from butanols. *Journal of Catalysis* **17**, 252-263, doi:https://doi.org/10.1016/0021-9517(70)90098-9 (1970).

5 Bringué, R. *et al.* Thermally stable ion-exchange resins as catalysts for the liquid-phase dehydration of 1-pentanol to di-n-pentyl ether (DNPE). *Journal of Catalysis* **244**, 33-42, doi:https://doi.org/10.1016/j.jcat.2006.07.035 (2006).

6 Arata, K. in *Advances in Catalysis* Vol. 37 (eds D. D. Eley, Herman Pines, & Paul B. Weisz) 165-211 (Academic Press, 1990).

7 Barton, D. G., Shtein, M., Wilson, R. D., Soled, S. L. & Iglesia, E. Structure and Electronic Properties of Solid Acids Based on Tungsten Oxide Nanostructures. *The Journal of Physical Chemistry B* **103**, 630-640, doi:10.1021/jp983555d (1999).

8 Baertsch, C. D., Komala, K. T., Chua, Y.-H. & Iglesia, E. Genesis of Brønsted Acid Sites during Dehydration of 2-Butanol on Tungsten Oxide Catalysts. *Journal of Catalysis* **205**, 44-57, doi:https://doi.org/10.1006/jcat.2001.3426 (2002).

9 Hino, M. & Arata, K. Synthesis of solid superacid of tungsten oxide supported on zirconia and its catalytic action for reactions of butane and pentane. *Journal of the Chemical Society, Chemical Communications*, 1259-1260, doi:10.1039/C39880001259 (1988).

10 Horsley, J. A., Wachs, I. E., Brown, J. M., Via, G. H. & Hardcastle, F. D. Structure of surface tungsten oxide species in the tungsten trioxide/alumina supported oxide system from x-ray absorption near-edge spectroscopy and Raman spectroscopy. *The Journal of Physical Chemistry* **91**, 4014-4020, doi:10.1021/j100299a018 (1987).

11 Kuba, S. *et al.* Redox properties of tungstated zirconia catalysts: Relevance to the activation of n-alkanes. *Physical Chemistry Chemical Physics* **3**, 146-154, doi:10.1039/B007774G (2001).

12 Ross-Medgaarden, E. I. *et al.* New insights into the nature of the acidic catalytic active sites present in ZrO2-supported tungsten oxide catalysts. *Journal of Catalysis* **256**, 108-125, doi:https://doi.org/10.1016/j.jcat.2008.03.003 (2008).

13 Ross-Medgaarden, E. I. & Wachs, I. E. Structural Determination of Bulk and Surface Tungsten Oxides with UV−vis Diffuse Reflectance Spectroscopy and Raman Spectroscopy. *The Journal of Physical Chemistry C* **111**, 15089-15099, doi:10.1021/jp074219c (2007).

14 Scheithauer, M. *et al.* Characterization of WOx/ZrO2by Vibrational Spectroscopy andn-Pentane Isomerization Catalysis. *Journal of Catalysis* **180**, 1-13, doi:https://doi.org/10.1006/jcat.1998.2237 (1998).

15 Scheithauer, M., Grasselli, R. K. & Knözinger, H. Genesis and Structure of WOx/ZrO2 Solid Acid Catalysts. *Langmuir* **14**, 3019-3029, doi:10.1021/la971399g (1998).

16 Wachs, I. E. Raman and IR studies of surface metal oxide species on oxide supports: Supported metal oxide catalysts. *Catalysis Today* **27**, 437-455, doi:https://doi.org/10.1016/0920-5861(95)00203-0 (1996).

17 Zhou, W. *et al.* Identification of active Zr–WOx clusters on a ZrO2 support for solid acid catalysts. *Nature Chemistry* **1**, 722-728, doi:10.1038/nchem.433 (2009).

18 Zhou, W. *et al.* Nature of Catalytically Active Sites in the Supported WO3/ZrO2 Solid Acid System: A Current Perspective. *ACS Catalysis* **7**, 2181-2198, doi:10.1021/acscatal.6b03697 (2017).

19 Macht, J. *et al.* Support effects on Brønsted acid site densities and alcohol dehydration turnover rates on tungsten oxide domains. *Journal of Catalysis* **227**, 479-491, doi:https://doi.org/10.1016/j.jcat.2004.08.014 (2004).

20 Herrera, J. E. *et al.* Synthesis, characterization, and catalytic function of novel highly dispersed tungsten oxide catalysts on mesoporous silica. *Journal of Catalysis* **239**, 200-211, doi:https://doi.org/10.1016/j.jcat.2006.01.034 (2006).

21 Shi, D. *et al.* WOx supported on γ-Al2O3 with different morphologies as model catalysts for alkanol dehydration. *Journal of Catalysis* **363**, 1-8, doi:https://doi.org/10.1016/j.jcat.2018.04.004 (2018).

22 Mallesham, B., Sudarsanam, P., Raju, G. & Reddy, B. M. Design of highly efficient Mo and W-promoted SnO2 solid acids for heterogeneous catalysis: acetalization of bio-glycerol. *Green Chemistry* **15**, 478-489, doi:10.1039/C2GC36152C (2013).

23 Park, Y.-M., Chung, S.-H., Eom, H. J., Lee, J.-S. & Lee, K.-Y. Tungsten oxide zirconia as solid superacid catalyst for esterification of waste acid oil (dark oil). *Bioresource Technology* **101**, 6589-6593, doi:https://doi.org/10.1016/j.biortech.2010.03.109 (2010).

24 Liu, Y., Luo, C. & Liu, H. Tungsten Trioxide Promoted Selective Conversion of Cellulose into Propylene Glycol and Ethylene Glycol on a Ruthenium Catalyst. *Angewandte Chemie International Edition* **51**, 3249-3253, doi:10.1002/anie.201200351 (2012).

25 Rorrer, J., Pindi, S., Toste, F. D. & Bell, A. T. Effect of Alcohol Structure on the Kinetics of Etherification and Dehydration over Tungstated Zirconia. *ChemSusChem* **11**, 3104-3111, doi:10.1002/cssc.201801067 (2018).

26 Rorrer, J., He, Y., Toste, F. D. & Bell, A. T. Mechanism and kinetics of 1-dodecanol etherification over tungstated zirconia. *Journal of Catalysis* **354**, 13-23, doi:https://doi.org/10.1016/j.jcat.2017.08.001 (2017).

27 Lin, F. *et al.* Single-Facet Dominant Anatase TiO2 (101) and (001) Model Catalysts to Elucidate the Active Sites for Alkanol Dehydration. *ACS Catalysis* **10**, 4268-4279, doi:10.1021/acscatal.9b04654 (2020).

28 Kostestkyy, P., Yu, J., Gorte, R. J. & Mpourmpakis, G. Structure–activity relationships on metal-oxides: alcohol dehydration. *Catalysis Science & Technology* **4**, 3861-3869, doi:10.1039/C4CY00632A (2014).

29 Zhi, Y. *et al.* Dehydration Pathways of 1-Propanol on HZSM-5 in the Presence and Absence of Water. *Journal of the American Chemical Society* **137**, 15781-15794, doi:10.1021/jacs.5b09107 (2015).

30 Liu, Y. *et al.* Solvent-determined mechanistic pathways in zeolite-H-BEA-catalysed phenol alkylation. *Nature Catalysis* **1**, 141-147, doi:10.1038/s41929-017-0015-z (2018).

31 Hoek, I., Nijhuis, T. A., Stankiewicz, A. I. & Moulijn, J. A. Kinetics of solid acid catalysed etherification of symmetrical primary alcohols: zeolite BEA catalysed etherification of 1-octanol. *Applied Catalysis A: General* **266**, 109-116, doi:https://doi.org/10.1016/j.apcata.2004.02.005 (2004).

32 DeWilde, J. F., Chiang, H., Hickman, D. A., Ho, C. R. & Bhan, A. Kinetics and Mechanism of Ethanol Dehydration on γ-Al2O3: The Critical Role of Dimer Inhibition. *ACS Catalysis* **3**, 798-807, doi:10.1021/cs400051k (2013).

33 Parry, E. P. An infrared study of pyridine adsorbed on acidic solids. Characterization of surface acidity. *Journal of Catalysis* **2**, 371-379, doi:https://doi.org/10.1016/0021-9517(63)90102-7 (1963).

34 Soled, S. L. *et al.* Comparison of the acidities of WO3Al2O3 and ultrastable faujasite catalysts. *Journal of Catalysis* **111**, 286-295, doi:https://doi.org/10.1016/0021-9517(88)90087-5 (1988).

35 Zhao, C., He, J., Lemonidou, A. A., Li, X. & Lercher, J. A. Aqueous-phase hydrodeoxygenation of bio-derived phenols to cycloalkanes. *Journal of Catalysis* **280**, 8-16, doi:https://doi.org/10.1016/j.jcat.2011.02.001 (2011).

36 Macht, J. & Iglesia, E. Structure and function of oxide nanostructures: catalytic consequences of size and composition. *Physical Chemistry Chemical Physics* **10**, 5331-5343, doi:10.1039/B805251D (2008).

37 Larsen, G., Lotero, E., Petkovic, L. a. M. & Shobe, D. S. Alcohol Dehydration Reactions over Tungstated Zirconia Catalysts. *Journal of Catalysis* **169**, 67-75, doi:https://doi.org/10.1006/jcat.1997.1698 (1997).

38 Calatayud, M., Ruppert, A. M. & Weckhuysen, B. M. Theoretical Study on the Role of Surface Basicity and Lewis Acidity on the Etherification of Glycerol over Alkaline Earth Metal Oxides. *Chemistry – A European Journal* **15**, 10864-10870, doi:https://doi.org/10.1002/chem.200900487 (2009).

39 Foo, G. S., Wei, D., Sholl, D. S. & Sievers, C. Role of Lewis and Brønsted Acid Sites in the Dehydration of Glycerol over Niobia. *ACS Catalysis* **4**, 3180-3192, doi:10.1021/cs5006376 (2014).

40 Pfriem, N. *et al.* Impact of the Local Concentration of Hydronium Ions at Tungstate Surfaces for Acid-Catalyzed Alcohol Dehydration. *Journal of the American Chemical Society* **143**, 20133-20143, doi:10.1021/jacs.1c07203 (2021).

41 Emeis, C. A. Determination of Integrated Molar Extinction Coefficients for Infrared Absorption Bands of Pyridine Adsorbed on Solid Acid Catalysts. *Journal of Catalysis* **141**, 347-354, doi:https://doi.org/10.1006/jcat.1993.1145 (1993).

42 Barzetti, T., Selli, E., Moscotti, D. & Forni, L. Pyridine and ammonia as probes for FTIR analysis of solid acid catalysts. *Journal of the Chemical Society, Faraday Transactions* **92**, 1401-1407, doi:10.1039/FT9969201401 (1996).

43 Kim, D. S., Ostromecki, M. & Wachs, I. E. Surface structures of supported tungsten oxide catalysts under dehydrated conditions. *Journal of Molecular Catalysis A: Chemical* **106**, 93-102, doi:https://doi.org/10.1016/1381-1169(95)00186-7 (1996).

44 Barton, D. G., Soled, S. L., Meitzner, G. D., Fuentes, G. A. & Iglesia, E. Structural and Catalytic Characterization of Solid Acids Based on Zirconia Modified by Tungsten Oxide. *Journal of Catalysis* **181**, 57-72, doi:https://doi.org/10.1006/jcat.1998.2269 (1999).

45 García-Fernández, S. *et al.* The role of tungsten oxide in the selective hydrogenolysis of glycerol to 1,3-propanediol over Pt/WOx/Al2O3. *Applied Catalysis B: Environmental* **204**, 260-272, doi:https://doi.org/10.1016/j.apcatb.2016.11.016 (2017).

46 Law, H. Y., Blanchard, J., Carrier, X. & Thomas, C. NOx-TPD as a Tool to Estimate the Accessible Zirconia Surface of ZrO2-Containing Materials. *The Journal of Physical Chemistry C* **114**, 9731-9738, doi:10.1021/jp9089535 (2010).

47 Santiesteban, J. G., Vartuli, J. C., Han, S., Bastian, R. D. & Chang, C. D. Influence of the Preparative Method on the Activity of Highly Acidic WOx/ZrO2and the Relative Acid Activity Compared with Zeolites. *Journal of Catalysis* **168**, 431-441, doi:https://doi.org/10.1006/jcat.1997.1658 (1997).

48 Kim, T., Burrows, A., Kiely, C. J. & Wachs, I. E. Molecular/electronic structure–surface acidity relationships of model-supported tungsten oxide catalysts.

Journal of Catalysis **246**, 370-381, doi:https://doi.org/10.1016/j.jcat.2006.12.018 (2007).

49 Jacobs, P. A. & Heylen, C. F. Active sites in zeolites: III. Selective poisoning of Bronsted sites on synthetic Y zeolites. *Journal of Catalysis* **34**, 267-274, doi:https://doi.org/10.1016/0021-9517(74)90036-0 (1974).

50 Das, D., Mishra, H. K., Parida, K. M. & Dalai, A. K. Preparation, physico-chemical characterization and catalytic activity of sulphated ZrO2–TiO2 mixed oxides. *Journal of Molecular Catalysis A: Chemical* **189**, 271-282, doi:https://doi.org/10.1016/S1381-1169(02)00363-1 (2002).

51 Bedard, J., Chiang, H. & Bhan, A. Kinetics and mechanism of acetic acid esterification with ethanol on zeolites. *Journal of Catalysis* **290**, 210-219, doi:https://doi.org/10.1016/j.jcat.2012.03.020 (2012).

52 Macht, J., Janik, M. J., Neurock, M. & Iglesia, E. Catalytic Consequences of Composition in Polyoxometalate Clusters with Keggin Structure. *Angewandte Chemie International Edition* **46**, 7864-7868, doi:https://doi.org/10.1002/anie.200701292 (2007).

53 Macht, J., Janik, M. J., Neurock, M. & Iglesia, E. Mechanistic Consequences of Composition in Acid Catalysis by Polyoxometalate Keggin Clusters. *Journal of the American Chemical Society* **130**, 10369-10379, doi:10.1021/ja803114r (2008).

54 Chiang, H. & Bhan, A. Catalytic consequences of hydroxyl group location on the rate and mechanism of parallel dehydration reactions of ethanol over acidic zeolites. *Journal of Catalysis* **271**, 251-261, doi:https://doi.org/10.1016/j.jcat.2010.01.021 (2010).

55 Liu, Y. *et al.* Enhancing the catalytic activity of hydronium ions through constrained environments. *Nature Communications* **8**, 14113, doi:10.1038/ncomms14113

https://www.nature.com/articles/ncomms14113#supplementary-information (2017).

56 Kuba, S., Lukinskas, P., Grasselli, R. K., Gates, B. C. & Knözinger, H. Structure and properties of tungstated zirconia catalysts for alkane conversion. *Journal of Catalysis* **216**, 353-361, doi:https://doi.org/10.1016/S0021-9517(02)00125-2 (2003).

57 Munos, J. W., Pu, X., Mansoorabadi, S. O., Kim, H. J. & Liu, H.-w. A Secondary Kinetic Isotope Effect Study of the 1-Deoxy-d-xylulose-5-phosphate Reductoisomerase-Catalyzed Reaction: Evidence for a Retroaldol-Aldol Rearrangement. *Journal of the American Chemical Society* **131**, 2048-2049, doi:10.1021/ja807987h (2009).

5) Summary and Conclusion

The summary section is based on references to Chapter 2-4. See the main text for references to related literature.

In zeolites Brønsted acidity is introduced into the microporous framework through the addition of framework aluminum, which creates in the presence of water in the limited volume of the microchannels of zeolite H-MFI a high concentration of hydrated hydronium ions at aluminum sites. The catalytic activity of these constrained hydronium ions is up to two orders of magnitude higher than the respective specific activity of hydrated hydronium ions in an aqueous acid solution as probed by alcohol dehydration. In zeolites, the resulting high charge density creates a highly non-ideal solvation environment, in which the proximity between the molecules is enhanced, which has been shown in literature to lead to an increase in the activity coefficient of organic molecules in the zeolite pores. The impact on activity coefficient directly translates to a increased excess chemical potential of sorbed and uncharged organic reactants. For cyclohexanol dehydrogenation, the charged carbenium-ion transition state was in addition stabilized, the activation barrier in consequence reduced and the reaction rates were observed to be higher.

Rates were analyzed for a set of zeolites varying BAS concentration from 0.054 to 0.86 mmol/g_{MFI}. The reaction rate is observed to be independent of the aqueous phase concentration of cyclohexanol. However, the activity is a function of the BAS concentration in a volcano-like shape, with a maximum at ~0.36 mmol/g_{MFI}. The increasing part of the function on BAS concentration [BAS] arises from the micropore volume, creating together with the BAS counts an enhanced charged and constrained environment with a increasing ionic strength along the [BAS] coordinate. As cyclohexanol is a neutral molecule in the ground state, while it is a positively charged cyclohexyl carbenium ion in the transition state, we show that the uncharged species get unstabilzed with increasing ionic strength, while charged species become stabilized in ionic environment. The increasing function of TOF over ionic strength is also observed for soluble acids, such as hydrochloric acid, in an artificial ionic environment created by LiCl addition. Both types of ionic strength (“external” via LiCl addition and “internal” via constrained BAS concentration) are comparable. We showed that partly exchanged H-HMF with Na^+ (up to 75% exchange degree), have higher TOFs than H-MFI with the same BAS concentration, due to higher local ionic strength.

However, we observed in contrast to HCl, that H-MFI plotted as a function of ionic strength drops at higher ionic strength. We show that the decrease in rate is due to a decrease in distance of hydronium ion boundaries. A critical distance is observed at which the volume between two neighboring hydronium ions is equal to the van der Waal volume of cyclohexanol. This causes a repulsion that increases the energy of the TS and consequently decreases the TOF due to a higher activation barrier.

The alcohol dehydration reaction was further carried out using a series of hydrothermally stable supported tungstate catalysts. In analogy to reaction on H-MFI we demonstrate that hydronium ions constrained within the electrical double layer (EDL) of mesoporous surfaces show a marked dependence of TOF on constrained proton concentration. This site-specific activity increases with the density of $(H_3O^+)_{hydr.}$ in the layer above the solid surface. The maximum TOFs rival the most active zeolite catalysts for the same reaction.

The ability of oxide-supported tungstates to delocalize hydronium ions in the EDL is a function of the surface tungstate domains. We show that from isolated monotungstated to two-dimensional polytungstates TOFs are a steep function of surface W density up to monolayer coverage. Exceeding monolayer coverage the activity becomes independent of the W-surface density and structural changes of tungstate. Moreover a substantial support effect (Al_2O_3 < ZrO_2 < TiO_2 <C) on activity is reported. We show via KIE measurements that these differences are not caused by changes in the reaction mechanism or rate-determining step. We demonstrate that TOFs increase with the estimated hydronium ion concentrations in the EDL (with increasing proximity of hydronium ions localized in the EDL) over the negatively charged WOx-domain. Similar to the above discussed ionic strength effect in zeolites our findings reflect the impact of ionic strength, H-bonding and the associated variations in electrostatic forces on the stability of the positively charged deprotonation transition state in the EDL.

In contrast to aqueous phase alcohol dehydration over tungstate zirconia catalyst, the elimination reaction in aprotic solvents proceeds via a monomer- and dimer-mediated pathway over Brønsted acid sites (bridging OH-groups, not hydronium ions). In contrast to literature we report three kinds of surface sites on WO_x/ZrO_2 catalysts. We identify and quantify active sites (BAS) that bind strong and weaker bases and contribute predominantly to the catalytic activity. However, we also identified weak acid sites that do not bind pyridine/DTBP, but bind piperidine (stronger base), and are inactive for dehydration. In contrast to literature, we further recognize weak acid sites that bind none of the investigated N-titrants, but which contribute to the catalytically activity. We show that the latter sites are Lewis acidic and catalyze the reaction via a E2-pathway.

6) List of publications

Qiang Liu, **Niklas Pfriem**, Guanhua Cheng, Eszter Baráth, Yue Liu*, Johannes A. Lercher*, “Maximum Impact of Ionic Strength on Acid-Catalyzed Reaction Rates Induced by a Zeolite Microporous Environment”, DOI: 10.1002/anie.202208693, Angew. Chem. 2023

Niklas Pfriem, Peter H Hintermeier, Sebastian Eckstein, Sungmin Kim, Qiang Liu, Hui Shi, Lara Milakovic, Yuanshuai Liu, Gary L Haller, Eszter Baráth, Yue Liu*, Johannes A Lercher*, “Role of the ionic environment in enhancing the activity of reacting molecules in zeolite pores”, DOI: 10.1126/science.abh3418, Science 2021

Niklas Pfriem, Yue Liu, Florian Zahn, Hui Shi*, Gary L Haller, Johannes A Lercher*, “Impact of the Local Concentration of Hydronium Ions at Tungstate Surfaces for Acid-Catalyzed Alcohol Dehydration”, DOI: 10.1021/jacs.1c07203, J. Am. Chem. Soc. 2021

Junnan Shangguan, Alyssa JR Hensley, Matthew V Gradiski, **Niklas Pfriem**, Jean-Sabin McEwen, Robert H Morris, Ya-Huei Cathy Chin*, “The role of protons and hydrides in the catalytic hydrogenolysis of guaiacol at the ruthenium nanoparticle–water interface”, DOI: 10.1021/acscatal.0c01963, J. Am. Chem. Soc. 2020

Junnan Shangguan, **Niklas Pfriem**, Ya-Huei Cathy Chin*, “Mechanistic details of CO bond activation in and H-addition to guaiacol at water-Ru cluster interfaces”, DOI: 10.1016/j.jcat.2018.11.036, J Catal. 2019

7) Curriculum vitae

Since 04/2021	Process Engineer Hydrotreating and Reforming Bayernoil Raffineriegesellschaft mbH
09/2017 – 04/2021	PhD Candidate Supervisor: Prof. Dr. Johannes A. Lercher Chair of Technical Chemistry II Technische Universität München
10/2016 – 03/2017	Master's Thesis Multidisciplinary Laboratory for Innovative Catalytic Science University of Toronto Supervisor: Prof. Dr. Ya-Huei (Cathy) Chin Prof. Dr. Johannes A. Lercher
09/2015 – 08/2017	Master of Science Chemical Engineering Chemical Process Technologies & Catalysis Technische Universität München
09/2011 – 08/2015	Bachelor of Science Chemical Engineering Technische Universität München
Until 2011	Abitur Gymnasium Geretsried